

Electronic Thesis and Dissertation Repository

---

7-30-2019 10:00 AM

## Three Dimensional Characterization of Deformation Twins Using Synchrotron X-Ray Diffraction

Karim Louca, *The University of Western Ontario*

Supervisor: Abdolvand, Hamidreza, *The University of Western Ontario*

A thesis submitted in partial fulfillment of the requirements for the Master of Science degree in Mechanical and Materials Engineering

© Karim Louca 2019

Follow this and additional works at: <https://ir.lib.uwo.ca/etd>

---

### Recommended Citation

Louca, Karim, "Three Dimensional Characterization of Deformation Twins Using Synchrotron X-Ray Diffraction" (2019). *Electronic Thesis and Dissertation Repository*. 6374.  
<https://ir.lib.uwo.ca/etd/6374>

This Dissertation/Thesis is brought to you for free and open access by Scholarship@Western. It has been accepted for inclusion in Electronic Thesis and Dissertation Repository by an authorized administrator of Scholarship@Western. For more information, please contact [wlsadmin@uwo.ca](mailto:wlsadmin@uwo.ca).

## Abstract

Hexagonal closed-packed (HCP) metals have been extensively used in various industrial sectors, eg, zirconium in nuclear industry, magnesium in transportation industry, and titanium in aerospace industry. Understanding deformation mechanisms of HCP metals is crucial for developing predictive models that can be used for performance and failures analysis of engineering components. The two main deformation modes in HCP polycrystals are slip and twinning. While deformation by slip is well understood, many fundamental questions about twinning are still remained unanswered.

The aim of this research is to employ a novel experimental technique, three-dimensional synchrotron X-ray diffraction, on two different HCP metals and acquire a statistical data that can help us understand fundamentals of deformation twinning. After a literature review in chapter two, the steps used for preparing samples, conducting the experiment, and post-processing the collected diffraction patterns are explained in chapter 3. The results of the experiments on zirconium and magnesium samples are provided and discussed in chapters 4, and 5, respectively. This is followed by conclusions and future work.

By updating and developing new procedures for grain matching, more than 19000 grains are investigated individually. It is shown for the first time that twin variant selection is preferential in the plastic zone, yet not at the early stages of plasticity. It is shown that due to local and macroscopic stress configurations, twins in zirconium are generally relaxed along the loading direction, but not in magnesium. In this thesis, the very first in-situ cyclic compress-tension experiment on magnesium was conducted where twinning and de-twinning were fully observed in 3D. Understanding the mechanism of twin nucleation and propagation can help us update our existing numerical models and improve our predictions.

**Keywords:** 3D-XRD, Twinning, Hexagonal Close-Packed, Polycrystal, Texture, EBSD

## Summary of Lay Audience

A broader view of this research topic is deformation of metals. Most metals are solid in nature and consist of closely packed atoms. The packing of these atoms varies from one metal to another, like face centered cubic (FCC) in aluminum and hexagonal close packed (HCP) in magnesium. The collection of crystals form lattice that can have point or line defects (dislocations) due to missing atoms. The population of these defect change with plasticity, effecting hardening.

Ideally, the lattice of atoms would all be packed in a single direction however most metals that exist in nature are polycrystalline in nature. This means the metal consists of several lattices or single crystals of different sizes and directions.

Most metals, like FCC and body centered cubic (BCC), deform in the plastic region through movement of dislocations. However, in HCP metals, another deformation mechanism, known as twinning, can occur when the lattice is oriented in a specific direction. Twinning is a mechanism that occurs in single lattice causing a portion of the lattice to re-orient in another direction.

Twinning can be advantageous, in terms of improving the ductility of the material, and disadvantageous, in terms of providing susceptible sites to crack nucleation. Therefore, the first step to understand twinning is investigating the parameters affecting its initiation. Most of the studies conducted before to understand twinning have viewed twins in 2D in terms of shape and stresses. The experiment conducted in this research looks at twins in 3D and uses the synchrotron 3D-XRD method.

## Statement of Co-Authorship

The preparation of zirconium specimens prior to the experiment were handled by me and Dr. Abdolvand. These preparations include sample design, machining, heat treatment, polishing, electropolishing, and characterization with SEM and EBSD. The magnesium specimens were prepared by our collaborator, Dr. Mareau in France. The synchrotron experiment was conducted at ID-11 of the European Synchrotron Radiation Facility (ESRF), Grenoble, France, where a six-day beamtime was awarded as a part of the proposal MA-3613.

The codes used for processing the raw data are developed at ID-11, ESRF, but I and Dr. Abdolvand customized the codes for post-processing our experimental data.

Grain assembling, grain matching, and twin identification codes are originally developed by Dr. Abdolvand, but they are upgraded and modified by me. All figure preparation and data interpretations provided in chapters 3 to 6 are done by me.

## Acknowledgements

I would like to start by greatly thanking Professor Hamidreza Abdolvand for giving me the opportunity to be a part of this group. His guidance and mentorship throughout this entire journey have exceeded my expectations and his enthusiasm in the field has always been a factor of my motivation.

I would like to express my gratitude towards the team at beamline ID11 at ESRF for giving us the opportunity to conduct the experiment (ID: MA3613) at their facility. Thank you to Drs. Marta Majkut and Jonathan Wright for assisting us with conducting the experiment. Thank you to Prof. Charles Mareau for preparing the magnesium specimens for the experiment. He is currently conducting the modeling work for data comparison with the experimental results. Thank you also to the rest of the lab, Omid Sedaghat and Abdulla Alawadi, for creating an encouraging and thriving environment to work.

I would like to acknowledge the NSERC program for supporting and funding this project.

Finally, I would like to thank my family and relatives for their constant emotional support. My mother and father have always believed in me through my ups and downs and their support is the reason I am able to pursue my goals.

## Table of contents

Abstract.....	i
Summary of Lay Audience.....	ii
Statement of Co-Authorship .....	iii
Acknowledgements.....	iv
List of Tables.....	vii
List of Figures .....	viii
List of Acronyms and Symbols.....	x
1. Introduction.....	1
1.1 Motivation .....	1
1.1.1 Industrial Applications of Zirconium Alloys .....	1
1.1.2 Industrial Applications of Magnesium Alloys.....	2
1.2 Scope of this research.....	2
1.3 Outline.....	3
2. Literature Review .....	4
2.1 Deformation Mechanisms in HCP metals.....	4
2.2 The Mechanism of Deformation Twinning.....	7
2.3 Evolution of Deformation Twins .....	10
2.3.1 Schmid Factor.....	10
2.3.2 Neighboring effects .....	10
2.3.3 Size effects.....	11
2.3.4 Residual Stresses .....	12
2.3.5 Stresses in Parents and Twins.....	12
2.3.6 Twin Volume Fraction .....	13
2.3.6 Modeling .....	14
2.4 Experimental and characterization techniques.....	15
2.4.1 Diffraction Basics: Bragg's Law .....	15
2.4.2 Texture measurement .....	16
2.4.3 Characterization Techniques.....	19
3. Experimental Procedures and Data Processing.....	25
3.1 Pre-experimental procedures .....	25
3.2 3D-XRD experiment and setup .....	29
3.3 Diffraction data processing .....	31

3.3.1	Indexing grains .....	31
3.3.2	Refining grains.....	32
3.3.3	Mathematical Formulation.....	33
3.3.4	Post-Analysis of grain maps .....	36
4.	Analysis of 3D-XRD experiment on zirconium.....	42
4.1	Details of 3D-XRD Results.....	42
4.2	Comparison between EBSD and 3D-XRD .....	46
4.2.1	Texture .....	46
4.2.2	Grain Sizes.....	47
4.3	Post Analysis.....	48
4.4	Deformation Twinning Results .....	55
4.5	Conclusions.....	62
5.	Analysis of 3D-XRD results on Mg AZ31.....	64
5.1	Details of 3D-XRD results .....	64
5.2	Grain maps and texture analysis .....	67
5.3	Twinning in 3D .....	74
5.4	Repeatability .....	78
5.5	Conclusions.....	79
6.	Conclusion and Future Work.....	81
6.1	Conclusion.....	81
6.2	Contributions .....	83
6.3	Future Work.....	83
	References .....	85
	Curriculum Vitae.....	92

## List of Tables

<b>Table 2.1: Slip systems in HCP metals [12]</b> .....	6
<b>Table 2.2: The six variants of tensile twins [18]</b> .....	9
<b>Table 4.1: 3D-XRD Table of Results for Zirconium</b> .....	45
<b>Table 4.2: CRSS of slip systems of Zircaloy-2 (<math>\alpha</math>-Zr) [38] and single crystal pure Zr of size 10 <math>\mu</math>m [64]</b> .....	51
<b>Table 5.1: 3D-XRD Table of Results for Mg AZ31</b> .....	65
<b>Table 5.2: CRSS of slip systems on Mg AZ31 [43]</b> .....	68



## List of Figures

Figure 2.1: (a) Unit cells of BCC, FCC and HCP crystals, (b) The $c/a$ ratios for different HCP metals [11].....	5
Figure 2.2: (a) Tensile twinning system in HCP unit cell, (b) Twinning and slip mechanism (c) Deformation Twins detected captured through EBSD labelled as ‘MXTX’ and X is a number [20] .	8
Figure 2.3: (a) Labelled schematics of twinning elements and plane of shear, P, [18] (b) Type I and Type II twins respectively [21] .....	9
Figure 2.4: Twin volume fraction against applied strain [42]–[44].....	14
Figure 2.5: (a) labelled Bragg's condition, (b) single crystal and polycrystal morphology .....	16
Figure 2.6: Variation in the mass absorption coefficient with x-ray wavelength showing the K-edge and L-edge [53].....	17
Figure 2.7: Different beams emitted during electron microscopy [53] .....	19
Figure 2.8: (a) & (b) are configuration A, (c) is configuration C, and (d) is configuration B [58] ....	22
Figure 2.9: Schematic of 3D-XRD [58].....	23
Figure 2.10: Schematics of (a) DCT and (b) DAXM.....	24
Figure 2.11: Detector A ( $2\theta \sim 0o$ ) and (b) Detector B ( $2\theta \sim 90o$ ) setups in DCT based on the schematic in figure 2.10 (a) [61] .....	24
Figure 3.1: (a) – (d) Preliminary designs for in-situ 3D-XRD experiment, (e) the modified deformation grip with the final sample design and (f) dimensions of the selected specimen .....	26
Figure 3.2: (a,b) optical image, (c,d) grain sized distribution and (e,f) EBSD maps before and after heat treatment of zirconium. (a), (c), and (e) are from the “as-received”.....	27
Figure 3.3: Final EBSD map of zirconium sample after mechanical polishing and electropolishing	28
Figure 3.4: Pole figures measured for Mg AZ31 prior to 3D-XRD experiment.....	28
Figure 3.5: The experimental setup at ID-11, ESRF.....	29
Figure 3.6: Flowchart describing the procedure of postprocessing the diffraction images .....	33
Figure 3.7: (a) Schematic of 3D-XRD experimental setup, (b) Illustration of the scattering vector, $q$ .....	34
Figure 3.8: Variation of number of paired grains with angular misorientation limit in pairing grains during grain map construction for (a) Zr and (b) MgAZ31.....	37
Figure 3.9: Schematic of a single grain in two separate layers .....	38
Figure 3.10: Variation of the number of paired grains with the distance limit (between COMs of paired grains) for (a) Zr and (b) MgAZ31.....	38
Figure 3.11: Variation of the number of paired grains with the added tolerance to summation of the radii of the paired grains for (a) Zr and (b) Mg AZ31B.....	39
Figure 3.12: EBSD map sectioned into layers to illustrate the divided grains in Pairs 1, 2, 3 .....	40
Figure 3.13: X-Y Plane of the paired grains in Layers (a) 11 and (b) 12 in the 1st step of Zr. The figure demonstrates that all the grains have the same x- and y-coordinates.....	41
Figure 4.1: Stress-strain plot of in-situ 3D-XRD measurement of zirconium .....	43
Figure 4.2: Diffraction patterns of (a) Step-1 (Preload), (b) Step-8 (Applied Load = 220N), (c) Step-9 (Unload) .....	44
Figure 4.3: Texture comparison between EBSD & 3D-XRD, misorientation of (a) c-axis with BD, (b) c-axis with LD, (c) prism plane normal with BD and (d) prism plane normal with LD.....	47
Figure 4.4: Grain size comparison between EBSD & 3D-XRD .....	48
Figure 4.5: (a) Macroscopic stress-strain plot and stress-strain plots of all grains that are matched in all steps, (b) Macroscopic stress-strain plot and stress-strain plot of hard and soft grains, c-axis	

misorientation with BD (c) of matched grains between step 2 and 8 plotted in step 2 and (d) sliced grain map in step 8.....	50
Figure 4.6: (a) Grain map and (b) stress distributions in step 4.....	52
Figure 4.7: (a) Grain map and (b) stress distributions in step 8.....	52
Figure 4.8: (a) Grain map and (b) stress distributions in step 9.....	53
Figure 4.9: Stress-based (0002) pole figures for steps (a) 1 to (i) Step-9. In (a)-(h) colors are coded based on measured stresses within grain in loading direction and in (i) colors are based on stresses in LD, S33. The size of each spot is proportional to the measured grain relative volume.....	54
Figure 4.10: (a) Schematic of a twinned grain in two layers and (b) Verification plot of the orientation between the parent and twin.....	55
Figure 4.11: Scatter plots of parent-twin pairs for (a) Step 4, (b) Step 5, (c) Step 6, and (d) Step 8. Colors represent c-axis misorientation with LD and the size of spheres are proportional to the measured relative volume for each grain.....	57
Figure 4.12: Progression of twin number and volume fraction with respect to the applied strain ...	58
Figure 4.13: Twin Local Schmid Factor as a function of twin Global Schmid Factor for twins nucleated in steps 2 to 8.....	59
Figure 4.14: The rank of twinned variant (a,d), in 4 and 5 respectively, based on Global Twin Schmid factor (b,e), in 4 and 5 respectively, Local Twin Schmid factor using the measured stress in the parent before twinning (c,f), in 4 and 5 respectively, Local Twin Schmid factor using the measured stress in the parent after twinning.....	61
Figure 4.15: (a) S11, (b) S22, (c) S33 of the parent and twin pairs in step 4 and (d) S11, (e) S22, (f) S33 of parent and twins in step 5.....	62
Figure 5.1: Diffraction patterns in (a) Step-3, (b) Step-4, (c) Step-5, and (d) Stress-strain curves of in-situ and ex-situ experiments.....	66
Figure 5.2: (a) Macroscopic stress-strain plot and stress-strain plots of all grains that are matched in all steps, (b) Macroscopic stress-strain plot and stress-strain plot of hard and soft grains. The c-axis misorientation with LD of Step-1 & 5 matched grains are plotted in (c) step 1 and (d) sliced grain map in step 5.....	69
Figure 5.3: (a) Grain map and normal stresses (b)S11, S22, and (c)S33 distributions in step 3.....	70
Figure 5.4: (a) Grain map and normal stresses (b)S11, S22, and (c)S33 distributions in step 4.....	71
Figure 5.5: (a) Grain map and normal stresses (b)S11, S22, and (c)S33 distributions in step 5.....	71
Figure 5.6: Pole figures of steps 1 to 5: each dot resents a grain, and the size of the dot is proportional to the measured grain volume. Dots are color codes with respect to the measured stress.....	73
Figure 5.7: Grain maps of parent grains and twins in (a) Step-2, (b) Step-3, and (c) Twin volume fraction.....	74
Figure 5.8: Twin Local Schmid Factor (LSF) vs Twin Global Schmid Factor (GDF) in (a) Step-2 and (b) Step-3.....	75
Figure 5.9: The rank of twin variants: Global and local ranks based on stresses prior to twinning and after twinning in step-2, (a)-(c), and step-3, (d)-(f), respectively.....	76
Figure 5.10: normal stresses in the twins as a function of the stresses in their parents: S11, S22, and S33, in step-2, (a)-(c), and step-3, (d)-(f), respectively.....	78
Figure 5.11: Residual stress distributions for current and past experiment. (a) – (c) is S11, S22 and S33 distributions respectively for current experiment.....	79

## List of Acronyms and Symbols

### Acronyms

HCP	Hexagonal close-packed
FCC	Face centered-cubic
BCC	Body centered-cubic
3D-XRD	Three-dimensional X-ray diffraction
CRSS	Critical resolved shear stress
SF	Schmid factor
GSF	Global Schmid factor
LSF	Local Schmid factor
SEM	Scanning electron microscope
EBSD	Electron backscatter diffraction
CPFE	Crystal plasticity finite element
COM	Center of mass
BD	Beam direction (i.e. x-axis) – The axis parallel to the incoming beam vector.
TD	Transverse direction (i.e. y-axis)
LD	Loading direction (i.e. z-axis) – The axis parallel to the direction of the load

### Symbols

$\theta$  – Beam diffraction angle

$\mu$  – Angle between the radial axis of the peak and vertical axis (Shown in figure 2.9 and 3.7a)

$\omega$  – Angular rotation around the loading direction, LD

$\lambda$  – Beam wavelength

$S_{11}$  – Stress in the beam direction (x-axis)

$S_{22}$  – Stress in the transverse direction (y-axis)

$S_{33}$  – Stress in the loading direction (z-axis)

# Chapter 1

## 1. Introduction

### 1.1 Motivation

#### 1.1.1 Industrial Applications of Zirconium Alloys

Zirconium has been extensively used in nuclear industry due to its low neutron capture cross-section, exceptional corrosion-resistance in hot water, and good mechanical properties [1]–[5]. In Canada, 16% of electricity needs are provided by the nuclear industry. More importantly, 60% of Ontario's power is provided by nuclear energy. With the continued growth of the nuclear industry, the amount of carbon dioxide emissions is expected to reduce by 30 million tons per year in 2030 [6]. This shows that the nuclear energy plays a vital role not only in supporting the population's electricity needs but also in the reduction of the greenhouse gases. Zirconium alloys are mainly used in the core of the CANDU (CANada Deuterium Uranium) reactors [2]. The outermost tube of a CANDU reactor is called calandria tube and is made of Zircaloy-2, composing of 1.5 wt% of Tin (Sn), 0.12 wt% of Iron (Fe), 0.10 wt% of Chromium (Cr), and 0.05 wt% of Nickel (Ni). Heavy water is used to fill the Calandria as neutron reflector and moderator. Hot heavy water runs through zirconium pressure tubes which is enclosed by the calandria tube, but is separated by a ring from it. The casing of the Uranium (U-235) fuel rods, known as fuel cladding, is made of Zircaloy-4 [1], [4]. The constant usage of Zirconium alloys is primarily based on its low neutron capture cross-section thereby permitting the use of natural Uranium rather than the enriched one. Using heavy water with Hydrogen-2 (Deuterium) instead of Hydrogen-1 as coolant for the fuel rods is an additional approach to reducing the overall neutron capture cross-section of the system [3].

Deformation of pressure tubes can be categorized into three groups. The first is diametral expansion, which occurs because of irradiation enhanced creep and the hoop stresses induced by pressurized heavy water. The second is cylinder ovality due to applied external pressure. Furthermore, creep sag is observed due to the heavy load of fuel channel. Hence, understanding the fundamentals of the deformation mechanisms in Zirconium is essential in predicting service life of the core components and improving their performance [2], [3], [5].

## 1.1.2 Industrial Applications of Magnesium Alloys

Implementation of lightweight materials in the world of transportation can lead to numerous benefits such as reduced CO<sub>2</sub> emissions. Therefore, investigation and study of lightweight materials is a must [7], [8]. Magnesium alloys, with light weight, are shown to possess excellent properties such as high specific strength, low density and recyclability. However, magnesium alloys have hexagonal close-packed (HCP) crystal structure where dislocation movements can only occur on the basal or prism planes making it highly resistant to deformation at room temperature. Formability, on the other hand, is possible at higher temperatures. Mg AZ31 is an alloy of magnesium where A stands for aluminum, Z stands for zinc and 31 stands for the composition percentages of both elements respectively [9]. Due to lack of easy slip system, deformation twinning is very active in MgAZ31. Twinning is a deformation mechanism where a portion of a grain is re-oriented resulting in significant texture evolution, and is accompanied by a significant shear strain, eg. 13% for Magnesium. Hence, twinning may improve the ductility of the material, but specific twin boundaries can act as crack nucleation site due to high stress concentration resulting from the shear transfer. Thus, an accurate model that captures key aspects of twinning would be an asset for estimating the mechanical behavior of magnesium and other HCP alloys [10].

## 1.2 Scope of this research

The objectives of this research are to investigate the mechanical behavior of HCP materials at macro- and meso-scales. This research specifically focuses on deformation twinning in dog-bone samples of pure Zirconium and Magnesium alloy AZ31B. An X-ray diffraction characterization technique is used to investigate elastic and plastic deformation at the grain level at different loading steps. Prior to the experiment, pre-experimental procedures, including heat treatment and polishing, were carried out on the samples to generate the right material texture that activates twinning. Statistical data acquired from these experiments will help us understand the underlying mechanism of twin formation and the parameters that affect twin nucleation. Investigating two separate materials with the same crystal structure, ie HCP, can give us an insight on the generic mechanisms that exist in HCP crystals.

## 1.3 Outline

Chapter 1 provides a general overview of the field and the objectives of this research. In chapter 2, a literature review is conducted on deformation twinning and advanced characterization techniques. Chapter 3 discusses the experimental procedure that was followed, starting from sample preparations that were done prior to the synchrotron experiments to the post-processing of the raw diffraction data measured at the ESRF. This chapter is categorized into three sections, preparation before experiment, experimental procedure, and data post-processing. Two in-situ experiments on two different specimens, zirconium and magnesium, are conducted and the results of the processed data are provided in chapter 4 and chapter 5. Chapter 4 and 5 provide summaries of the results and focus on deformation twinning in zirconium and magnesium, respectively. Finally, chapter 6 ends the thesis by stating the concluding remarks and discussing future work.

## Chapter 2

### 2. Literature Review

This thesis focuses on investigating tensile twinning in HCP metals through the use of an in-situ diffraction technique. Therefore, a brief review of the previous works is presented to understand the current state of the art. This chapter focuses on explaining deformation mechanisms in HCP metals specifically in Zirconium and Magnesium. Some of the existing and relevant characterization techniques are also discussed.

#### 2.1 Deformation Mechanisms in HCP metals

In a unit cell of an HCP crystal,  $a_1 = a_2 \neq c$  and  $\alpha = \beta = 90, \gamma = 120$ . Unlike cubic crystals, deformation systems in HCP metals are not spread out in a symmetrical fashion. In addition, due to having low symmetry in the crystal, slip systems are not as numerous as cubic crystals. As a result, deformation along the c-axis of the crystal (see Fig 2.1) is mainly accommodated by twinning. The c/a ratio is an important metal-specific character that essentially determines the possible deformation mechanism. HCP metals can be classified into two groups, in terms of the active slip plane [10]; the first group has  $c/a > 1.633$  and the other has  $c/a < 1.633$  as summarized in figure 2.1.

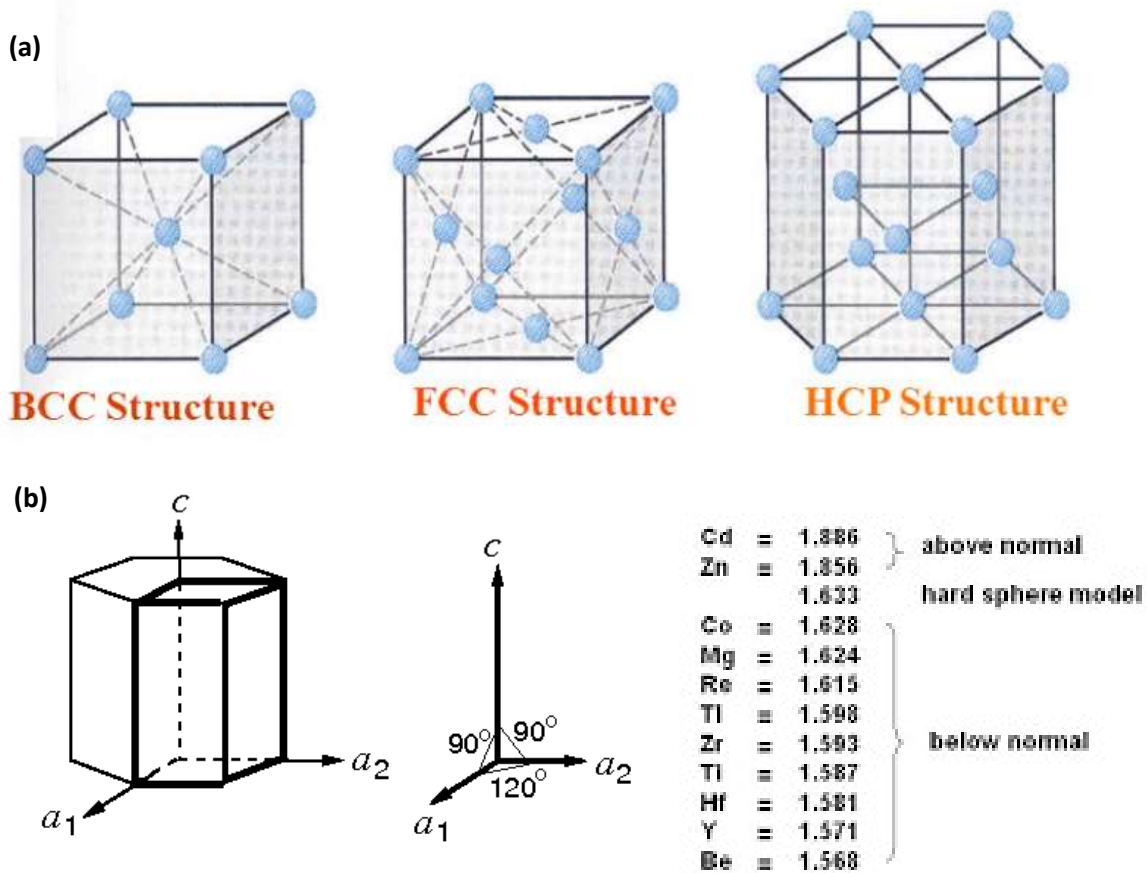


**Figure 2.1: (a) Unit cells of BCC, FCC and HCP crystals, (b) The  $c/a$  ratios for different HCP metals [11]**

Unlike face-centered cubic (FCC) and body-centered cubic (BCC) metals, the slip systems in HCP metals are limited leading to various alternative deformation mechanisms. Primary, secondary slip and twinning systems exhibit different critical resolved shear stresses (CRSS). Possible active slip systems of an HCP crystal are summarized in table 2.1.



**Table 2.1: Slip systems in HCP metals [12]**

Slip System	Burgers vector type	Slip Direction	Slip Plane	No. of Slip Systems
1	a	$\langle 11\bar{2}0 \rangle$	basal $\{0001\}$	3
2	a	$\langle 11\bar{2}0 \rangle$	prism type I $\{10\bar{1}0\}$	3
3	a	$\langle 11\bar{2}0 \rangle$	1 <sup>st</sup> -order pyramidal type I $\{10\bar{1}1\}$	6
4	c+a	$\langle 11\bar{2}3 \rangle$	2 <sup>nd</sup> order pyramidal type II $\{11\bar{2}2\}$	12

If the local stress of a specific slip system exceeds its CRSS, then this slip system is assumed active. CRSS of a specific slip system depends on several factors, including c/a ratio and temperature. Generally, there are three laws that govern the activation of slip system in any crystal structure [11].

- 1) The crystal operates on the slip system that has the largest difference between the resolved shear stress and its CRSS.
- 2) The slip plane is the plane with the largest number of atoms packed on it or in other words, its atomic density is the largest.
- 3) The slip direction is the one with the shortest burger vector (i.e. the distance between two atoms on that plane is the shortest)

These laws are all established in the past in Schmid's law of resolved shear stresses [13], 1<sup>st</sup> law, and Peierls-Nabarro model [14], [15], 2<sup>nd</sup> and 3<sup>rd</sup> law. The Schmid's law was initially discovered through experimentation and then Schmid's factor was later developed. The Peierls-Naborro model deals with the atomic interactions and the forces involved in these interactions.

Considering a uniaxial load applied on a polycrystalline material, the resolve shear stress ( $\tau_0$ ) acting on a specific slip system can be found using the magnitude of the applied load following :

$$\tau_0 = (F/A)\cos\phi\cos\lambda \quad (2.1)$$

where  $F$  is the applied force,  $A$  is cross-sectional area of the specimen,  $\phi$  is the angle between the slip plane normal and the direction of the applied load, and  $\lambda$  is the angle between the slip direction and force direction. The Schmid factor,  $m$ , is given by,

$$m = \cos\phi\cos\lambda \quad (2.2)$$

This is the global Schmid factor due to the angular relations with respect to the direction of the applied load. In a polycrystalline material, each grain has a specific averaged local stress tensor depending on the interactions with the neighboring grains and the load applied. Therefore, the local Schmid factor can be found using the local stress tensor. The generalized form of Schmid factor for the case where state of the stress is tri-axial is given by [16]:

$$SF^\alpha = \frac{P^\alpha : \sigma}{\|\sigma\|} \quad (2.3)$$

where  $SF^\alpha$  is the Schmid factor for the slip system,  $\alpha$ , and  $\sigma$  is the stress tensor. To find the local Schmid factor, local stresses can be used in Eq. 2.3.

## 2.2 The Mechanism of Deformation Twinning

When there is a lack of easy slip systems, twinning may become active. Twinning can be defined as the reorientation of a portion of lattice. The twinned domain is a reflection of the parent domain against the twin habit plane [17], [18]. Different twin types can form depending on processing. Annealing twins form during heat treatment or recrystallization. Annealing twins are profound in Nickel alloys. Transformation twins are another type of twins that form during martensitic phase transformation; this is common in shape memory alloys. In martensitic transformation, transformation twins normally form with a fixed size ratio and the boundaries interconnecting them are highly glissile thereby raising its plasticity. Lastly, deformation twins are accompanied by large shear strain on the twin plane. In contrast to transformation twins, the deformation twins are thin layers of atoms, as shown in figures 2.2 (c) and (d), embedded within a matrix and their boundaries are migratable thus enhancing metal ductility [18], [19]. The main focus in this research is to observe deformation twinning (tensile twinning) in two different HCP metals. There are two different types of deformation twinning: tensile twinning and compressive twinning. Tensile twinning is the most common type of deformation twinning and it is often referred to as “normal” twinning [11]. Tensile twinning happens on the  $\{10\bar{1}2\} <$

$10\bar{1}\bar{1}$  system, where atoms on the opposite side of the plane are glided rather than shifted in the case of slip mechanism as shown in figure 2.2 (b).

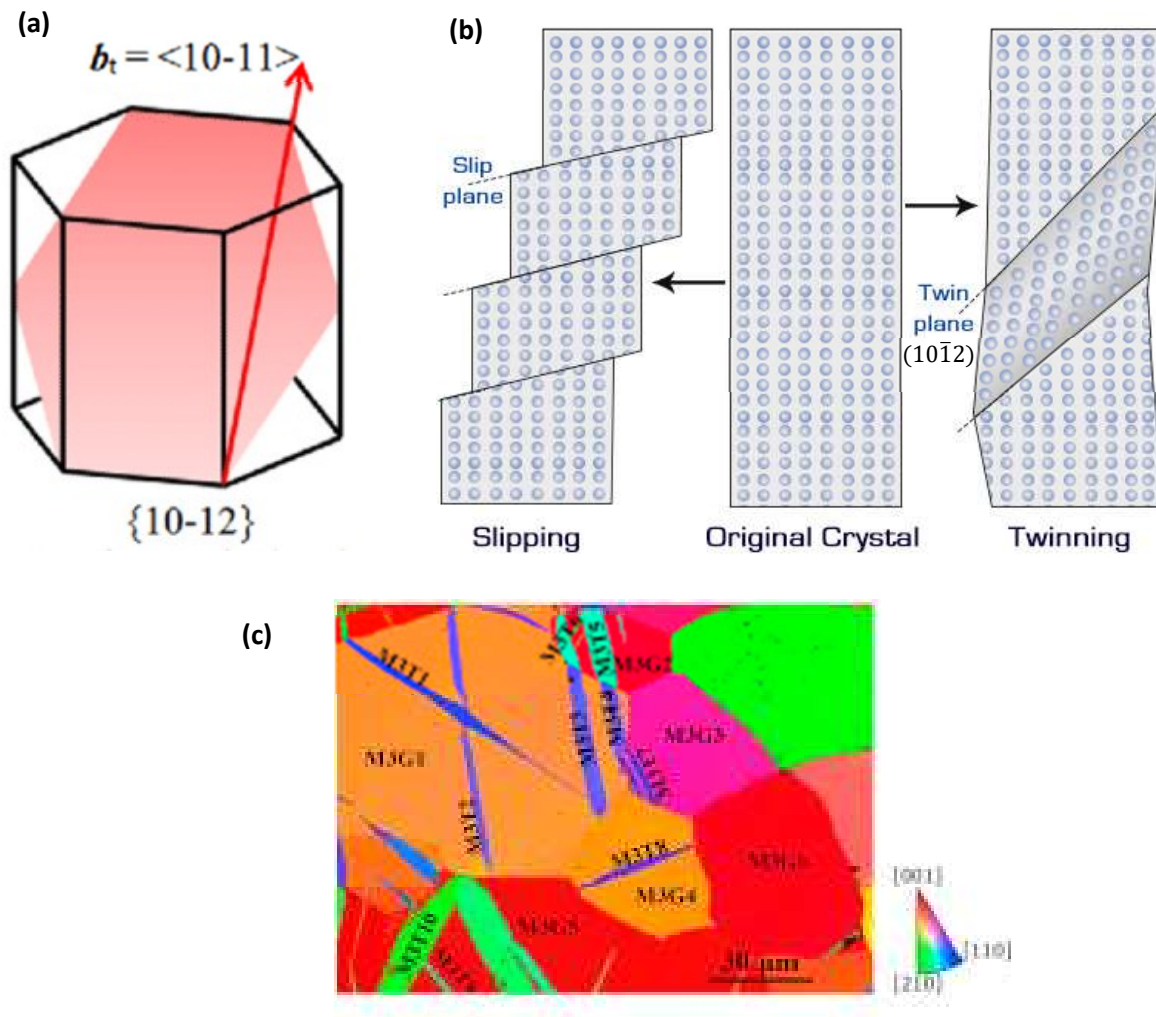


**Figure 2.2: (a) Tensile twinning system in HCP unit cell, (b) Twinning and slip mechanism (c) Deformation Twins detected captured through EBSD labelled as ‘MXTX’ and X is a number [20]**

Understanding the crystallography of twinning has been a vital step towards understanding deformation twinning. From the theory of deformation twinning, atomic displacements in the parent lattice assists in re-orienting a part of the lattice and these displacements are equivalent to simple shear. The twinning (“invariant”) plane is called  $K_1$ , and its shear direction is  $\eta_1$  while the undistorted plane is called  $K_2$ . The plane containing the invariant,  $K_1$ , and undistorted,  $K_2$ , plane normals and the invariant shear direction,  $\eta_1$ , is the plane of shear defined as P. The intersection of the plane of shear, P, with the undistorted plane,  $K_2$ , is the undistorted shear

direction,  $\eta_2$ . This schematic, shown in figure 2.3 (a) of crystallographic twinning is conducted to distinguish between type I, reflection off a plane, and type II twin, rotation around an axis.

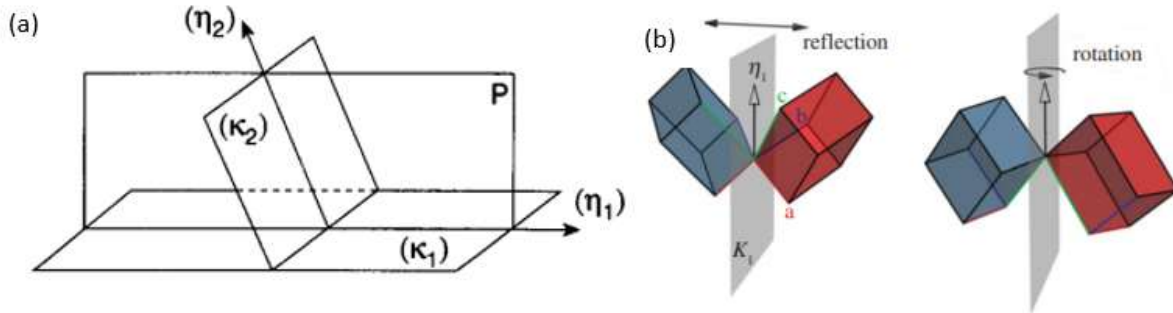


**Figure 2.3: (a) Labeled schematics of twinning elements and plane of shear, P, [18] (b) Type I and Type II twins respectively [21]**

Twinning mode can be identified either when  $K_1$  and  $\eta_2$  are fixed or vice versa ( $K_2$  and  $\eta_1$ ) [18]. Several other models are also used to view geometric alterations in the lattice structure [12].

**Table 2.2: The six variants of tensile twins [18]**

	h	k	i	l	u	v	t	w
<b>V1</b>	1	0	-1	2	-1	0	1	1
<b>V2</b>	-1	1	0	2	1	-1	0	1
<b>V3</b>	-1	0	1	2	1	0	-1	1
<b>V4</b>	0	-1	1	2	0	1	-1	1
<b>V5</b>	1	-1	0	2	-1	1	0	1
<b>V6</b>	0	1	-1	2	0	-1	1	1

The twinning elements of these normal twins are,

$$K_1 = \{10\bar{1}2\}, K_2 = \{\bar{1}012\}, \eta_1 = \langle 10\bar{1}\bar{1} \rangle, \eta_2 = \langle \bar{1}01\bar{1} \rangle, P = \{1\bar{2}10\}$$

Based on the twinning elements, the mis-orientation between the c-axes of the parent and the twinned lattice is 85.2 degrees for a c/a ratio of 1.523 (Zirconium). The hexagonal symmetry results to six variants of  $\{10\bar{1}2\} \langle \bar{1}011 \rangle$  which are listed in table 2.2. The activity of each variant depends on the local stress and crystal orientation.

## 2.3 Evolution of Deformation Twins

In general, deformation twinning can be divided into four steps. In the first step, called nucleation, dislocations accumulate to potential twin regions within the grain. Once these dislocations attain a critical value, a successful twin is formed. This is the second step. In the third step, known as propagation step, the formed twin extends as a line crossing the entire grain and in the final step, this propagated twin thickens. Deformation by slip is a gradual process that involves movement of dislocations through the lattice however twinning is a sudden reorientation in the crystal thereby making it difficult to extract its CRSS [4], [19]. A study on Zinc has discovered that the stress required to nucleate twins is higher than the stresses required to propagate and thicken the twins [22]. The stresses required to propagate and thicken a twin varies greatly from one grain to another. When twins are nucleated, the stresses are concentrated at the tip, and this enforces the nucleated twins to propagate at an approximately sonic velocity [23].

### 2.3.1 Schmid Factor

Studies have shown that the Schmid factor plays an important role when it comes to investigating twins [24]–[26]. Godet et al. [24] investigated the role of Schmid factor in the tensile twinning of an AM magnesium alloy tubes. To easily define the twin variants, the initial texture was optimized for twinning. Tensile twinning was observed to occur in crystals with high Schmid factor. In other study [25], significant deviation from the maximum Schmid factor criterion was observed in over 300 deformation twins in alpha-Zirconium. This study concluded that the local stresses have a significant impact on the twin nucleation in HCP metals. The effects of local stresses and Schmid factor on twin nucleation in pure titanium was studied by Guo and Abdolvand [26], thereby disregarding the direct effect of external loads. A smooth correlation was found to exist between the maximum LSF and the active twin variant, while external load showed to play a less significant role.

### 2.3.2 Neighboring effects

Studies show that local Schmid factor is not the only parameter that affect twin nucleation [27], [28]. Neighboring grains and their misorientations are important in predicting twin nucleation in the parent grain. When twins are formed near the grain boundary, the neighboring grain must accommodate the alterations in the crystal geometry [27]. Therefore, the amount of deformation

in the neighboring grain that is essential to compensate for its shape change plays an important role. For example, if considerable amounts of prismatic glide are required in neighboring grain but the shape change cannot be accommodated, twins will not nucleate, and internal strains will grow high within the grain and this is mainly observed in Mg alloys [27]. Similarly, a crystal, with a low Schmid factor, may have twins when the required prismatic glide to be accommodated by the neighboring grains is considerably low. Moreover, misorientation of neighboring grains is an essential factor in determining the thickness of twins. A study has demonstrated that an existence of low misorientation between c-axes of the neighboring grains and parent grain would essentially ease the thickening process of the propagated twins [29]. Furthermore, several other interesting studies show that neighboring grains can affect the propagation process of twin embryos [30], [31]. When the misorientation between the c-axes of the neighboring grains and parent grain is low, twin embryos do not only propagate within the grain, but it extends to the neighboring grain. An important factor that decides this behavior (twin transmission) is the plastic anisotropy of the material. Plastic anisotropy in HCP metals is the difference between the CRSS of different slip modes, including basal  $\langle a \rangle$ , prism  $\langle c \rangle$ , and pyramidal  $\langle c + a \rangle$ .

Plastic anisotropy in HCP metals is large when compared to other FCC and BCC metals. In the study by Kumar et. al. and Beyerlin et. al. [30] twin transmission was investigated in three different HCP polycrystals, Ti, Mg, and Zr, where zirconium had the greatest plastic anisotropy and magnesium had the lowest. Among the three samples, zirconium showed the highest probability of twin transmission thus concluding that increase in plastic anisotropy promotes twin transmission.

### 2.3.3 Size effects

The variation of yield stress ( $\sigma_y$ ) in metals with grain size ( $d$ ) is known as Hall-Petch effect:

$$\sigma_y = \sigma_0 + kd^{-\frac{1}{2}} \quad (2.4)$$

where  $\sigma_0$  and  $k$  are material parameters. Likewise, grain size was also found to play a role in twin nucleation. Several studies have shown that formation of twins vary from small to large grains and others showed that the grain size effects are minimal. Studies have shown that the number of twins increase with increasing grain size [32]–[35]. For instance, Ghaderi et al. [32]

have studied the effect of grain sizes in magnesium and titanium on twinning. Twin volume fraction was found to increase with grain size in titanium while no such effect was observed in magnesium. Twin length varies significantly with grain size in both titanium and magnesium. However, in coarse grains ( $> 30$  microns), twins do not propagate through the whole grain due to twin impingement and high concentrative stresses near grain boundaries. Another study showed that grain size in zirconium has no impact on twin thickening but depends on the c-axes angular misorientation between the parent grain and neighboring grains. The number of twins increase with grain size, but the twin area fraction remained the same over different grain sizes [35].

### 2.3.4 Residual Stresses

Due to high anisotropy in elastic modulus and thermal coefficient of expansion of zirconium crystals, high levels of residual stresses can build up even after recrystallization and heat treatment. Thermal residual stresses in magnesium samples are much smaller since the degree of anisotropy in the elastic modulus of magnesium is much lower. Residual stresses can impact the stress evolution with a grain, which can subsequently affect the prediction of deformation modes [36], [37].

### 2.3.5 Stresses in Parents and Twins

Comparisons between the stress states in parent and twin grains were studied to understand the behavior of the twinned grain and the polycrystal [38]–[41]. Aydiner et al. [38] carried out an experiment to investigate a twin within a parent grain during compression of an Mg alloy with the c-axis of the parent grain approximately perpendicular to the loading axis. The stress state of the twin was found to be lower than its parent grain. Bieler et al. [41] carried out an experiment on a strongly textured grade 1 Titanium under tension where the average orientation of the c-axis was close to the loading axis. Three parent-twin pairs were investigated separately, where two of them were surrounded by soft grains while the third pair was surrounded by hard grains. The stresses in the loading direction of the parent grains surrounded by soft grains increased after twin nucleation. Meanwhile, the stresses in the loading direction of the parent grains surrounded by hard grains decreased after twin nucleation. These results support the theory of slip transfer from neighboring to parent grains. In all pairs, the stresses in twins were 10%-30% lower than the parent grains. Similarly, Abdolvand et al. [40] has conducted a tensile experiment on Zircaloy-2 and the stress-states in nearly 200 twins were investigated. Normal stresses of parent

grains in global coordinate was higher than those of twins. However, when those stresses were transferred to the local coordinate, the stresses of the parents and twins were similar in all directions except for  $\sigma_{22}$  &  $\sigma_{13}$ . The differences in those two stresses can be explained by the force continuity, twin transformation strain, and back stresses induced by formation of twins. Another study [39] performed on Zircaloy-2 revealed that the favored nucleation sites for twins in parent grains the highly stressed regions. These regions usually exist near grain boundaries that are shared between three or more grains due to the development of high stress concentrations. In general, RSS or Schmid factor are not the sole factors in determining twin nucleation. The c-axis misorientation of neighboring grains play an essential role in determining twin nucleation and the overall stress state in parent grains due to slip transfer. Moreover, understanding the interactions occurring at the twin habit-plane can aid us in predicting the stress-field pattern across the twin habit plane.

### 2.3.6 Twin Volume Fraction

There is a relationship between the accommodated strain and the number of twins, and twin volume fraction [42]–[45]. However, when studying the relationship, several other factors must also be considered. For instance, a sample with an unfavorable texture for twinning will barely have twins irrespective of the applied strain. The formed twins have significant effects on the work-hardening of the material and they can be seen in the macroscopic true stress-strain curves [42], [46]. Tensile and compression experiments on magnesium AZ31 alloy were conducted by Chun et al. [42] to understand these trends. Chun et al. [42] demonstrated that the trend existing between the strain and formation of twins is a sigmoidal relationship expressed as,

$$\chi = 1 - e^{-4.2\frac{\epsilon}{\epsilon_t}} \quad (2.5)$$

where  $\chi$  is the fraction of tensile twins,  $\epsilon_t$  is the macroscopic strain. Using this equation and work hardening laws, the overall flow stress was also predicted.



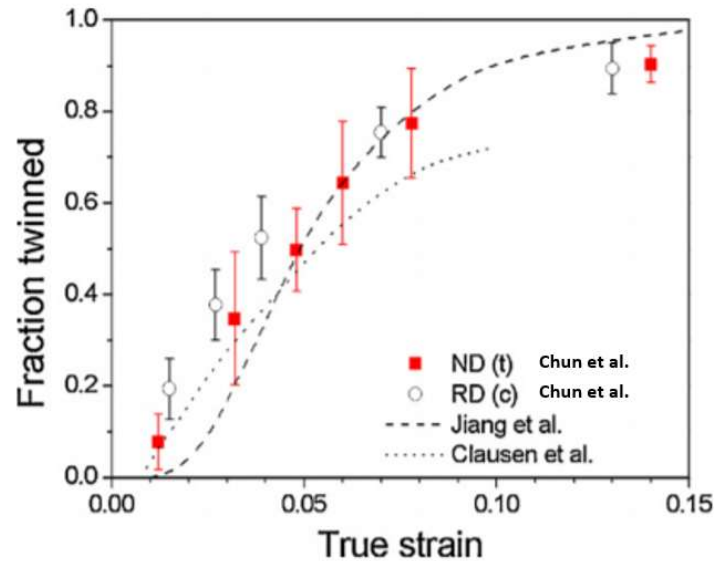


**Figure 2.4: Twin volume fraction against applied strain [42]–[44]**

### 2.3.6 Modeling

Several approaches have been used to study twin formation and twin-parent as well as twin-neighbor interaction. The two common modelling techniques used in simulating deformation of polycrystals at the meso-scale are self-consistent modeling and finite element analysis. In self-consistent modelling, each grain act as an elliptical inclusion in an infinite homogenous matrix and the properties of which is the average properties of all grains except the one under investigation. This means that the elastic and plastic interactions between the grain and matrix can be captured, however the direct grain-grain interactions are neglected. In crystal plasticity finite element (CPFE) framework, the whole geometry of the grains and their orientations are modelled. Depending on the model and element size, a single grain can have more than one element thereby integrating the feature of demonstrating the variation of mechanical response within a single grain. The downside of finite element modeling, in contrast to self-consistent modelling, is its computational cost. Therefore, a compromise is required between the computational time and element size. Modeling extends beyond the scope of this work but acquired results from conducted experimental work will be used for comparison and validation of a CPFE model [47], [48].

## 2.4 Experimental and characterization techniques

Deformation of polycrystalline materials depend on several parameters including elastic and plastic properties of the material, crystal structure, the orientation of individual the grains, and the texture of the material. The mechanical response of a single crystal can vary from one crystallographic plane to another depending on the interplanar spacing. For instance, loading an HCP material along the basal plane will result in a different mechanical response compared with loading along the prism plane. This results in plastic anisotropy. Hence, understanding the orientation distribution, also known as texture, of the HCP crystals within the specimen will help comprehend local deformation mechanisms. Different techniques are developed to study the effects of materials texture on deformation mechanism, yet what all have in common is that they are all based on Bragg's law. These techniques can be categorized into two groups, macroscopic and microscopic measurement.

### 2.4.1 Diffraction Basics: Bragg's Law

When beams of electrons, X-rays or neutrons strike on lattice, the reflected beams will either interfere constructively or destructively. Based on the cumulative effect, beams that were interfered destructively would fade whereas the constructively interacting beams would become stronger and appear as a strong peak on the detector. Bragg law states that the condition for an incident beam, with the wavelength of  $\lambda$ , to diffract constructively is

$$n\lambda = 2d\sin\theta \quad (2.6)$$

where  $n$  is an integer,  $d$  is the interplanar spacing between the atomic planes, and  $\theta$  is the scattering angle of the diffracted beam or half the angle between the incoming and diffracted beams (see figure 2.5 (a)). In a single HCP crystal, atoms can have different plane arrangements where Miller indices are used in defining the direction of these planes. Using the Miller indices, the interplanar spacing for an HCP crystal can expressed as,

$$\frac{1}{d_{hkil}^2} = \frac{4}{3} \left( \frac{h^2 + hk + k^2}{a^2} \right) + \frac{l^2}{c^2} \quad (2.7)$$

where  $a$  and  $c$  are the unit cell parameters representing the atomic spacing on the basal plane and along the crystal  $c$ -axis (see figure 2.1 (b)). Depending on the size of the detector and the

distance between the sample and detector, the wavelength (energy) of the beam can be adjusted to successfully capture as many  $2\theta$  values as possible. [49]

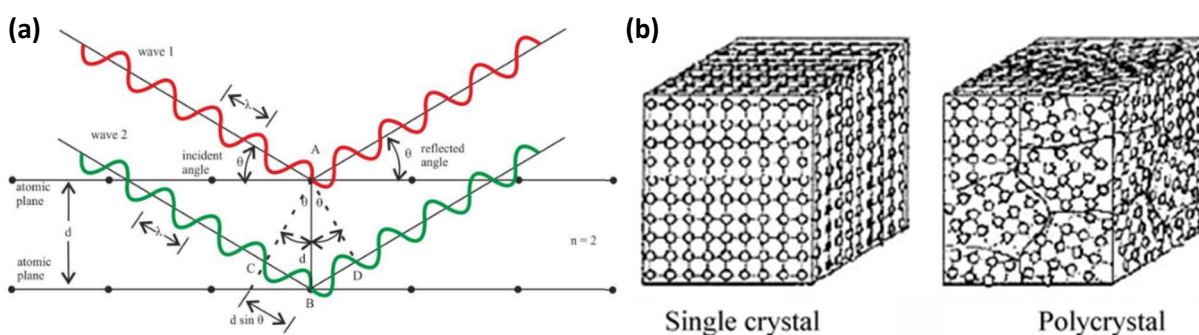


**Figure 2.5: (a) labelled Bragg's condition, (b) single crystal and polycrystal morphology**

While  $2\theta$  of any crystallographic plane can be measured using the Bragg's law, understanding the intensity of the diffracted beam from a crystallographic plane is quite complex and involves implementation of several factors. An important feature that can be acquired through intensity is the volume fraction of the specimen containing those diffracted planes (i.e.  $\alpha$ -phase,  $\beta$ -phase). The main factors involved in adjusting the intensity are scattering, multiplicity, Lorentz, and polarization factor. Scattering factor is a mathematical expression of the scattering of an incident beam by all atoms in a unit cell. Multiplicity factor is the total number of planes with similar interplanar distances. Lorentz factor is the factor that expresses the relative time spent by the beam during a reflection in a specific lattice plane. Polarization factor is a factor that represents the scattering of unpolarized rays through the interplanar spacing (i.e. slit) thereby reducing its intensity. Furthermore, absorption coefficient is a number that accounts for the amount of x-ray absorbed by the specimen. The mathematical formulation and the details of these factors will be discussed briefly in the experimental technique used in this work. [50]–[52]

## 2.4.2 Texture measurement

Beams of X-rays, neutrons or electrons can be used for texture measurement. However, the spatial resolution of each technique is different [53].

### 2.4.2.1 X-ray

X-ray is a form of electromagnetic radiation with a wavelength shorter than UV rays and visible light but longer than gamma rays. The radiation energy of a typical X-ray is ranged from 0.1 keV to 100 keV. Low energy X-rays are used to study the atomic structure of a material based on

the X-ray absorption spectroscopy (XAS) pattern while high energy X-rays are used for studying crystal structures through diffraction pattern analysis. Acceleration of charged particles is the most common method to produce X-rays. Synchrotron radiation involves bending magnets that controls the path of electrons (charged particle) produced by electron guns. The acceleration of an electron going around a circle (i.e. radial acceleration) leads to emission of X-rays. The emitted beam enters through a series of focusing techniques to strike the specimen. This can be used in measuring the macrottextures of material with known lattice parameters and a fixed Bragg's angle for its hkl planes. The term macrottexture refers to the texture measured for the entire sample (normally more than 1000 grains). During the diffraction process, X-rays can be absorbed by the material, thus limiting its penetration depth. Mass absorption coefficients are measured in  $\text{cm}^2/\text{g}$  and this represents the amount of X-ray flux absorbed per single gram of the specimen. The larger the atomic number 'Z' of an element, the higher the mass absorption coefficient. For instance, the mass absorption coefficient of zirconium, based on figure 2.6, starts sloping at a very low wavelength, and the discontinuity at  $\sim 0.06$  nm is a result of electron excitation at K-edge. Therefore, high energy X-rays are used to avoid the undesirable high absorptions. [49], [53], [54]

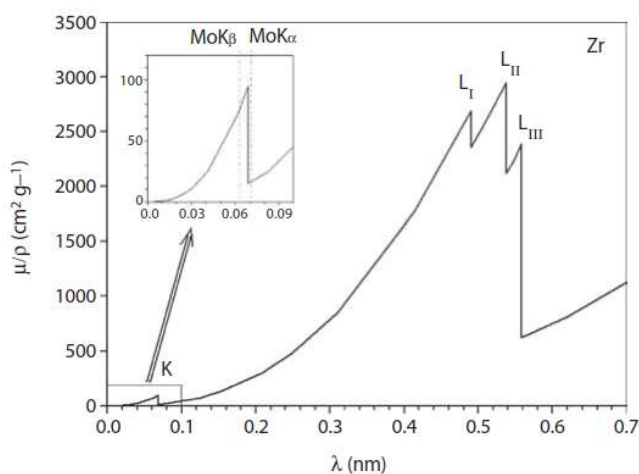


**Figure 2.6: Variation in the mass absorption coefficient with x-ray wavelength showing the K-edge and L-edge [53]**

### 2.4.2.2 Neutron

Neutron is a subatomic particle with no net electric charge and a slightly larger mass than a proton. Neutron diffraction techniques can only be used in very specific cases where its

advantages defeat those of X-ray. For example, investigating zirconium macrotexture via neutron diffraction is quite ideal due to its low neutron capture cross-section. Neutrons can be generated either through fission of uranium in nuclear reactors [1], [3]. The situations where neutrons can provide an advantage over x-rays are as follows;

- Size: Investigating a bulk sample due to the materials irregular shape or small volume fraction of a second phase crystal. In addition, texture of a large grained specimens cannot be acquired through x-ray diffraction due to its penetration limit. Unlike X-ray, neutron do not interact with the cloud of electrons around the atoms and has high penetration depth.
- Speed: A good example is investigating texture evolution based on the mechanical response of a specimen.
- Irregular microstructure: Low crystal symmetry or multiphase materials require large statistics for validity which is time consuming to obtain with x-ray diffraction.

### 2.4.2.3 Electron

Unlike X-rays and neutrons, electrons are charged subatomic particles that interact with the material through Coulomb forces. Compared to X-rays and neutrons, the interaction volume is small allowing diffraction from a portion of individual grains rather than a volume or families of grains. However, electrons interact with the material thereby having very limited penetration depth resulting in only surface measurement. Those signals emitted from electron-matter interaction can be used for different types of studies including the analysis of chemical composition, microstructure, and grain orientations (i.e. microtexture). Examples of such signals are shown in figure 2.7. For example, reflected X-rays from a sample, as a result of the electrons interaction with atom, can be used in a procedure known as micro-Kossel technique to investigate local orientations. [53], [55], [56]

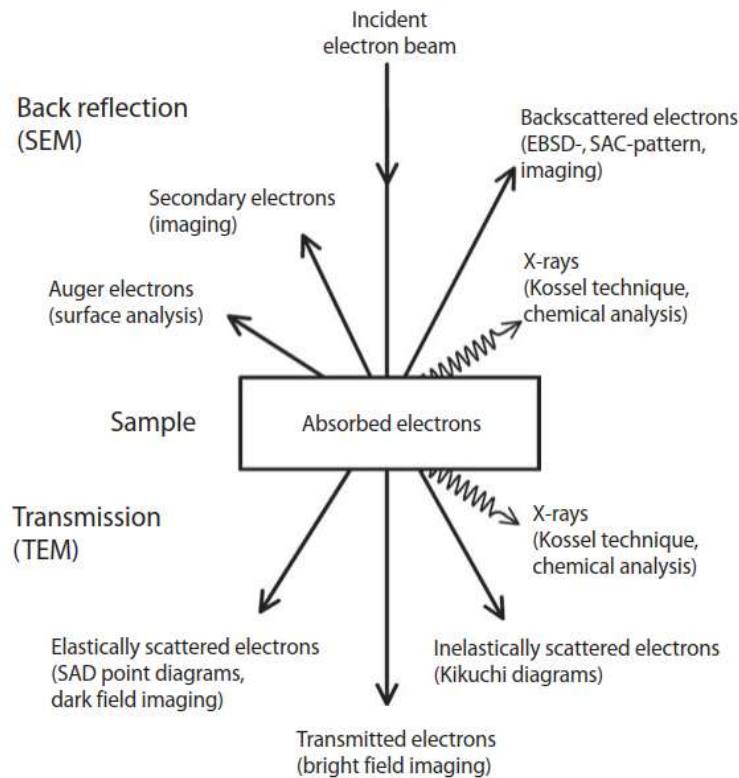


**Figure 2.7: Different beams emitted during electron microscopy [53]**

## 2.4.3 Characterization Techniques

### 2.4.3.1 Single crystal X-ray diffraction and powder diffraction

One of the oldest X-ray crystallography methods is single crystal X-ray diffraction. The diffracted X-rays from a single crystal are collected on a detector as the sample rotates on a stage to pick up reflection from each set of evenly spaced planes in material. Alternatively, powder X-ray and neutron diffraction are specific to polycrystalline materials and texture measurement. A polycrystal sample may have random orientations or might be textured. Thus, some of the crystallographic planes of each grain of this polycrystal may satisfy the Bragg condition and appear on the detector. This means there is no need for sample rotation. The state of materials texture can be investigated when comparing the diffraction patterns of the randomly oriented polycrystal and a textured polycrystal. These techniques are used in measuring the macrotexture of the sample due to the large size of the incident beam striking many grains at once. Average elastic strains can be measured by measuring diffraction peak shifts. When a tensile load is applied perpendicular to one of the  $\{hkil\}$  lattice planes, the interplanar spacing between those

planes increases thereby reducing its diffraction angle. [57] The elastic lattice strain is determined as follows,

$$\varepsilon_{hkil} = \frac{d_{hkil} - d_{ref}}{d_{ref}} = \frac{\sin\theta_{ref}}{\sin\theta_{hkil}} - 1 \quad (2.8)$$

### 2.4.3.2 Electron microscopy (EM)

In a scanning electron microscope (SEM) electrons with a specific energy and wavelength strike the sample surface and interact with the atoms on the surface. The secondary electrons, subsequently emitted, can be used to study sample topology and composition. Moreover, the backscattered electrons can be used, in a method called electron backscattered diffraction (EBSD), to characterize microtexture. Microtexture is referred to the texture made by families of grains. For EBSD, the sample is tilted at an angle slightly higher than 60 degree to reduce the energy loss of the electron beam. This beam is diffracted, through Bragg's condition, and hits a phosphor screen causing it to shine and create a Kikuchi pattern. This pattern can be used to analyze the orientation of the single pixel ( $\sim 3\mu\text{m}$ ) on the surface that reflected the electron beam. Spatial resolution is the size of the pixel used in constructing the scanned area of the sample. Samples with various grain size can be used for orientation mapping starting from  $\sim 50$  nm. However, samples with average grain sizes lower than the spatial resolution of specific SEM will result to unreliable Kikuchi patterns. Nevertheless, through microdiffraction and transmission electron microscopy (TEM), spatial resolution is greatly improved for specimens with small grains. In this technique, transmitted electrons are post-processed them to retrieve microtexture information. The major drawback of this technique is the requirement for the sample to be very thin to allow electron transmission. Through utilization of this technique with recently developed techniques, like transmission-EBSD or transmission Kikuchi diffraction (TKD), two-dimensional orientation maps can be retrieved for small grains and nanoparticles with an excellent spatial resolution [53].

### 2.4.3.3 Three-Dimensional X-ray Diffraction (3D-XRD)

One of the main issues existing in the discussed techniques is the inability to capture microtexture in three dimensions. In terms of statistical representation, the limitation of EM is its low penetration depth and inability to capture texture in the third dimension (i.e. beam direction). Investigation of grain-grain interactions and local effect of neighborhood should not be limited to two dimensions and stresses in all directions should be acquired to enhance our

understanding of the physics behind the deformation mechanisms occurring in the material. Poulsen et al. [58] have developed a novel technique, called 3D-XRD, that captures materials microtexture non-destructively. The technique follows similar setup to conventional XRD with some alteration, as shown in figure 2.9. Like XRD, the sample thickness is restricted due to the attenuation issue of X-ray beam. The beam initially impinges a sample that is mounted on a  $\omega$ -stage. The  $\omega$ -stage rotates around the  $\omega$ -axis, e.g. loading direction, so that various crystallographic of individual grains satisfy Bragg's condition. The stage also allows for translation in all x, y, and z-axes as an additional option for the user to tailor the sample's position during setup. As shown in figure 2.8, three configurations are proposed for 3D-XRD depending on the problem in hand,

- Configuration A: This configuration involves a detector that is positioned close to the specimen at three different distances (4 – 8 mm) for data acquisition. While the spatial resolution is remarkable, the angular resolution is quite low, which means that elastic lattice rotations will not be precise. Therefore, only grain map and microstructure can be acquired using this configuration.
- Configuration B: This configuration involves a detector that is positioned far from the specimen (2500 mm). A fraction of the pattern or diffraction spots are captured, but at very high angular resolution. Valuable information about lattice strains and rotations can be obtained.
- Configuration C: To get a compromise between capturing the full pattern and getting adequate angular resolution, the detector is placed at a medium distance from the specimen (~400 mm). Debye-Scherrer rings consisting of individual diffraction spot will form on the detector. The captured angular resolution is lower than configuration B, yet higher than configuration A allowing for strain and rotation measurement at the level required for engineering application, i.e.  $1E-4$ .



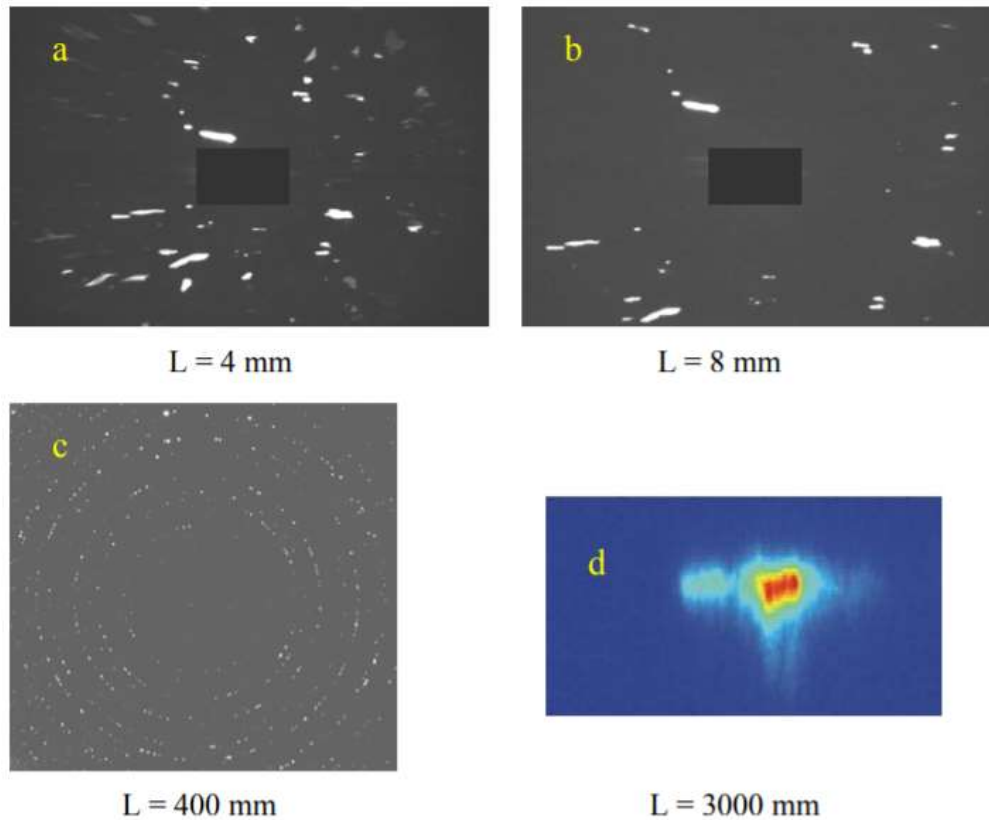


**Figure 2.8: (a) & (b) are configuration A, (c) is configuration C, and (d) is configuration B [58]**

Furthermore, the experiment can be modified by changing the cross-section of the incident beam. This also depends on the problem in hand and through experience, the possible geometries of the cross-section are divided into three categories:

- **Box Beam:** The incident beam has a square cross-section and its dimensions are much larger than the characterized microstructural elements. This allows for a full characterization in a single  $\omega$ -scan.
- **Line Beam:** The square incident beam is narrowed down in one dimension until the beam's cross-section appears as a line. This forces the sample to be divided into a set of layers with thickness equivalent to the beam's thickness. The number of layers indicate the total number of required  $\omega$ -scans to characterize the sample.
- **Pencil Beam:** The beam cross-section in this case is narrowed down in both directions until it appears as a dot compared to the scanned area. In a single  $\omega$ -scan, the beam must be probed through y and z-directions to characterize the entire sample.

It is well-known that the EBSD's microtexture is informative and reliable due to its high spatial resolution. The pencil beam setup is somewhat similar to the probing mechanism in EBSD and this makes it the best among the other beam cross-section's geometries. However, retrieving an entire scan through this geometry is time consuming. Therefore, line beam is mostly used as a compromise for spatial resolution and scanning time.

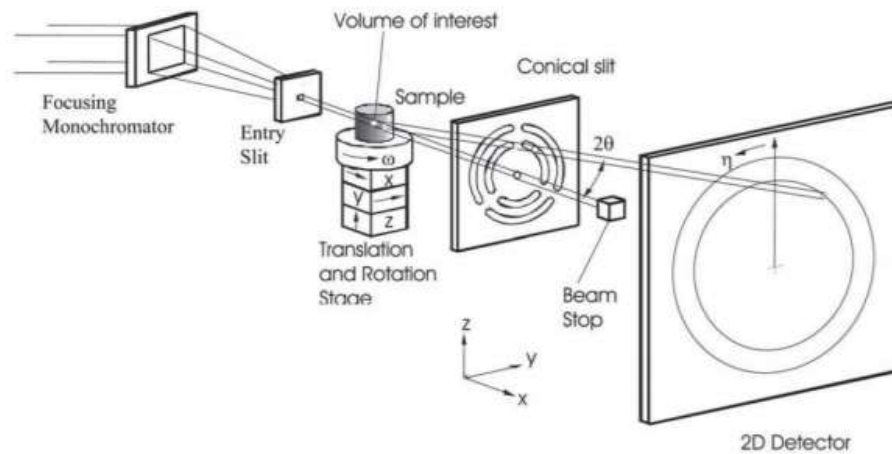


**Figure 2.9: Schematic of 3D-XRD [58]**

#### 2.4.3.4 Alternative techniques

Differential aperture X-ray microscopy (DAXM) [59], [60] and diffraction contrast tomography (DCT) [61] are other advanced 3D microscopy techniques that can be used to capture the microtexture of a sample (see figure 2.10). An additional advantage of these techniques over 3D-XRD is that they capture the grains' morphology. However, in both techniques the number of grains is limited thereby restricting statistical representation of sample's characteristics. In DAXM, the detector is placed such that its normal axis is perpendicular to the beam direction (see figure 2.11). This setup has proven to provide improved angular resolution. The spatial resolution in both techniques is required to be high to acquire grain maps. Moreover, DAXM uses the pencil beam cross-section, which is very small compared to the scanning area. This means that accurate strains and strain variation can be acquired within a grain.

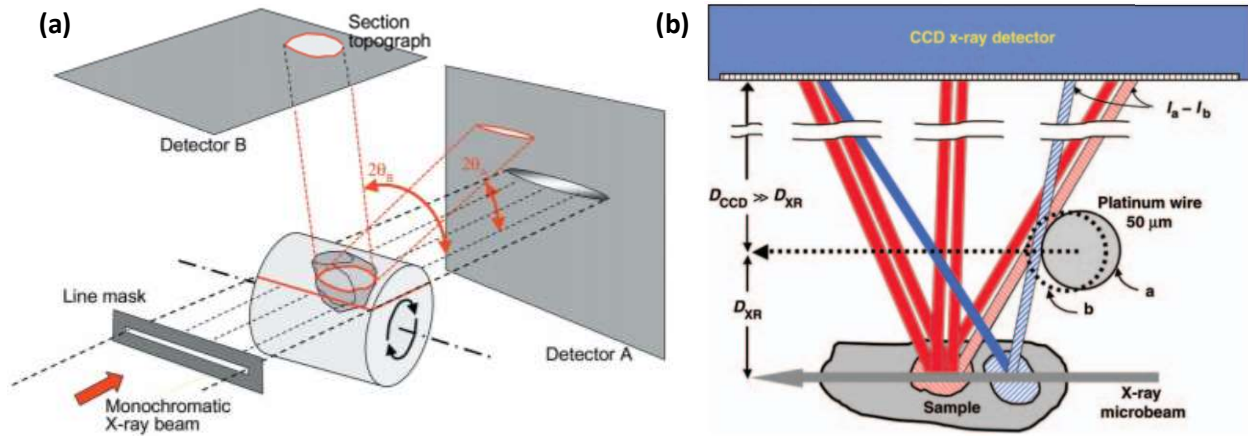


Figure 2.10: Schematics of (a) DCT and (b) DAXM

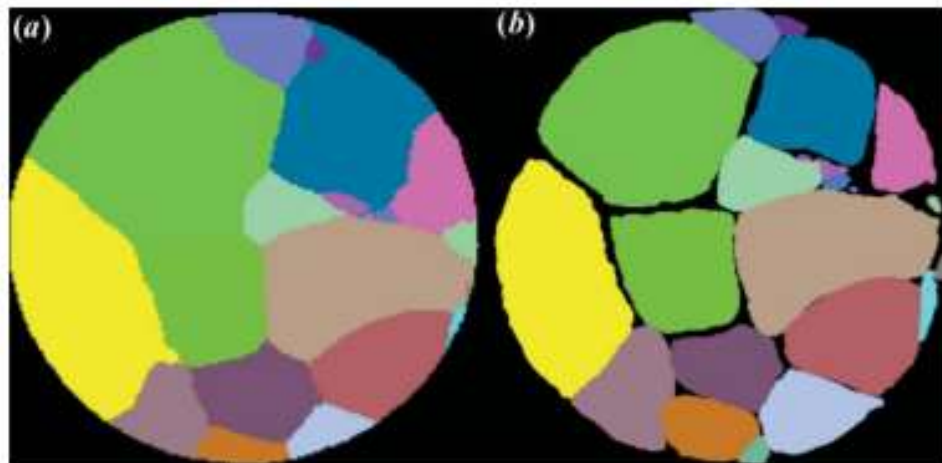


Figure 2.11: Detector A ( $2\theta \sim 0^\circ$ ) and (b) Detector B ( $2\theta \sim 90^\circ$ ) setups in DCT based on the schematic in figure 2.10 (a) [61]

Other techniques that use the same methodology as 3D-XRD are being investigated. 3D neutron diffraction is a potential technique that is yet to be developed and its benefit over 3D-XRD is its penetration depth. This means that the studied component does not have to go through sample preparation processes, like machining, to optimize them for the experiment.

## Chapter 3

### 3. Experimental Procedures and Data Processing

In this study, three-dimensional Synchrotron X-ray Diffraction (3D-XRD) is used to study deformation mechanism of HCP polycrystals. This is to provide robust data sets for numerical model development. The configuration C and line beam are used in the setup of 3D-XRD experiments to capture all the grains information in the scanned volume. More than 11000 zirconium grains and 8000 magnesium grains are measured. This is significant and is the first such measurement in the materials community. The experiment was done at the European Synchrotron Radiation Facility (ESRF), Grenoble, France, by Dr. Abdolvand and Dr. Mareau. Before conducting the experiment, the sample textures and dimensions were optimized for twinning and de-twinning during the first cyclic experiment that has yet been conducted on HCP alloys. In this chapter the procedure for sample preparation, data collection, and data analysis are explained in detail.

#### 3.1 Pre-experimental procedures

In many tensile test rigs, the loaded specimen has a dog-bone shape to ensure that deformation is localized in the middle of the specimen. However, in this experiment, compressive and tensile loads are applied on the sample to monitor twinning and de-twinning. The failure of dog-bone samples due to compressive loads can occur due to buckling or bending. Therefore, the specimen shape and deformation rig are optimized to prevent sample buckling and this was done using ABAQUS finite element solver. As shown in Fig. 3.1, four preliminary designs are initially introduced for finite element analysis (FEA) by Dr. Abdolvand and the sample with the best mechanical response was selected.

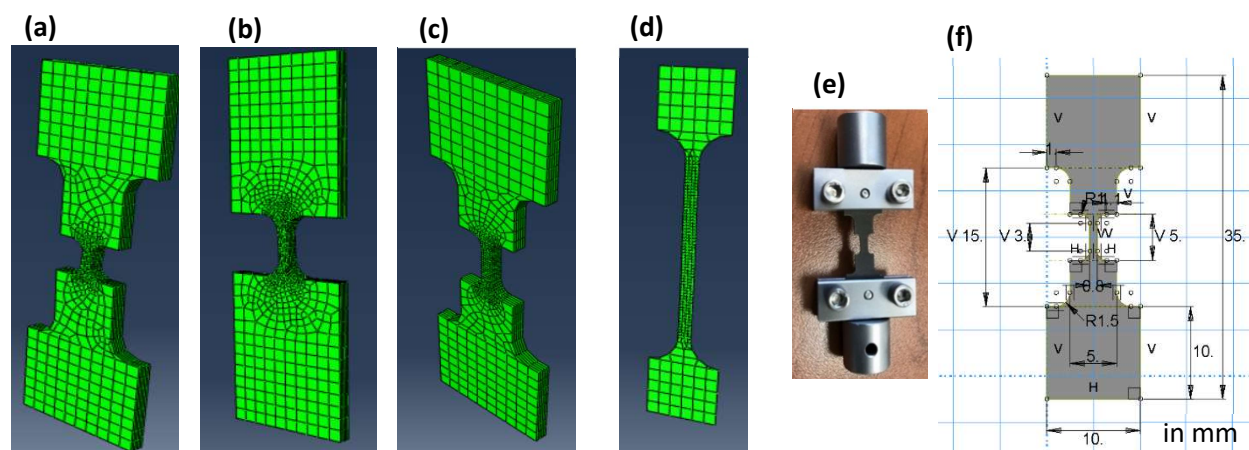


**Figure 3.1: (a) – (d) Preliminary designs for in-situ 3D-XRD experiment, (e) the modified deformation grip with the final sample design and (f) dimensions of the selected specimen**

Among the four specimen designs shown in figure 3.1 (a)-(d), the third design, figure 3.1 (c), was selected for the experimental study. In addition to these designs, the grips used for holding specimens were also designed to optimize the cycling of small samples during the in-situ experiment. This was necessary as the optimum thickness for zirconium sample was  $\sim 0.7$  mm and that for the magnesium sample was  $\sim 1.1$  mm. To ensure that the ends of the specimen, in the grips, do not slip during compressive loading, a hole was extruded through the grips and the specimen allowing for the specimen to hold on to the grips with the aid of screws and bolts. Since the hole is relatively small, the material selected and diameter of the screw are required to be carefully chosen. Likewise, finite element analysis on the screw was conducted to confirm that the screw can sustain the applied loads. Once the designs were finalized, a pure zirconium bar was firstly annealed and then machined to the geometry shown in figure 3.1. SEM image and EBSD maps are captured on the machined specimen to check for the texture, grain size and morphology to ensure they are perfect to the 3D-XRD experiment. Before heat treatment, the average grain size of the as-received zirconium bar was 12 microns (see figure 3.2 (c)). Since there are many grains in the as-received specimen, the characterization with 3D-XRD would be quite challenging due to overlapping of diffraction spots. To avoid this issue, heat treatment was conducted at  $700$  °C for 2 straight days in an argon gas environment to prevent formation of an oxide layer. The dog-bone samples were then machined out of the cleaned bar. The grain size approximately tripled to 41 microns and the morphology of the grains are equiaxed (as shown in figure 3.2 (d)).

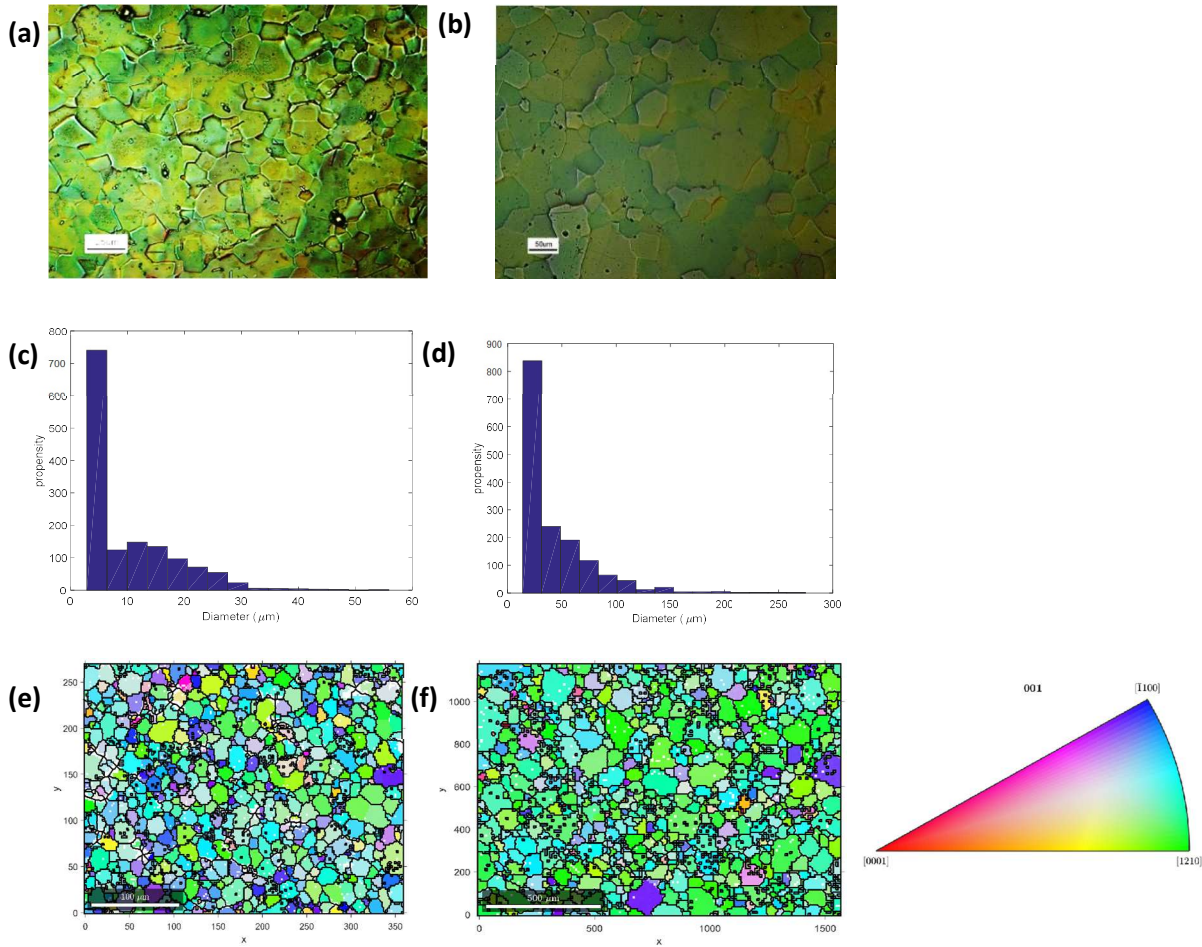


**Figure 3.2: (a,b) optical image, (c,d) grain sized distribution and (e,f) EBSD maps before and after heat treatment of zirconium. (a), (c), and (e) are from the “as-received”.**

To eliminate the effects of Electric discharge machining (EDM) of the samples, surface polishing was conducted. Samples were polished from 150 grid down to 2000 grid, and then with colloidal silica solution with powder sizes of 1, 0.5, and 0.3 microns. Finally, a solution of 10% perchloric acid and 90% methanol was used for electropolishing the samples. This was done at -35 °C to minimize surface damage. Upon completion of the process, the resulting surface was shiny and had no scratches. Among the 10 specimens, 5 of them were designed for in-situ experimentation and others were for ex-situ prior experimentation. EBSD scans were conducted on two of the in-situ and one ex-situ samples. The EBSD map of the in-situ specimen used in the 3D-XRD experiment is shown in figure 3.3 and the dimensions of the rectangular cross-section is 0.67mm and 0.78mm. The same procedure was followed for magnesium samples but the final sample cross section area is 0.93mm and 0.95mm.

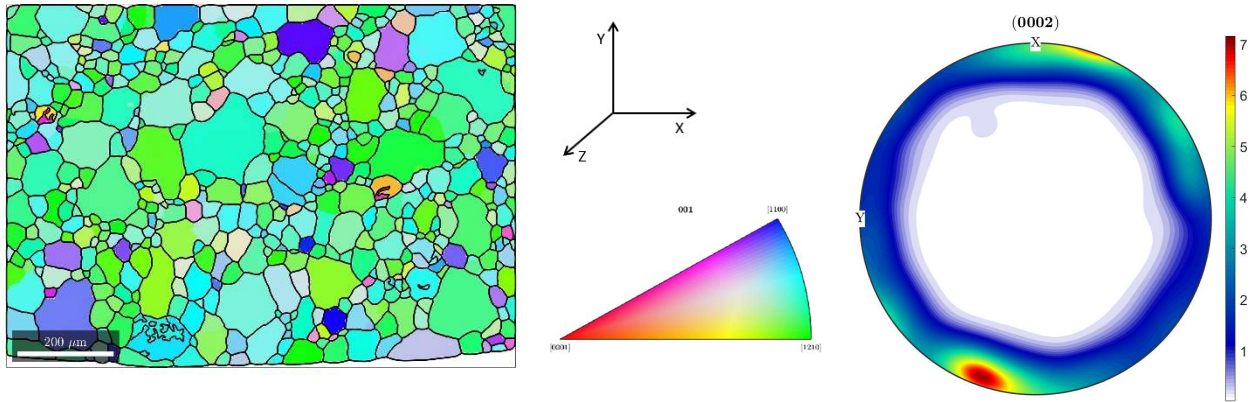


**Figure 3.3: Final EBSD map of zirconium sample after mechanical polishing and electropolishing**

From the map and the inverse pole figure, almost all the grains have their prism plane normal oriented in the z-axis, and from the pole figure, the basal plane normal or c-axes are distributed along the x- and y- axes. This illustrates that the zirconium specimen is quite textured for deformation twinning to occur when loaded along the x-direction in a tensile manner. Note that x-axis in the SEM/EBSD images is the z-axis in the 3D-XRD experiment, i.e. the loading direction.

The magnesium samples were cut from a rolled plate and then annealed to increase the average grain size. Samples were cut from the RD-TD plane. This is to activate twinning during the compression test as most of the crystal c-axis were oriented perpendicular to the loading direction. The measured texture of the magnesium samples is shown in figure 3.4.

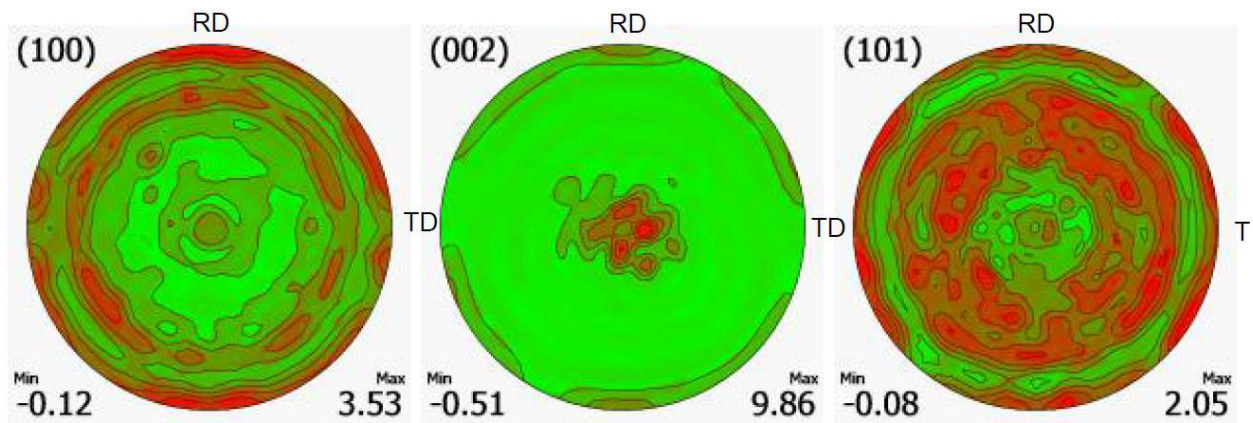


**Figure 3.4: Pole figures measured for Mg AZ31 prior to 3D-XRD experiment**

## 3.2 3D-XRD experiment and setup

The in-situ 3D-XRD experiment was conducted at a high-energy X-ray beamline ID-11 at the European Synchrotron Radiation Facility (ESRF) in Grenoble, France. The experimental set up is shown in figure 3.5. The laboratory coordinates of the sample are defined based on the positioning of the sample in the uniaxial tensile rig and axes were labelled as loading direction (LD), X-ray beam direction (BD), and transverse direction (TD). The final dimensions of the targeted scanning range are 1mm height, 0.78mm width, and 0.67mm thickness for zirconium sample and 1mm height, 0.95mm width and 0.93mm thickness for magnesium sample. The experiment is carried out by illuminating a planar beam of monochromatic X-rays.

For the first specimen (Zirconium), the beam energy was set at 78.395 keV, calibrated at platinum's K-edge, and its height was 40 microns in the z-direction, LD. This means that 25 scans for 25 layers are required to retrieve the microstructural data from the entire 1mm height of sample and the specimen is translated such that scanning starts from bottom to top. A beam stop was added behind the specimen to prohibit the transmitted beam from reaching the detector. Toward the end of the experiment, the height of the beam is reduced to 25 microns and the number of layers increased to 40 to cover the entire 1mm scanning range. The reason for this modification was to avoid overlapping of broadened diffraction spots coming from highly plastically deformed zirconium grains.

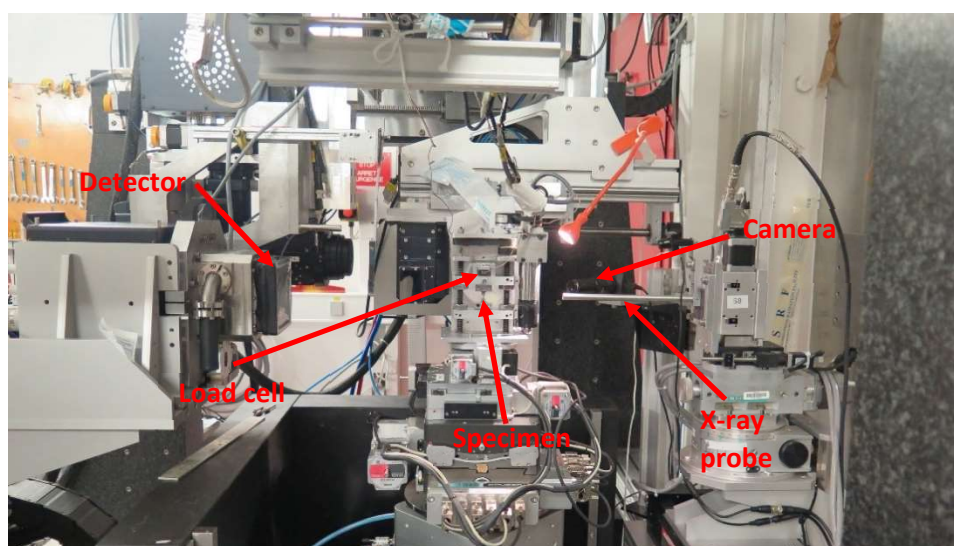


**Figure 3.5: The experimental setup at ID-11, ESRF**



The load cell on the tensile rig was used to measure the macroscopic applied stress while the macroscopic strain is measured by mounting two silver wires on the specimen on the plane perpendicular to x-axis, BD. The wires are placed at the maxima of the vertical scanning range and their displacements are tracked using X-ray beam to measure the macroscopic strain, which has an accuracy of  $3(10^{-5})$ . The applied strain was also measured using another independent method where a resistive strain gauge was attached to the sample, away from the scanning range, and strain was recorded with a separate strain indicator. During the in-situ experiment, the zirconium sample was rotated on an omega-stage around the loading direction (LD) and the diffraction patterns were collected in angular ranges of  $[-234.5^\circ$  to  $-125.5^\circ]$  and  $[-54.5^\circ$  to  $54.5^\circ]$  in steps of  $0.25^\circ$  to collect the diffraction spots of all grains. This experiment used a more efficient way of rotating the stage while capturing the images. In previous experiments, the stage was rotated by the step angle ( $0.25^\circ$ ) and then paused for capturing the images. In this experiment, the sample was constantly rotating at a low angular speed while diffraction patterns were captured at  $0.5^\circ$  step size. Once the  $\omega$ -range was completed, the  $\omega$ -rotation reversed and the diffraction patterns were captured again at  $0.5^\circ$  step size such that the two sub-steps do not overlap. The diffraction images were collected on a Frelon2K detector with  $2048 \times 2048$  pixels with each pixel size of  $50 \times 50 \mu\text{m}^2$ . The distance between the sample and the detector was fixed at approximately 325mm.

Likewise, the same experiment was conducted on the magnesium sample. The X-ray beam energy in this experiment was set to 51.996 keV, calibrated Terbium, Tb, K-edge. The dimensions of the sample are 1mm in the vertical direction, LD, 0.95mm width (TD), and 0.93mm thickness (BD). The initial beam height used for scanning is 100 microns. The beam height is relatively large when compared to the beam height used in zirconium due to the large grain size ( $\sim 60$  microns) in the magnesium specimen. After the first two in-situ loading steps, the beam size was halved to 50 microns to capture twins and minimize overlapping of peaks. The total number of layers required to accommodate the full height of the scanning range was initially 10 and then 20 when the beam size dropped. The sample to detector distance was 185 mm for this experiment.

The total number of diffraction images captured from both experiments are slightly close to 300,000 comprising of approximately 4TB size of data. Intensive post-processing was done by coding in Python and using various software by the author of this thesis to index grains.

### 3.3 Diffraction data processing

Post-processing of the diffraction data was handled by python programming in the FABLE suite of software [40]. This was done in two stages, identifying grains (grain indexing), and grain refinement.

#### 3.3.1 Indexing grains

In the first stage, ImageD11 [62] was used to index the grains and make grain maps. The grain map contains information about each grain such as position, orientation, elastic strain and stress tensors. For the code to work, the following list containing the preassigned experimental variables should be determined.

- X-ray beam wavelength
- Sample to detector distance
- Pixel size of the detector
- The center of the detector
- Detector tilts
- Sample rotation details (rotation step size ( $w$ ), rotation angular range, etc)

The first step for obtaining data is to remove the background of the collected diffraction images. Background image is created by firstly calculating the background of each diffraction image and then calculating the background average for all of the patterns measured for each load step. After reducing the calculated background from each diffraction image, the next step is peak-search. The peak-search algorithm searches for diffraction spots and adds up a connected region of pixels (i.e. one diffraction spot) that are above the minimum intensity, specified by the user, and subtracts the averaged background image intensity. A series of output files with a '.flt' and '.spt' extensions (containing peaks) will be spewed out based on the intensity thresholds provided by the user. All of the .flt output files are then merged into a single .flt file by avoiding spot overlaps. The geometry and experimental setup, e.g beam energy and detector distance, can then be used to index grains.

Scattering vectors are calculated to index peaks from the 'flt' file and assign them to grains based on their estimated COM positions and crystallographic orientations. This is an iterative process where simulated peaks for each orientation are compared with measured ones to index a grain until the minimum number of peaks per grain is achieved. Peaks that have less than 5 pixels are removed from analysis since to remove any potential left-over noise after background reduction. The peaks close to the detector edges are also eliminated since they do not form full ring. Additional parameters, such as cosine and d-spacing tolerances, are provided into the program for indexing peaks and grains. The cosine tolerance is the maximum peak width allowed for a diffraction spot. The d-spacing tolerance is simply the thickness of one ring in the diffraction pattern used for identifying the ring number for each diffraction spot. By reducing the 'hkl' tolerance, the indexing process selects the peaks using tighter tolerances, however the total number of indexed peaks is reduced. The 'hkl' tolerance is the difference between the retrieved 'hkl' from the peak search and the simulated 'hkl'. Once indexing is done, a 'ubi' file containing grain information is created. This file is then used to make grain map with reduced hkl tolerance to improve grain positions. This process is iterated until the grain's information are accurate for further processing (i.e. Stage II).

The experimental, i.e. global, parameters are also iterated and averaged using the indexed grain from the previous step. The change in the crystal parameters defines elastic strain. Therefore, the initial crystal parameters are used to obtain the final strain tensors. This is done for both specimens, zirconium and magnesium at the first step, i.e. pre-load, where the macroscopic applied stress and strain in the vertical direction, LD, are approximately zero. An iterative process is carried on the two mentioned parameters to modify them until the average microscopic stresses calculated for all measured grains in the vertical, LD, is close to zero.

### 3.3.2 Refining grains

In the second stage, FitAllB [63] was used to refine the grain center-of-mass (COM), orientations and elastic strain tensors from the .flt files and produce the final grain map. The term FitAllB is originated from program purpose of fitting all B tensors, grain specific reciprocal space metrics, containing information about strains of individual grains. If the elastic stiffness tensor is known, stresses can be calculated using the measured elastic strains. FitAllB also provides the errors associated with each grain information (i.e. COMs, orientations, stresses, and strains). In

addition, relative volume for each grain is also calculated through the intensity of the grain's diffracted peaks. This essentially means that a 3D grain map of stresses or orientations can be obtained through tessellation for equiaxed grains. Supplementary information, like X-ray absorption coefficients of specimen, can improve the prediction of the grain volumes. The crystal parameters that are used for zirconium specimen are  $a_1 = a_2 = 3.23 \text{ \AA}$  and  $c = 5.151 \text{ \AA}$  measured in Angstrom. Similarly, the initial crystal parameters used for magnesium specimen are  $a_1 = a_2 = 3.216 \text{ \AA}$  and  $c = 5.223 \text{ \AA}$ . Maximum g-vector misorientation, volume tolerance and minimum reflections per grain are provided in the input file to reject undesirable peaks and acquire the grain's information with high confidence.

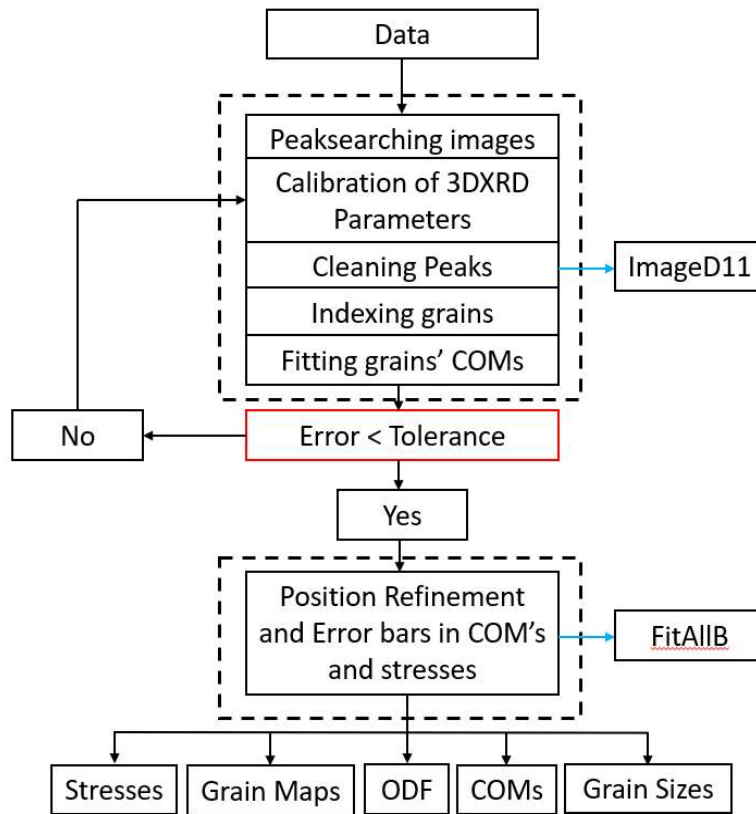


**Figure 3.6: Flowchart describing the procedure of postprocessing the diffraction images**

### 3.3.3 Mathematical Formulation

This section focuses on the mathematical formulations used in acquiring grain information from diffraction images [64]. The scattering vector,  $\vec{q}$  (shown in figure 3.7 (b)), bisects the incident beam ( $\vec{R}_0$ ), with the wavelength of  $\lambda$ , and the diffracted beam ( $\vec{R}_1$ ):

$$\vec{q} = \frac{\vec{R}_0 - \vec{R}_1}{\lambda} = \vec{r}_{hkl}^g \quad (3.1)$$

where  $\vec{r}_{hkl}^g$  is the reciprocal lattice vector normal to the hkl plane and superscript g represents the following vector in the global or laboratory coordinate system. The sample coordinate system is defined based on the rotation of the specimen on the  $\omega$ -stage.

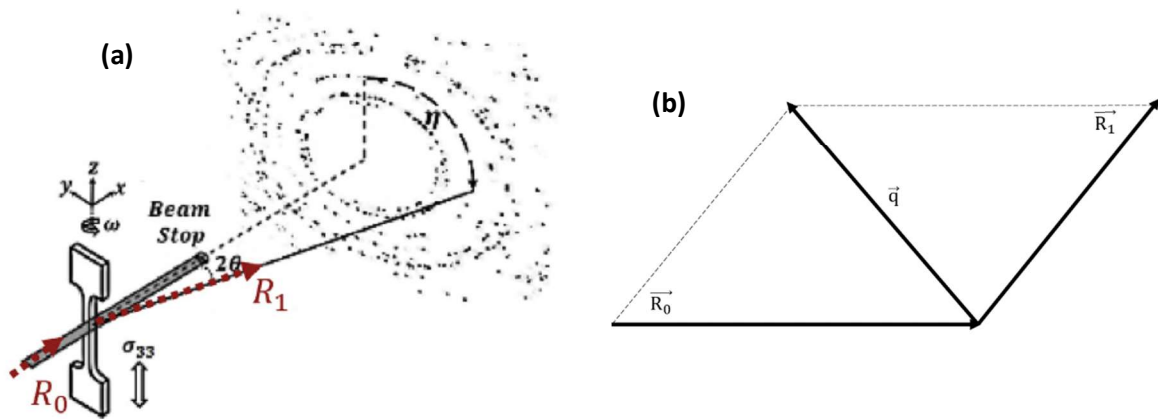


**Figure 3.7: (a) Schematic of 3D-XRD experimental setup, (b) Illustration of the scattering vector,  $\vec{q}$**

Three Cartesian coordinate systems are introduced in this experiment. One is lab or global coordinate system, i.e. stationary system, and is based on the beam direction (BD), loading direction (LD), and transverse direction (TD). The second coordinate system is attached to the sample and rotates with the sample with  $\omega$ -rotation about the loading direction. Through constant rotation of  $\omega$ -stage, global x- and y-coordinates of the sample changes (see figure 3.7 (a)). This simplifies the conversion of the crystal coordinates system to the sample coordinate system. The third coordinate system is the crystal (grain) coordinate system within the sample. The crystal coordinate system is the coordinate system for each grain, where c-axis is perpendicular to the other two axes lying on the basal plane. Thus, to convert any lattice vector in the crystal coordinate system,  $\vec{r}_{hkl}^c$ , to the sample coordinate system,  $\vec{r}_{hkl}^s$ , the following equation is used:

$$\vec{r}_{hkl}^s = R_C^S \vec{r}_{hkl}^c \quad (3.2)$$

where  $R_C^S$  is the rotation tensor containing the Euler angles that transforms the crystal coordinate system to the sample coordinate system. Since the sample coordinate system changes with the

angular rotation of the  $\omega$ -stage, the system can be presented in the global coordinate system through the following expression:

$$\vec{r}_{hkl}^g = R^\omega \vec{r}_{hkl}^s = \begin{bmatrix} \cos\omega & \sin\omega & 0 \\ -\sin\omega & \cos\omega & 0 \\ 0 & 0 & 1 \end{bmatrix} \vec{r}_{hkl}^s \quad (3.3)$$

The unit vector of the diffracted beam ( $\vec{R}_1$ ) intersect the detector at the  $2\theta$  and  $\eta$  angles as shown in figure 3.7(a):

$$\vec{R}_1 = \begin{bmatrix} \cos 2\theta \\ -\sin 2\theta \sin \eta \\ \sin 2\theta \cos \eta \end{bmatrix} \quad (3.4)$$

Through substitution of Eq. 3.4 in Eq. 3.1, and considering that the incident beam vector,  $\vec{R}_0$ , is  $[1, 0, 0]$ , the scattering vector is expressed as:

$$\vec{q} = \begin{bmatrix} -\sin\theta \\ -\cos\theta \sin\eta \\ \sin 2\theta \cos\eta \end{bmatrix} \quad (3.5)$$

$\eta$  is the angle between the vertical axis of the diffraction pattern and the line connecting the center point of the rings to the peak's center position (see figure 3.7(a)). Euler angles ( $\phi_1, \phi, \phi_2$ ) are used for calculating the transformation matrix that converts the crystal coordinates of a grain to the sample coordinates (Eq. 3.2). Using the Eqs. 3.3-3.5, the scattering vector in the sample coordinate system can be expressed as:

$$\begin{bmatrix} r_x^s \\ r_y^s \\ r_z^s \end{bmatrix} = \begin{bmatrix} \cos\omega & -\sin\omega & 0 \\ \sin\omega & \cos\omega & 0 \\ 0 & 0 & 1 \end{bmatrix} \begin{bmatrix} -\sin\theta \\ -\cos\theta \sin\eta \\ \sin 2\theta \cos\eta \end{bmatrix} \quad (3.6)$$

where  $r_x^s, r_y^s, r_z^s$  are the components of  $\vec{r}_{hkl}^s$ . The energy of the incident beam in zirconium and magnesium are 78.39 KeV and 51.996 KeV respectively therefore the angle,  $\theta$ , can be determined for each (hkl) plane using Bragg's law. Hence, the  $\omega$ -rotation satisfying the diffraction condition for a particular (hkl) plane can be calculated using the following equation:

$$r_x^s \cos\omega + r_y^s \sin\omega = -\sin\theta \quad (3.7)$$

The position of peaks on the detector can be determined by intersecting the diffracted beam vector at a specific  $\omega$ -rotation with the plane of detector. The peak position on the detector is hence expressed as:

$$P_y = \frac{R_{1y}}{R_{1x}} D - \frac{R_{1y}}{R_{1x}} \text{COM}_x^\omega + \text{COM}_y^\omega \quad (3.8)$$

$$P_z = \frac{R_{1z}}{R_{1x}} D - \frac{R_{1z}}{R_{1x}} \text{COM}_x^\omega + \text{COM}_z^\omega \quad (3.9)$$

where  $P_y$  and  $P_z$  are the peaks' positions in the horizontal and vertical direction respectively, and  $R_{1x}$ ,  $R_{1y}$ , and  $R_{1z}$  are the three components of the diffracted beam vector  $R_1$ , and  $D$  is the sample to detector distance.

### 3.3.4 Post-Analysis of grain maps

After indexing grains and performing grain refinement, the COM of each grain is acquired in the measured later. These layers are used to create the grain map for the entire scanned volume.

Since grain morphologies are not available from a 3D-XRD experiment, complexity arises when joining two layers. The main problem that should be tackled in this process is finding grains that exists in two or multiple layers. One way used in finding those grains is setting a misorientation limit (i.e. misorientation between c-axes of grains and total misorientation between grains) between the grains in their distinct layers and distance limit between their COMs.

#### 3.3.4.1 Misorientation limit

The misorientation limit between the c-axes of the separated grains and their total misorientation limit are kept equal. Since the zirconium specimen is textured and the magnesium sample is extremely textured, the appropriate limit is required to be chosen such that all the separated grains are picked up and pairing of grains with the “wrong” orientation is avoided. A study is conducted to investigate the number of paired grains (i.e. merging of sectioned grains) as a function of the misorientation limit. This investigation was conducted for the preload step.

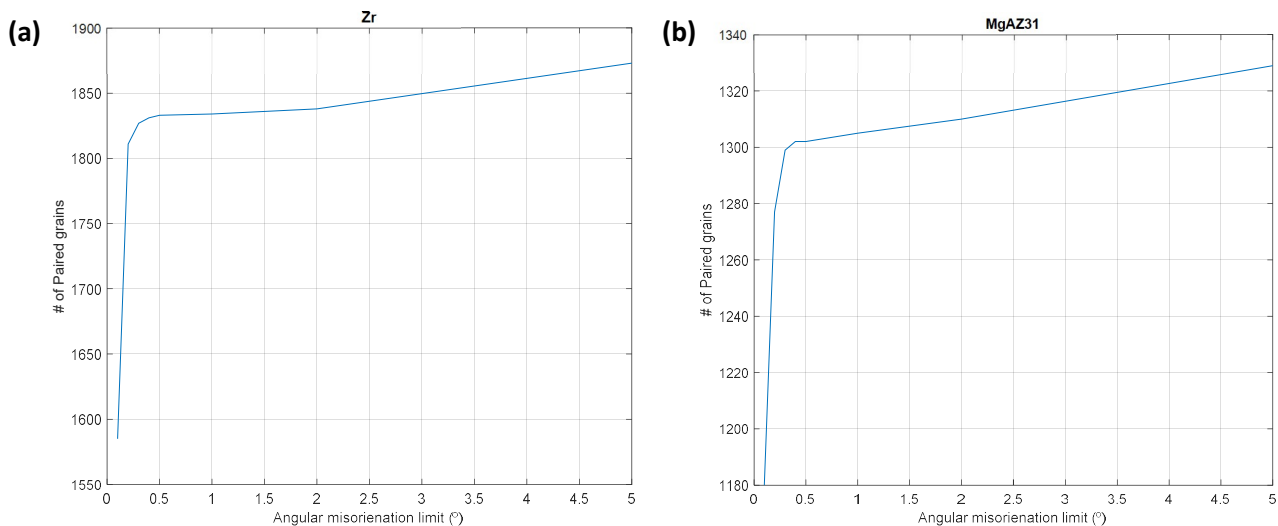


**Figure 3.8: Variation of number of paired grains with angular misorientation limit in pairing grains during grain map construction for (a) Zr and (b) MgAZ31**

For both zirconium and magnesium samples, the observed trends, in figure 3.8, are similar. The number of paired grains rises significantly, with a small change in the misorientation limit, and then converges at a specific number of paired grains followed by a linear positive slope. In the initial rise, the separated grains are picked up since their misorientation is quite low. The convergence indicates that most of those separated grains have been picked up and then the linear slope portrays grains that have been paired up with the “wrong” grain due to their similar orientation. Hence, the appropriate limit that can be used for both specimens is the point of convergence, which is  $2^\circ$  for zirconium and  $0.5^\circ$  for magnesium. However, due to orientation distribution within grain with plastic deformation, with increasing the applied strain, an additional  $0.5^\circ$  is added to the stated limits leaving the final limits as  $2.5^\circ$  and  $1^\circ$  for zirconium and magnesium respectively. The limit for magnesium is clearly lower than zirconium’s because of its higher texture.

### 3.3.4.2 Distance Limit

The second criterion used, limits the distance between the two separated grains. For this experiment, since the size of the grain is small compared to detector pixel size, the grain’s morphology cannot be acquired. However, the volume of the grain can be obtained from the intensity of the diffracted peaks and this feature can be used for this criterion. Several methods are used to identify the separated grains based on the distance criterion (see Fig. 3.9).



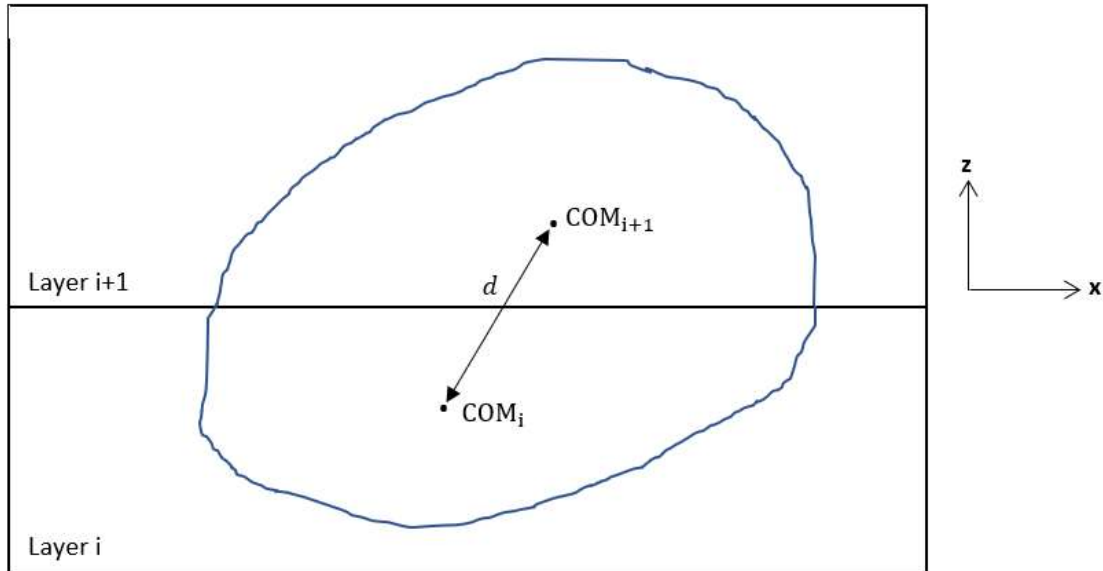


**Figure 3.9: Schematic of a single grain in two separate layers**

The first method imposes a fixed distance limit,  $d$ , between the COMs of the separated grains. Through this criterion, all separated grains with their COMs less than the fixed distance are captured and paired. The trend, shown in figure 3.10, is the same for both specimens, where the number of paired grains converges at a specific point and then slowly increases again. Large separated grains could fall in the large distance-limit hence paired large grains might not be accurate through this method.

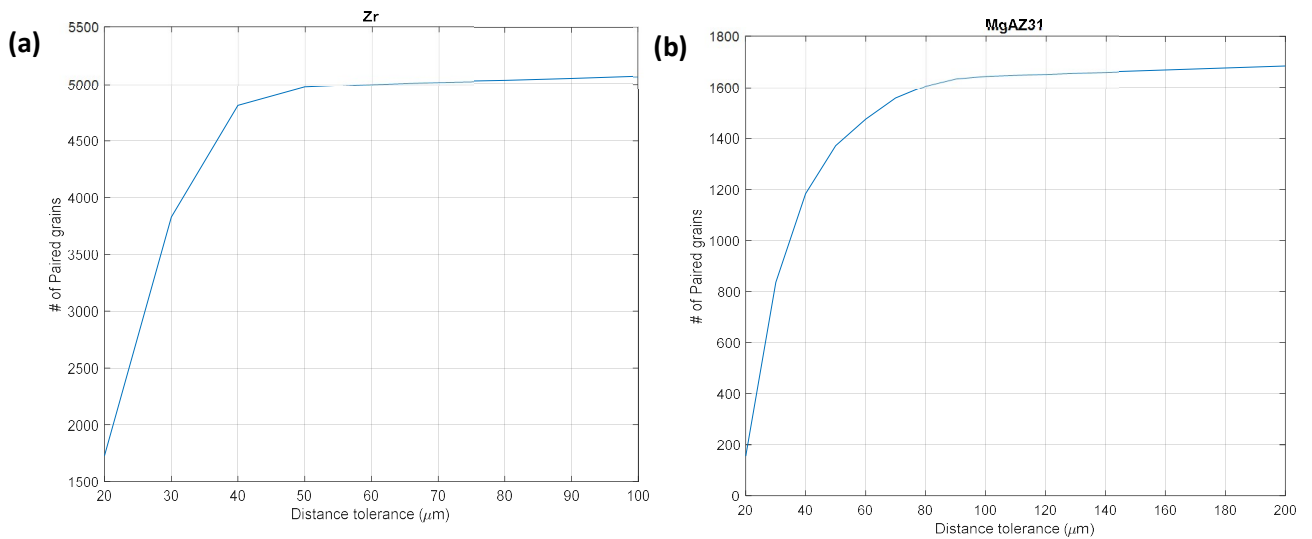


**Figure 3.10: Variation of the number of paired grains with the distance limit (between COMs of paired grains) for (a) Zr and (b) MgAZ31**

Another distance criterion method is the addition of the radii of both grains. The grain morphologies are not known however the calculated volumes can be used for assuming that the grain shape is sphere. For the grains to be paired up, ideally the summation of the radii of both grains should be equal to the distance between their COMs. Since the grains are not exactly sphere and the calculated volumes have their own error bars associated to them, a tolerance value is added to the radii summation.

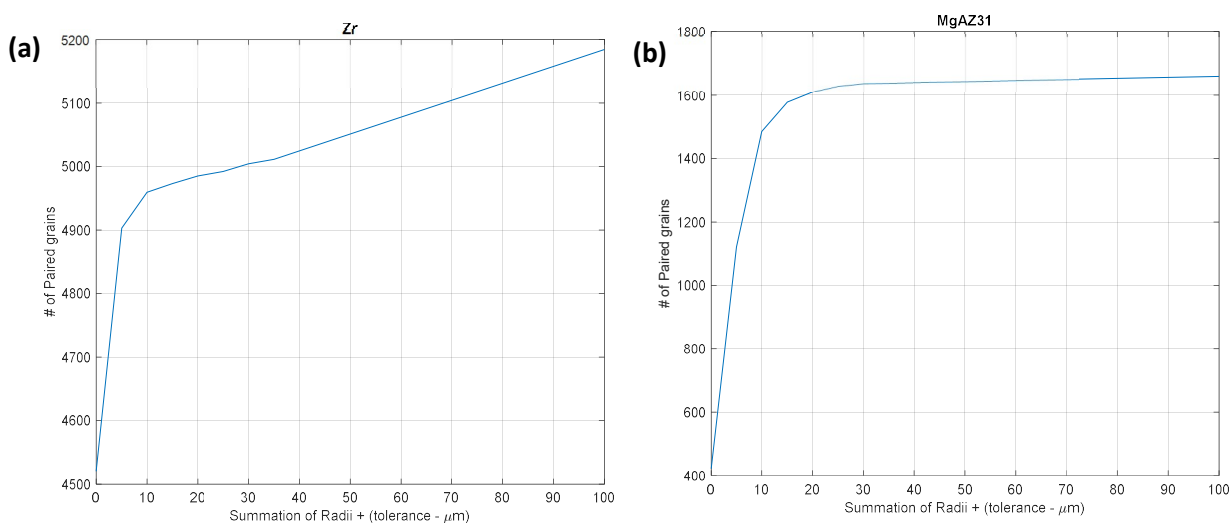


**Figure 3.11: Variation of the number of paired grains with the added tolerance to summation of the radii of the paired grains for (a) Zr and (b) Mg AZ31B**

The graphs in figure 3.11 shows the variation of the number of paired grains with the added tolerance, to the summation of the radii of the separated grains. The observed trend in both specimens is inconsistent for large tolerances illustrating that the captured large grains might not be the correct grains. This method could be ideal for equiaxed grains due to the assumption of spherical shaped grains however in the presence of nucleated or propagated twins, glitches could occur due to the significant difference between the assumed shape, sphere, and the actual shape, needle.

The final method is having a separate tolerance for each COM coordinate of the separated grains. Since EBSD measurements were conducted prior to 3D-XRD experiment, measured grain sizes were used to validate our merging approach. The main measured EBSD was firstly sectioned using the thickness of 40 microns, as shown in figure 3.12, to be consistent with the X-ray beam

size used in the 3D-XRD experiment. In the sectioned EBSD map of zirconium in figure 3.12, the COM of most of the separated grains are barely changing in the y-axis compared to the other two axes.

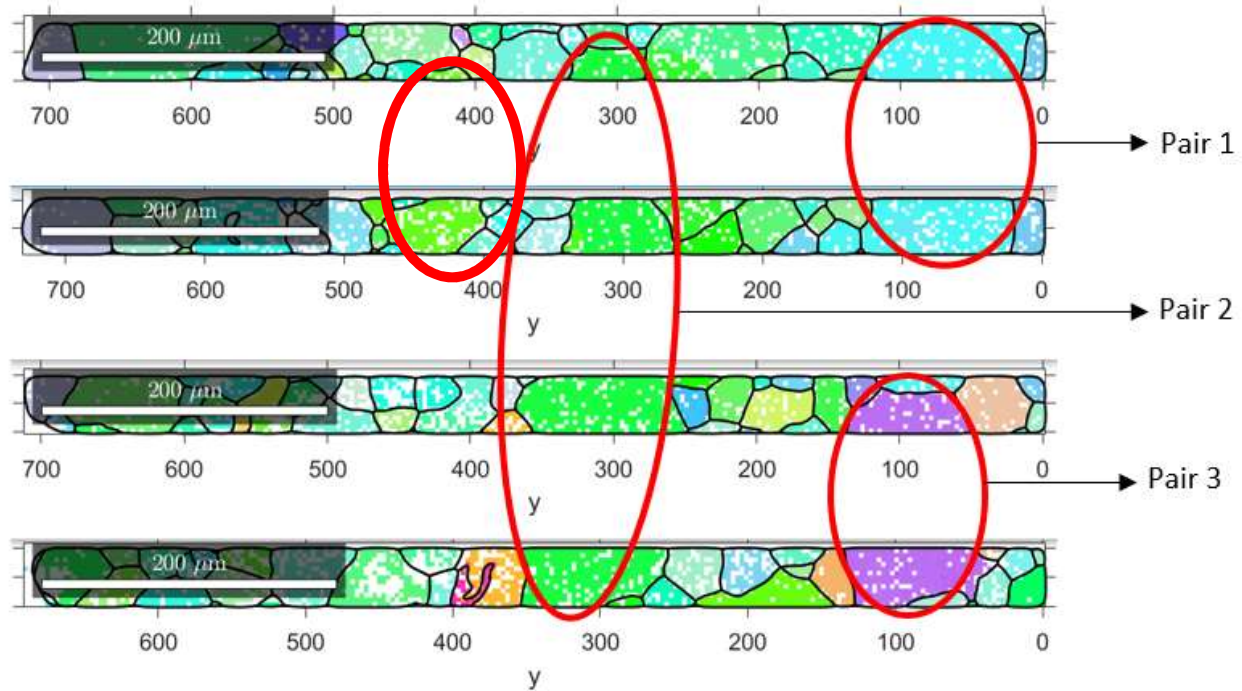


**Figure 3.12: EBSD map sectioned into layers to illustrate the divided grains in Pairs 1, 2, 3**

If a spherical grain is separated by a plane normal to the z-axis, the COMs of the separated grains in the z-direction will be significantly shifted from the original position but remain the same in the other two direction. Likewise, the same concept can be applied when this spherical grain is separated by any other plane. In figure 3.13, the separated grains in layer 11 and layer 12 of the first step of the zirconium specimen are shown. From the same figure, the COM coordinates in the x-axis and y-axis are similar in both layers but different in the z-axis due to the shift in the z-direction during scanning.

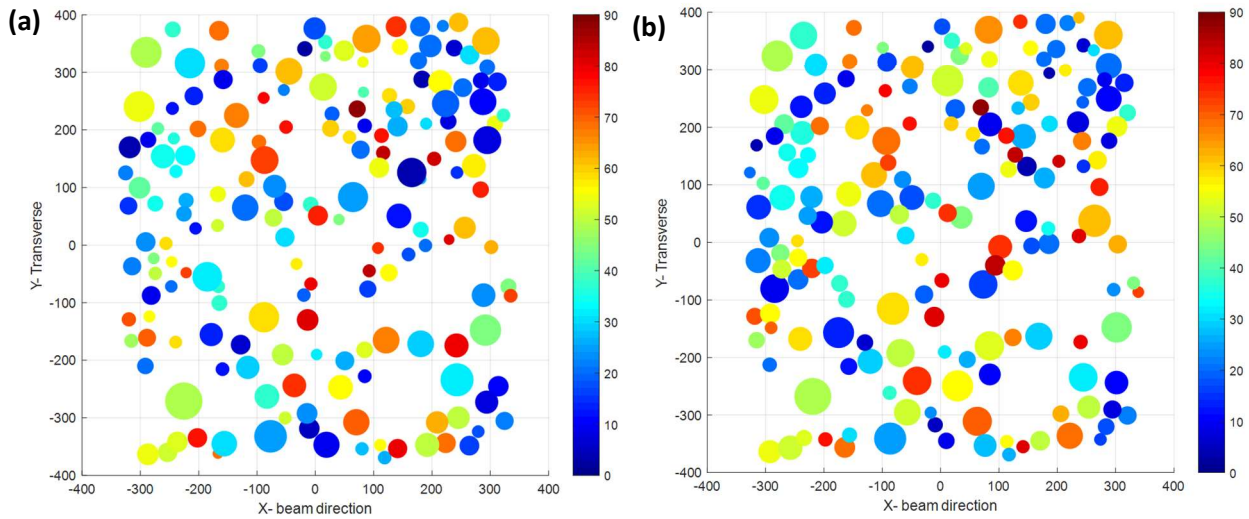


**Figure 3.13: X-Y Plane of the paired grains in Layers (a) 11 and (b) 12 in the 1st step of Zr. The figure demonstrates that all the grains have the same x- and y-coordinates**

To summarize the above methods, the misorientation criterion can be explicitly chosen based on the studies carried on both specimens. However, the distance criterion for all three mentioned procedures do not possess a clear value. Unlike the second method, the first and third method can estimate an approximate value for the distance criterion. One main challenge in this criterion is pairing up large separated grains due to the large distance between the COMs of their separated grains. The first and third method provide the same number of paired grains for similar limits, and hence were used in this study.

## Chapter 4

### 4. Analysis of 3D-XRD experiment on zirconium

This chapter focuses on providing a statistical analysis of the results acquired through the 3D-XRD experiment on zirconium. These results are then verified with the orientation maps acquired from EBSD analysis by comparing the texture and grain sizes. Next, further data analysis are conducted to investigate evolution of stresses in individual grains through the entire experiment. An algorithm that detects twins is also developed and the results including variant selection and Schmid factor of twins are discussed. The development of stresses and volumes of the parent grain is studied pre and post twinning.

In all of the figures presented in Chapters 4 and 5, the global Cartesian system is labeled as 11, 22, and 33 representing Beam Direction, Transverse Direction, and Loading Direction respectively.

#### 4.1 Details of 3D-XRD Results

The conducted synchrotron 3D-XRD experiment was carried out through nine loading steps, as shown in figure 4.1, to track grain stresses in the elastic and plastic zones. Over 11,000 grains are captured in the first step with all six components of their stress tensors. The grain average stresses and error bars are recorded in table 4.1. The applied strain provided in table 4.1 is measured by the strain gauge attached to the sample. The macroscopic stress is measured using the applied load from load cell and the sample cross-section. The total number of indexed grains acquired through data processing is recorded for each step so as the average number of peaks assigned to each grain. Micromechanical properties, including grains COMs and stresses are acquired through data processing and their averages is recorded in the table of results.

Errors are the highest in the BD while in the other two directions they are approximately the same. The reason is that the scattering vector,  $\vec{q}$ , is oriented toward the LD and TD due and this means that there is no component BD leading to high uncertainties. The error bar becomes large due to limited data in the BD. Moreover, error bars increase through the experiment due to peak broadening resulting from plastic deformation and the reduction in the total number of peaks assigned to a grain.

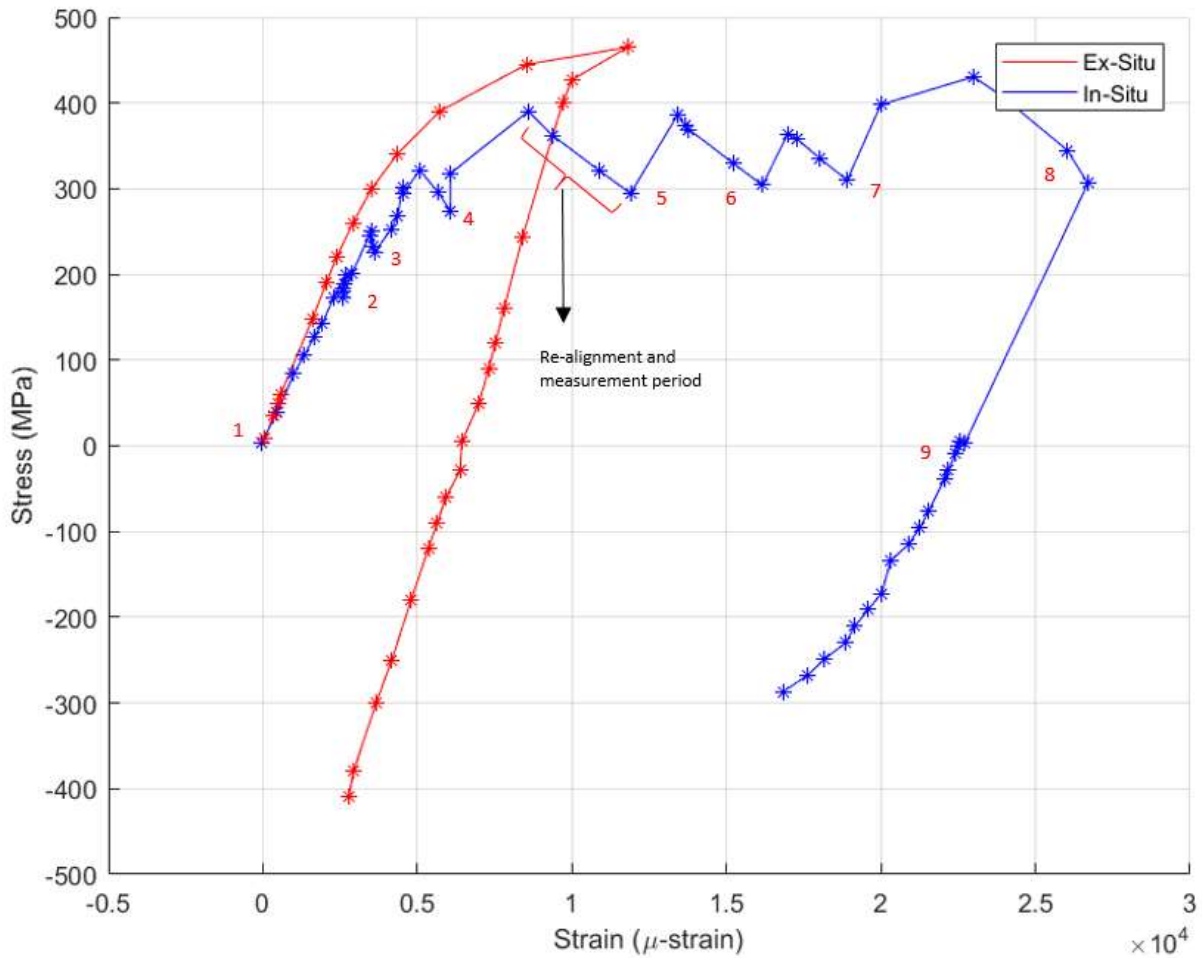


**Figure 4.1: Stress-strain plot of in-situ 3D-XRD measurement of zirconium**

Similarly, the number of indexed grains reduces with the experiment due to the reduction of the total number of peaks. Ideally, the number of indexed grains should increase due to twin nucleation, however, a lot of peaks that broaden, shown in the transition between figure 4.2 (a) and (b), due to plasticity and exceed the tolerances set in the indexing algorithm. These peaks are rejected during peak analysis leading to an overall drop in the number of peaks in plastic zone. On the hand, the number of grains should remain the same, after unloading the specimen, however the number of indexed grains is observed to increase. This increase originates from the increase in the number of indexed peaks since the broadened peaks becomes round again after unloading allowing it to get picked up by the peak searching algorithm.

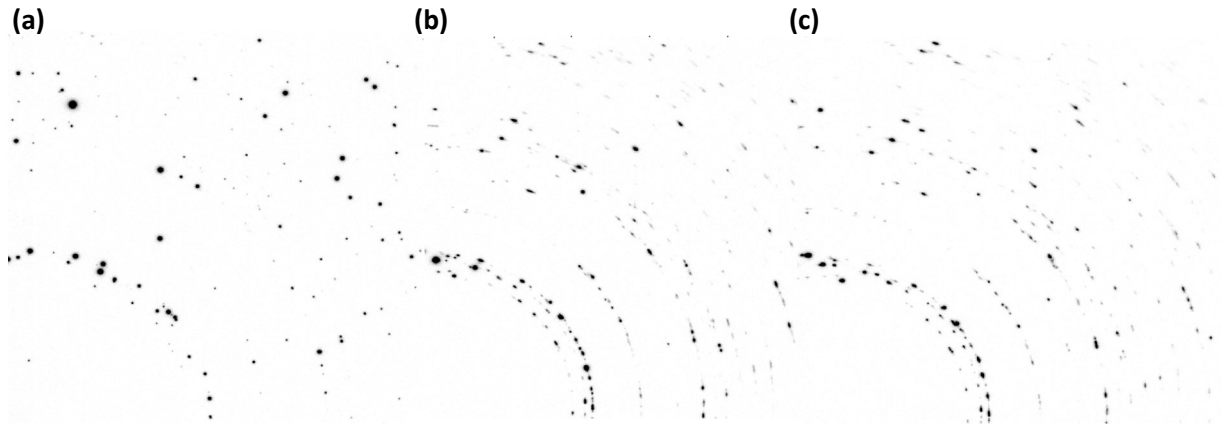


**Figure 4.2: Diffraction patterns of (a) Step-1 (Preload), (b) Step-8 (Applied Load = 220N), (c) Step-9 (Unload)**

The weighted average of grain stresses in the LD is matching with the microscopic applied stress and those in the other two directions are close to zero showing that the selection of crystal parameters in the pre-load step is done accurately. The three macroscopic stresses provided are before alignment, after alignment and after measurement. Once the sample is loaded to a specific load, the specimen is aligned to probe the same volume that was initially scanned. The alignment takes about half an hour. Once the specimen is realigned, the collection of diffraction patterns started and it took about 3 hours to fully scan the volume. During realignment and measurement, the stresses in the specimen relaxes, which causes uncertainties in the average micromechanical stresses. In one part of the sample, the stresses could be higher than another part since the measurement was taken earlier. The stress drop occurs exponentially where the majority of stress relaxation occurs during sample alignment. Therefore, the average microscopic stress should be compared with the macroscopic stress during the diffraction measurement period.

Table 4.1: 3D-XRD Table of Results for Zirconium

Step ID	Step Description	Applied Strain (%)	Macroscopic Stress (MPa)			No. of grains	Average Number of Peaks per grain	COM Position Error (Microns)	S11 (MPa)	S22 (MPa)	S33 (MPa)	S23 (MPa)	S13 (MPa)	S12 (MPa)	Beam Size
			Before Alignment	After Alignment	After Measurement										
1	Zr1_preload	0.0014	8	8	8	11703	119	±4.0530	-4.0535	0.3437	1.6343	-0.0777	0.3102	-0.9676	
2	Zr1_100N_	0.2574	184	180	172	11308	118	±3.8262	-6.2953	-6.2488	169.3536	0.2066	1.4295	-1.3658	
3	Zr1_130N_	0.3553	245	233	226	11087	117	±3.6559	±16.8042	±12.6232	±10.8316	±3.0911	±3.2722	±4.1490	
4	Zr1_170N_	0.5652	321	297	274	10995	115	±3.5272	-4.4025	2.5715	227.0768	0.6935	1.4609	-1.4024	
5	Zr1_200N_	1.0872	362	321	295	10578	109	±4.7477	±15.8967	±11.9988	±10.3055	±2.9314	±3.1145	±3.9315	
6	Zr1_200Nb	1.5235	369	329	304	9071	105	±5.9196	-2.8437	1.5883	287.1286	0.9231	1.3057	-1.6438	0.04mm - height
7	Zr1_190N_	1.8900	358	335	310	8042	102	±6.5339	±15.5245	±11.6627	±10.0133	±2.8367	±3.0380	±3.8664	
8	Zr1_220N_	2.6000	406	344	306	7312	97	±9.5163	-2.1492	-1.8300	301.2988	1.0633	0.5855	-1.4867	
9	Zr1_15N_	2.2710	2	2	3	8455	102	±9.3115	±21.0113	±15.6791	±13.5493	±3.8737	±4.1176	±5.2489	
									±26.6246	±19.6260	±17.0425	±4.8716	±5.2165	±6.6337	
									±29.5474	±21.7689	±18.8945	±5.4215	±5.7936	±7.4578	
									±20.2937	±3.1330	±26.9703	±2.3971	±0.3362	±1.3734	
									±43.9218	±32.2290	±28.0148	±7.9680	±8.5870	±10.9902	0.025mm - height
									±17.7820	±32.2359	±3.9069	±0.7507	±0.1751	±2.6700	
									±42.9182	±31.4232	±27.2738	±7.5599	±8.3674	±10.6829	



## 4.2 Comparison between EBSD and 3D-XRD

The EBSD map was measured before conducting the 3D-XRD experiment. The post-processed data from the first step of 3D-XRD, the pre-load step, is compared to the EBSD measurement. One of the benefits of EBSD over 3D-XRD is its ability to capture grain's morphology due to its high spatial resolution. This feature is important in understanding the evolution of twins shape during deformation.

The EBSD data captures the grains on the surface of the specimen while the 3D-XRD data captures the entire 3D scanned volume. Therefore, only the results from sample surface measured by 3D-XRD is compared to those from EBSD. This is done by partitioning the top 60 microns, in BD, of the reconstructed grain volume. Texture and grain sizes are compared.

### 4.2.1 Texture

Since the same specimen was used in both techniques, the Euler angles should ideally represent the same texture. One way to view the overall texture and compare the results is to compare the misorientation of the basal plane normals and the prism plane normals with the lab (global) coordinate. Figures 4.3 (a)-(d) shows the distribution of the misorientations between basal and prism plane normals with the BD and LD from both techniques. From figures 4.3(a) and 4.3(c), the trend clearly demonstrates that there are almost no grains with their c-axes oriented along BD. This good agreement, observed in figures 4.3 (a)-(d), illustrates that the 3D-XRD results for texture measurement are accurate.

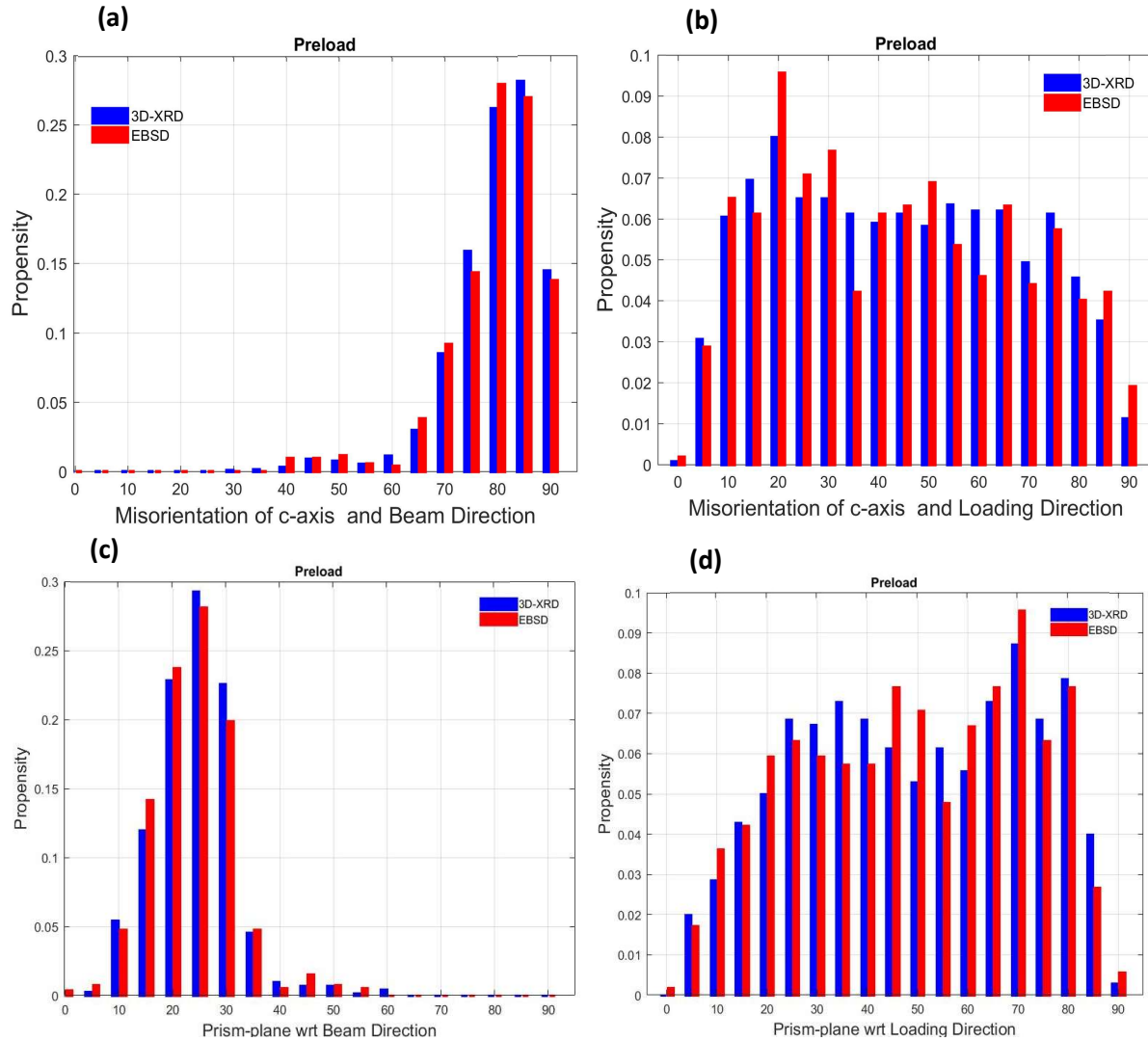


**Figure 4.3: Texture comparison between EBSD & 3D-XRD, misorientation of (a) c-axis with BD, (b) c-axis with LD, (c) prism plane normal with BD and (d) prism plane normal with LD**

## 4.2.2 Grain Sizes

Grain's volume acquired through 3D-XRD is computed using the intensity of the diffracted beam. The actual volume of a grain is calculated using the following expression:

$$V_g^i = \frac{V_{Rg}^i}{\sum_{i=1}^n V_{Rg}^i} V_P \quad (4.1)$$

$V_{Rg}^i$  is the relative volume of the grain measured in 3D-XRD experiment,  $n$  is the total number of measured grains, and  $V_P$  is the physical volume of the scanned specimen. Using the physical volume, and assuming that grains are spherical, grain diameters are calculated to compare with

those from EBSD. Since grains are equiaxed it was assumed that grains are spherically shaped. Similarly, the grain areas, in EBSD, are directly computed from the map since their shapes are known and their diameters are calculated by assuming that grains are circular. From figure 4.4, a good agreement is observed for the grain size distribution from both techniques. A bimodal distribution is observed in the trends where the first peaks is at 20 microns and the second, yet weaker peak is at 120 microns showing that the specimen had lots of small grains with some bigger grains. The trends are well matched in both techniques confirming the validity of the measured 3D-XRD data.

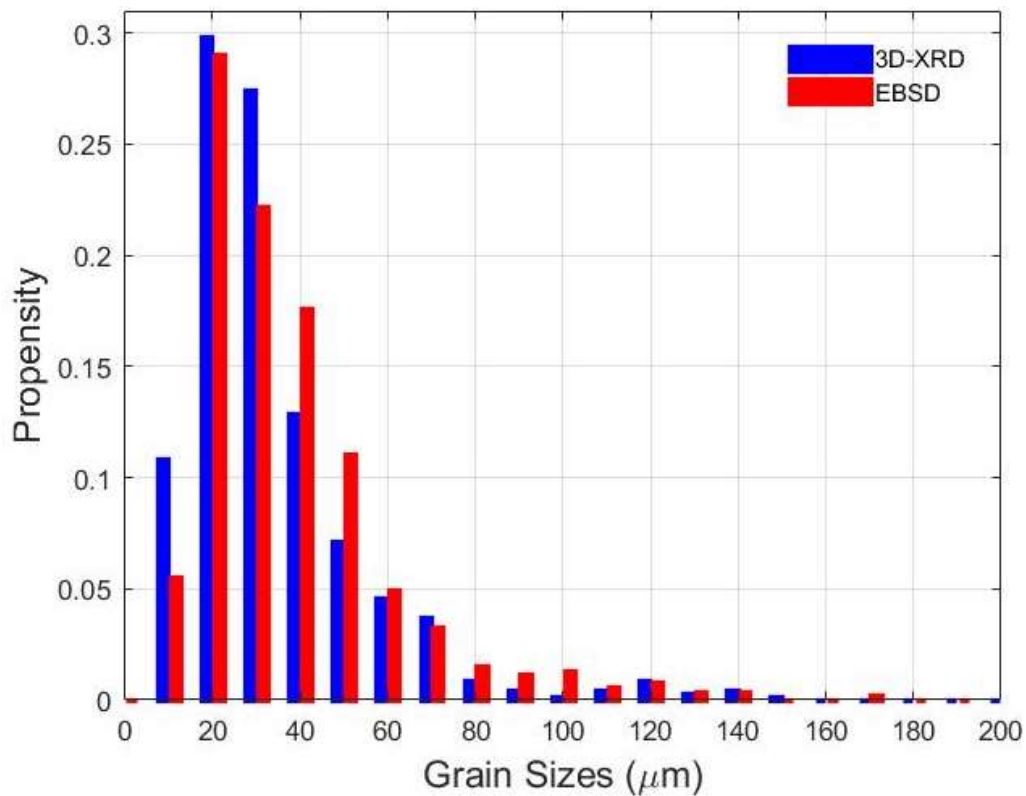


**Figure 4.4: Grain size comparison between EBSD & 3D-XRD**

### 4.3 Post Analysis

Diffraction measurement of each loading step during 3D-XRD experiment is independent from other steps. This simply means that the ID of a grain in one step is not the same in the consecutive step. Therefore, the MATLAB script developed by Abdolvand et al [65] was used and updated to match the grain IDs between any two steps. The neighbors of one grain is recorded from one step and the same grain is searched in the next step and once found, the recorded neighbors are matched with the neighbors of the matched grain. The aim of this process

is to track stresses of a single grain through the entire experiment. To have a unique grain ID assigned to each grain from each step, grains positions and orientations are independently compared. Each grain from the new step is compared with all the grains in the previous step. If the total misorientation as well as basal plane misorientation between the two grains in the different steps are less than  $2.5^\circ$  for Zr. and  $1.5^\circ$  for MgAZ31 and the distance between their COMs is less than 55 microns for Zr and 60 microns for MgAZ31 then the ID of the grain is matched. The rigid body movement between each step is fixed however the distance tolerance is still high to account for grains with high plastic deformations and the misorientation tolerances are similar to those used in joining layers in a single step. The neighborhood of the same grain ID should also satisfy the same criteria for the grains to be matched. The neighborhood procedure is added to avoid cases where more than one ID is matched. If the neighborhood is not matched or if the grain still has more than one match then they are considered unmatched.

A reconstructed volume of grains that are matched in steps 2 & 8 is displayed in figure 4.5 (c) and compared with all the grains in step 8, displayed in figure 4.5 (d). The color bar represents the c-axis misorientation with BD (x-axis). The results of these matches can be used to generate a matrix of grain IDs in all 9 steps and two methods are proposed to generate this matrix. The first method records grains from two consecutive steps, i.e. grains matched between steps 1&2 should also be matched between steps 2&3 all the way to steps 8&9. In the second method, grains are recorded from three consecutive steps, i.e. grains matched in steps 1,2&3 should be matched with steps 2,3&4 all the way to steps 7,8&9. The second method is more conservative since the procedure looks at grains matched in at least three consecutive steps, rather than two, therefore the number of matched grains is expected to be lower than the first method. Another matrix is also created that shows all the grains, even the unmatched ones, in all steps.

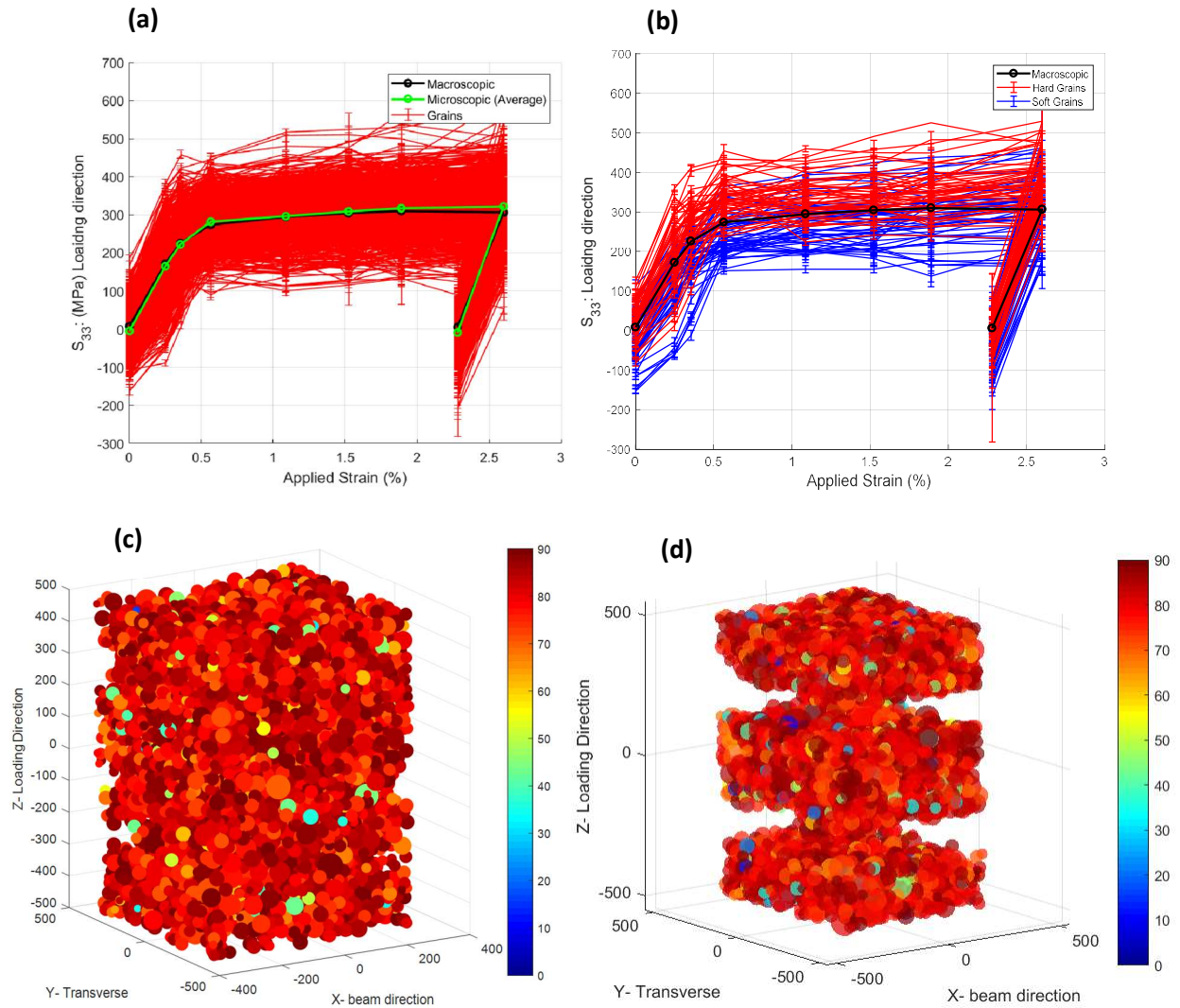


**Figure 4.5: (a) Macroscopic stress-strain plot and stress-strain plots of all grains that are matched in all steps, (b) Macroscopic stress-strain plot and stress-strain plot of hard and soft grains, c-axis misorientation with BD (c) of matched grains between step 2 and 8 plotted in step 2 and (d) sliced grain map in step 8**

The total number of grains matched in all steps is 4335 from the first method and 2557 from the second method. The number of matched grains in the second method is less than the first method since (a) it is more conservative method and (b) rigid body movement between step ‘n’ and step ‘n+2’ might be more than the tolerances used for all grains in our grain matching analysis. Using the ID of the matched grain, based on the 1<sup>st</sup> method, grain stresses along the LD ( $S_{33}$ ) are plotted as a function of applied stresses (figure 4.5 (a)). In addition, hard grains and soft grains are selected for further analysis. Grains with their c-axis misorientation with LD less than  $10^\circ$  are hard grains and those with the misorientation higher than  $80^\circ$  are soft grains. Grains with

hard orientations are those that typically deform plastically by twinning or dislocation movement on the pyramidal  $\langle c+a \rangle$  systems. On the other hand, soft grains are those that deform plastically by slip on the basal or prism slip systems with low CRSS values.

**Table 4.2: CRSS of slip systems of Zircaloy-2 ( $\alpha$ -Zr) [40] and single crystal pure Zr of size 10  $\mu\text{m}$  [66]**

Plane	Zircaloy-2, $\alpha$ -Zr, CRSS (GPa)	Pure-Zr CRSS (GPa)
Prism	0.111	0.182
Basal	0.156	0.322
Pyramidal	0.307	0.501
Tensile Twinning	0.232	-

The stress-strain graph in figure 4.5 (a) shows the stresses in all matched grains in red and the black line is the applied stress measured by the load cell. The green plot represents the weighted average of the stresses measured for all grains in the probed volume. This trend matches applied stress, i.e. macroscopic stress verifying our multi-scale approach. In figure 4.5 (b), stress-strain plots of hard and soft orientation grains are plotted and the graphs clearly displays that the stresses in most of the hard grains are larger than soft grains. In order for the hard grain to attain plasticity, a higher stress is required to exceed to the higher CRSS value. For the same strain, the stresses in hard grains are larger than soft grains as shown in the plot. After unloading the sample, the resulting residual stresses in hard grains are tensile stresses while soft grains have compressive stresses to fulfill the stress balance. From the two grain maps in figures 4.5 (c) and 4.5 (d), most of the grains in step 2 can be observed in step 8 and the new blue colored grains are the twins that are nucleated and propagated during the in-situ deformation. Steps 2 and 8 are chosen as an example of the most difficult scenario, since they are the furthest steps with the highest rigid body movement and highest difference in plastic deformation thereby highlighting the effectiveness of the matching algorithm.

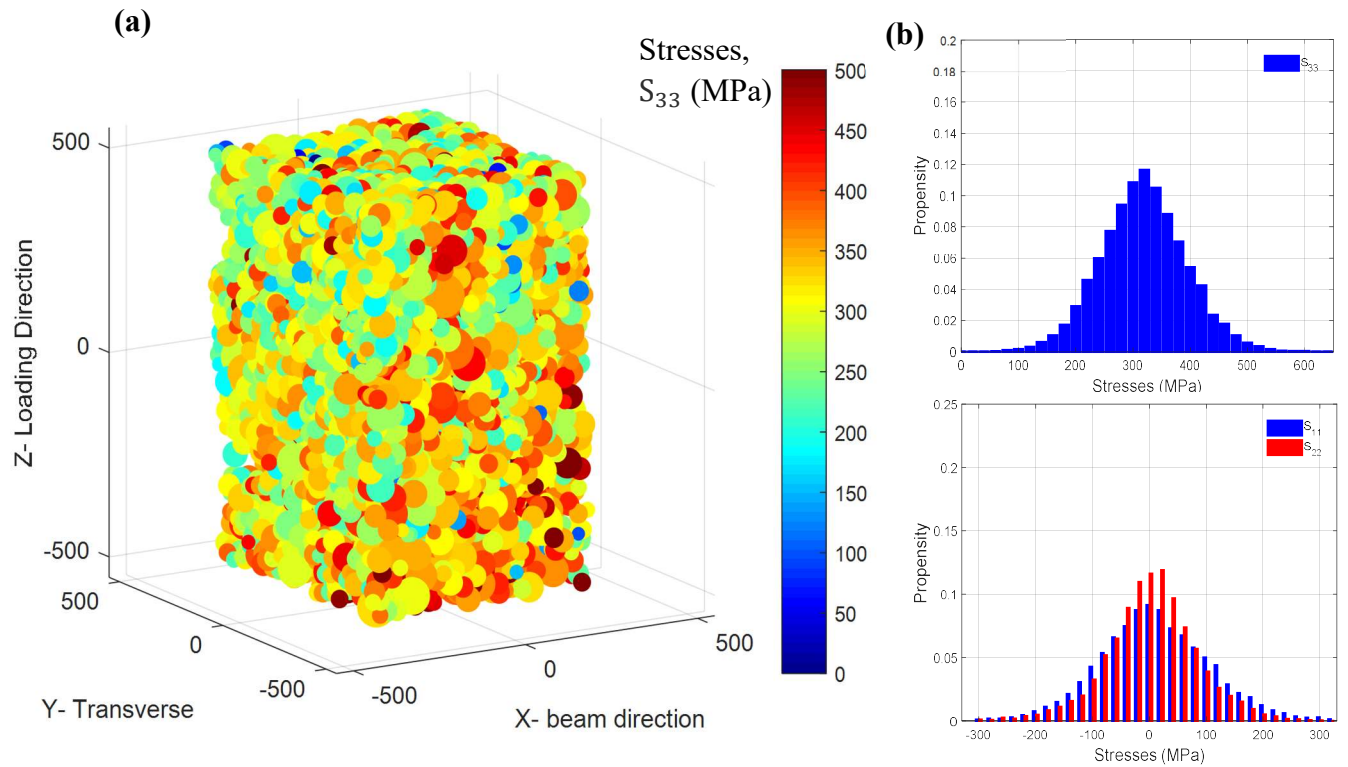


**Figure 4.6: (a) Grain map and (b) stress distributions in step 4**

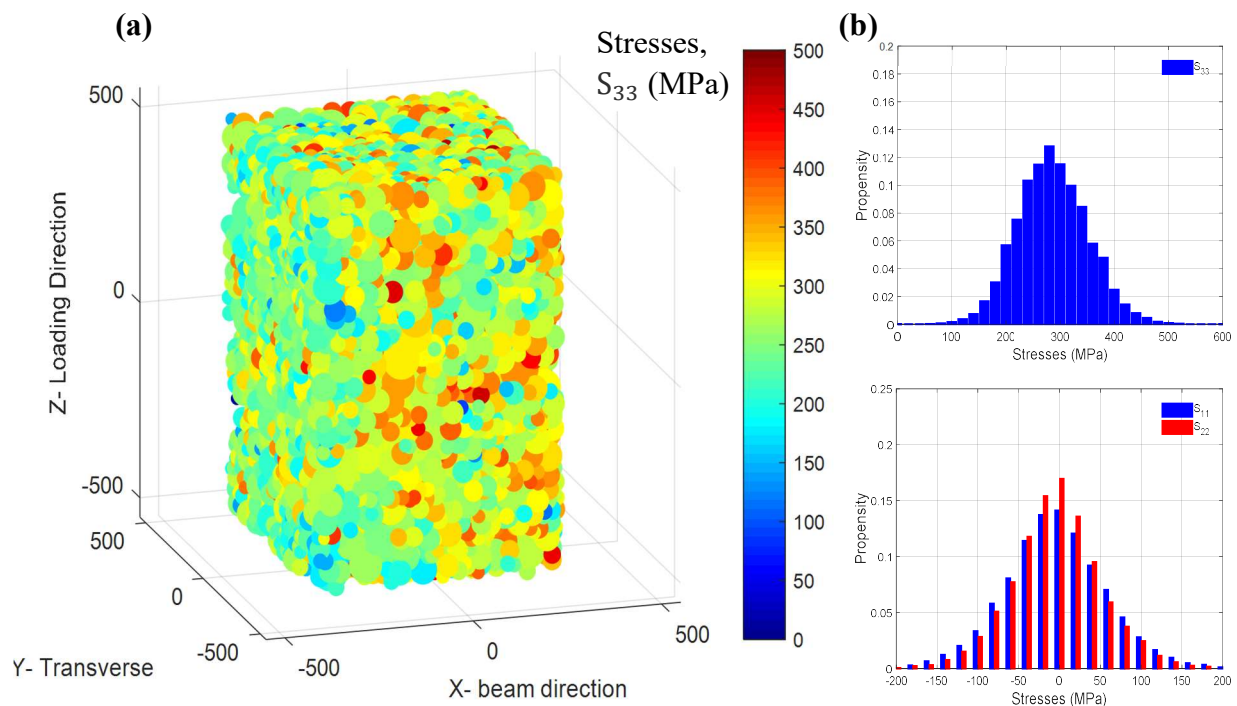


**Figure 4.7: (a) Grain map and (b) stress distributions in step 8**

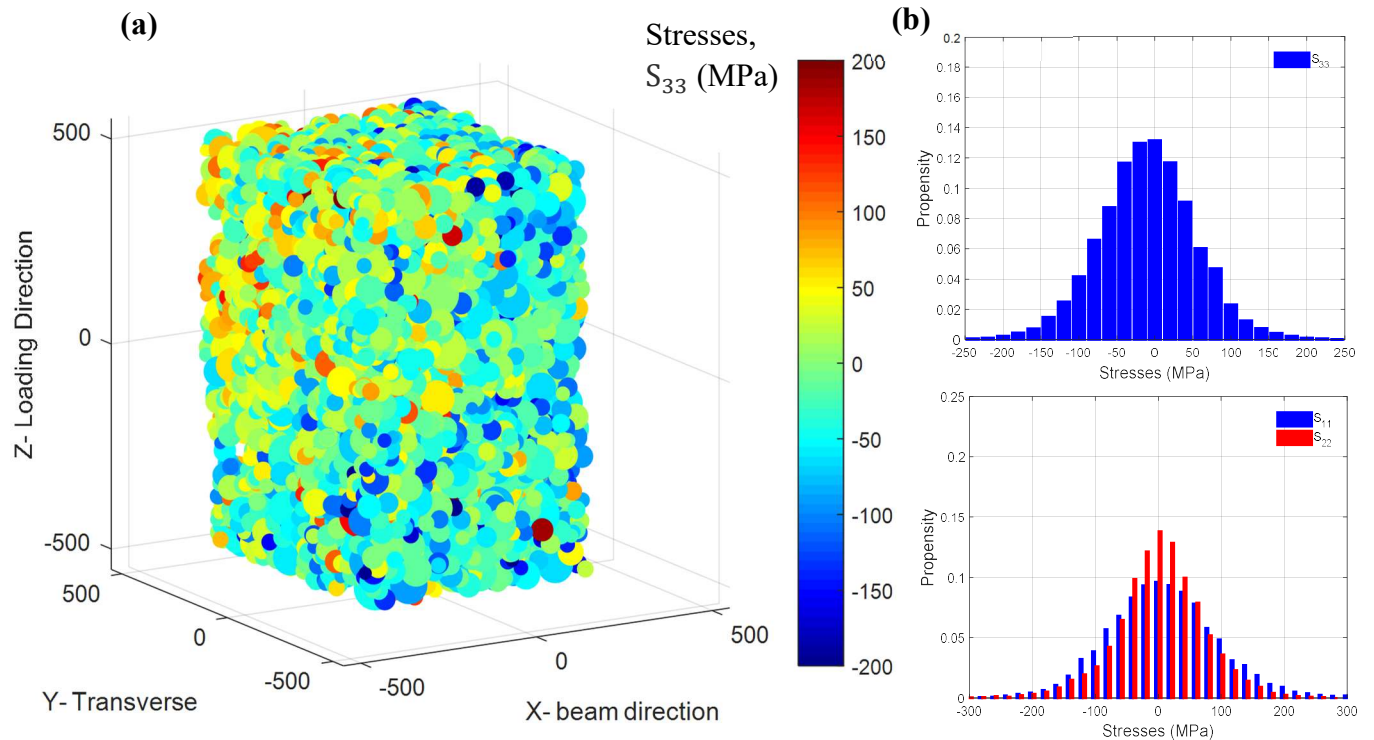


**Figure 4.8: (a) Grain map and (b) stress distributions in step 9**

With the increase in the applied load, the shift in the stress distribution along LD occurs towards the right. The shape of the distribution remains gaussian, shown in figures 4.6 to 4.8, with the average stresses in the grains equivalent to the applied stress in all directions. The grains average stresses should be equal to the applied stress to enforce force equilibrium. During unload, the distribution shifts back to the left as a result of stress drop. The distribution range changes in each step where it increases in the plastic zone from step 3 (onset of plasticity) to step 8 and decrease from maximum applied strain (step 8) to unload (step 9). The increase in the distribution arises from the increase in the force interaction at grain boundary due to several deformation mechanisms, including deformation twinning.

The texture of the sample is engineered for twinning since a large portion of the grains have their c-axis oriented along the tensile loading direction. The change in the pole figures is one of the methods to monitor deformation twinning since it demonstrates the evolution of the specimen's texture under tensile load and this is demonstrated in figure 4.9.



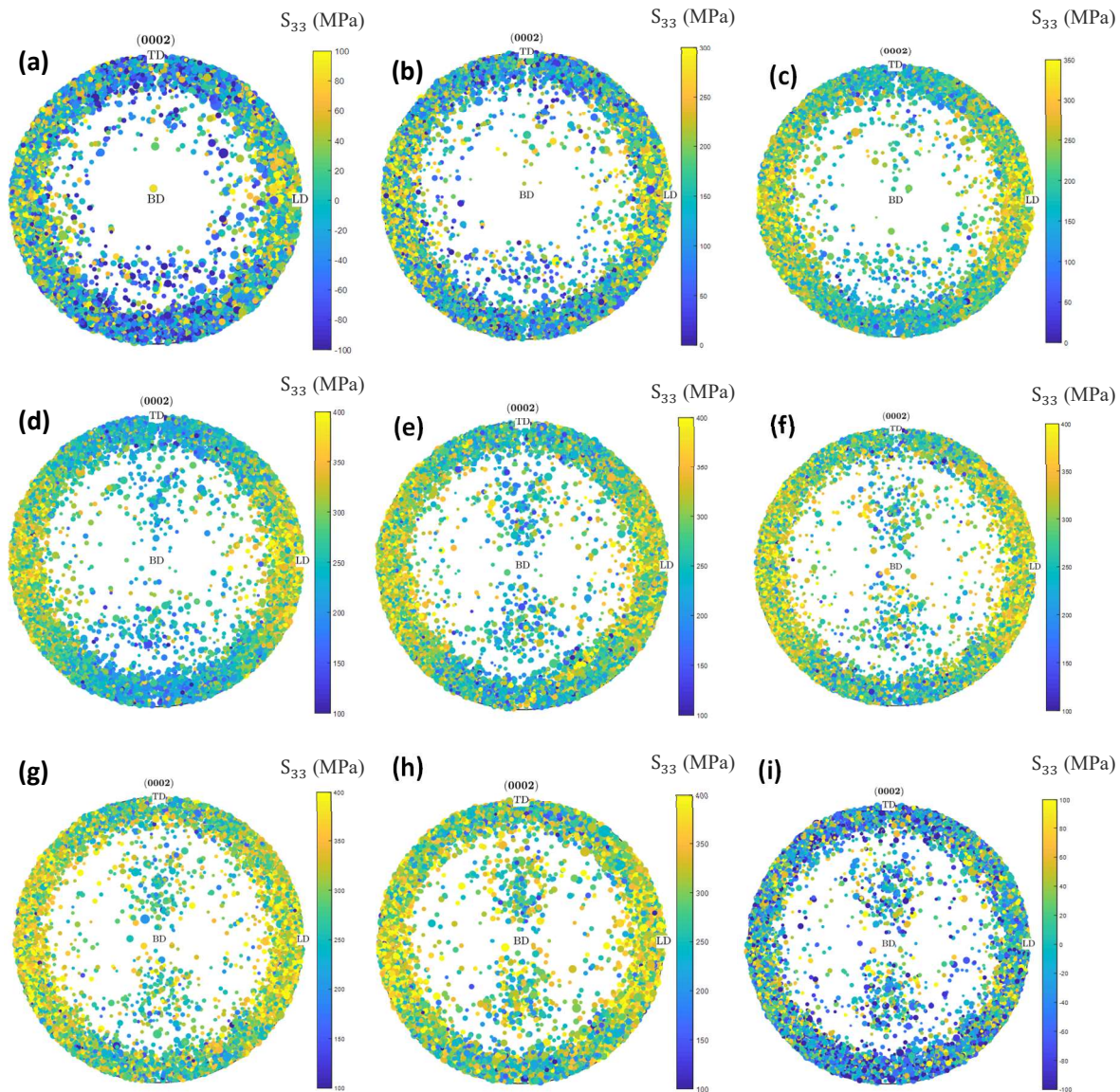


**Figure 4.9: Stress-based (0002) pole figures for steps (a) 1 to (i) Step-9. In (a)-(h) colors are coded based on measured stresses within grain in loading direction and in (i) colors are based on stresses in LD,  $S_{33}$ . The size of each spot is proportional to the measured grain relative volume.**

Figure X displays the basal plane (0002) pole figures of all grains in all steps and the color bar represents stresses along the LD. This pole figure is basically the stereographic projection of the (0002) plane from each grain on a sphere. Each dot on the pole figure represents a grain and the size of the dot is proportional to the volume of the grain. In all figures, the east and west sides of the pole figure, representing LD (z-axis), has higher stresses compared to the north and south of the figures, resembling the TD (y-axis). This simply shows that the hard grains, oriented along

LD, have higher stresses compared to soft grains, oriented along TD. Moreover, there are nearly no poles around the center, BD (x-axis), at the beginning of the experiment. However, as soon as the specimen enters the plastic region in steps 3 and 4, a cluster of spots appear around the center of the plot. Those poles represent the deformed twins nucleated upon loading in the plasticity region. In figures 4.9 (c) to (h), the stresses in the cluster of poles around BD are all lower than the stresses in the LD and this essentially means that the stresses in the twins along LD are relaxed compared to their parents. The number of spots around the center increase and their volumes also increases toward the end of loading indicating the rise in the twin volume fraction.

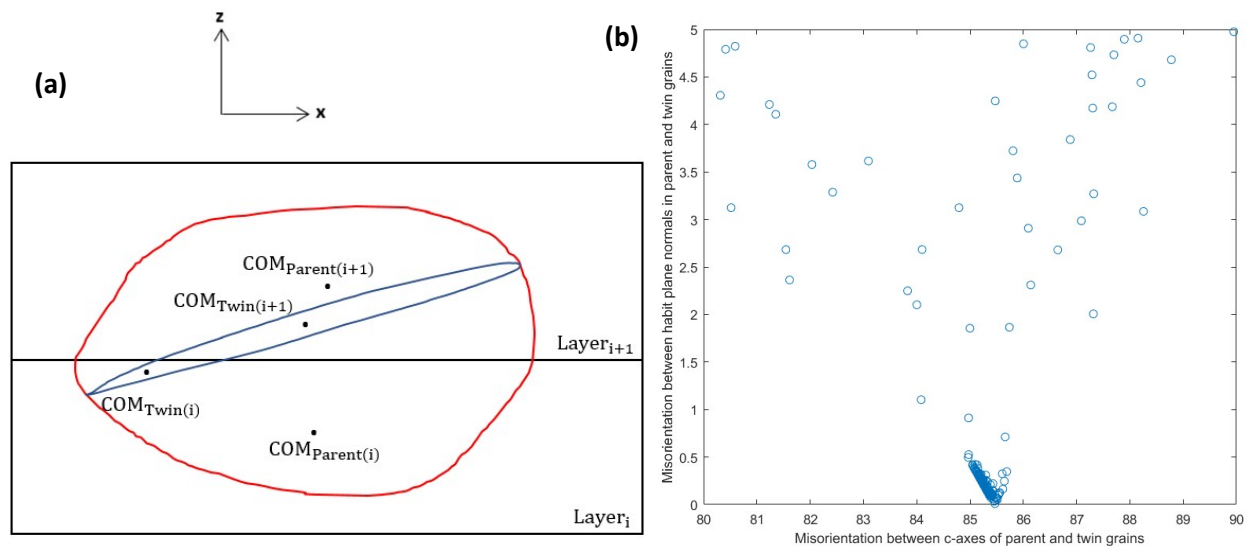


**Figure 4.10: (a) Schematic of a twinned grain in two layers and (b) Verification plot of the orientation between the parent and twin**

#### 4.4 Deformation Twinning Results

In the previous section, the overall trends of deformation twinning are discussed however capturing parent-twin pairs requires a different strategy. Twins in the grain maps and pole figures are considered as separate grains due to their unique orientation compared to their neighboring grain, i.e. parent grain. The misorientation between the c-axes of a parent and twin grain should be  $85.25^\circ \pm 5^\circ$  and the twin habit plane should be the same for both parent and twin grains and this means that the misorientation between the plane normal of both grains should be less than  $5^\circ$ . Twin habit plane is the plane shared between the twin and parent, and for Zr and Mg samples are the  $\{1 -1 0 2\}$  planes. The twin-parent matching code starts by looking

for grains that are not matched in the previous step, i.e. new grains, and records them as potential twins. All unmatched grains, i.e. potential twins, in the same measured layer, demonstrated in figure 4.10, are the potential twins and are tested for both orientation criteria and distance criteria. Rather than checking for the parent grain in all layers, the search is restricted to the layer where the twin was detected thereby improving the computational efficiency and ensuring that both twin and parent grains are close to each other regardless of the distance between their COMs. However, before the misorientation criteria is tested, the distance between COMs of the potential parent and twin should be less than the summation of their radii. If these potential twins satisfy the first criterion of c-axis misorientations, the second criterion is tested by ensuring that the twin habit plane is one of the six variants of  $\{1\ 1\ 0\ 2\}$  tensile twin systems. This was done by calculating the normal to the habit plane using the parent and twin orientation and ensuring that the two normals are aligned (misorientation  $< 5^\circ$ ). Even though misorientation was kept below  $5^\circ$ , the produced results of all parent-twin pairs that satisfied all the criteria are plotted in figure 4.10 (b) and the trend shows that most of the pairs have their misorientations less than  $1^\circ$  thereby illustrating excellence in the accuracy of the recorded pairs.

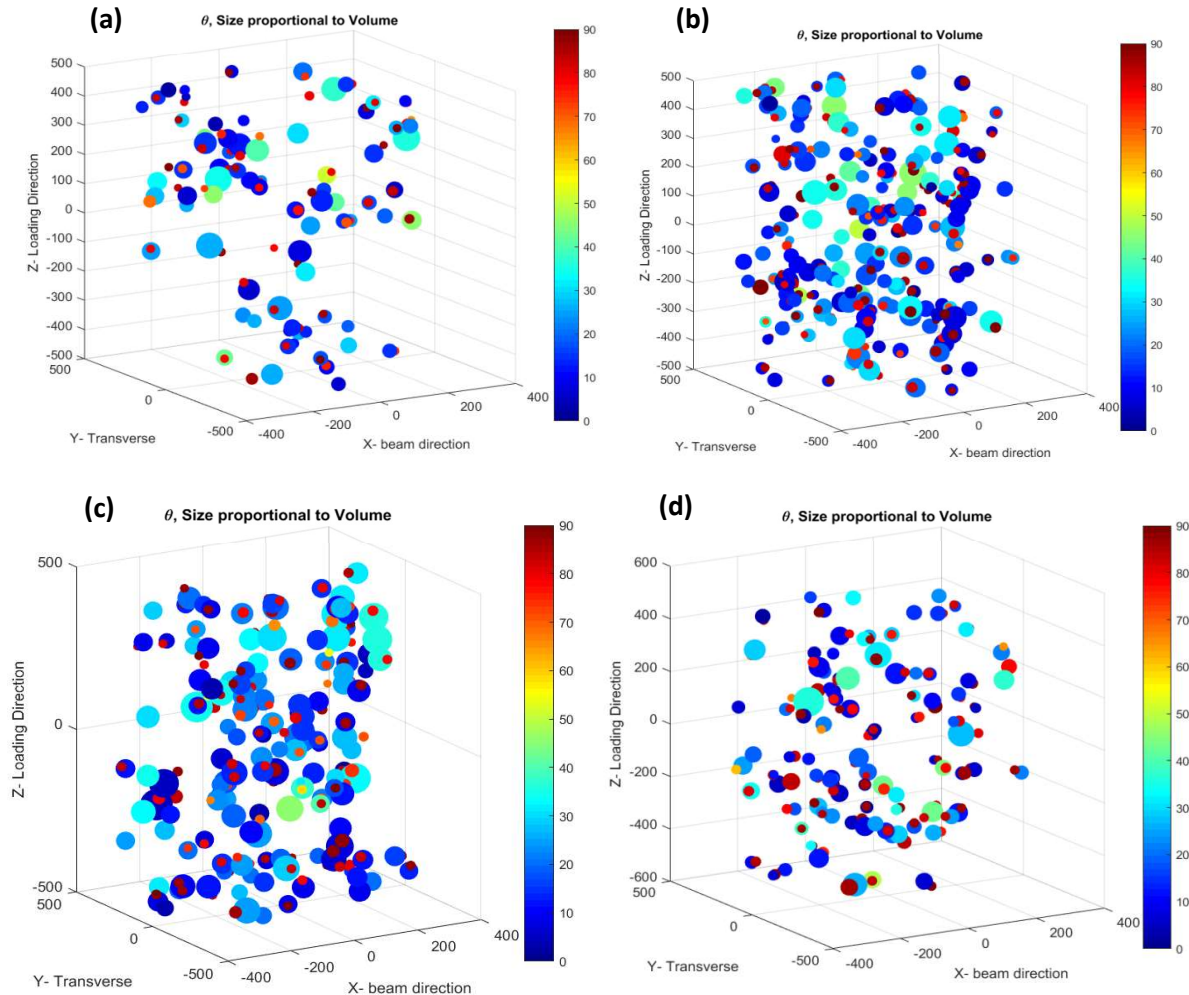


**Figure 4.11: Scatter plots of parent-twin pairs for (a) Step 4, (b) Step 5, (c) Step 6, and (d) Step 8. Colors represent c-axis misorientation with LD and the size of spheres are proportional to the measured relative volume for each grain.**

Using this algorithm, the nucleated twins are captured by searching for new grains between two consecutive steps starting from step 1 to step 9. Those twins are then matched with the latter steps to capture the trends in their stresses and volumes. The same process is also carried out on the parent grains and the trends in their properties are compared to those of twins. Figure 4.11 shows the parent-twin pairs nucleated in steps 4, 5, 6 and 8. From the figures, the twins are red in color and parents are blue and since the twins are just nucleated, the parent grains are larger than twins. Ideally, a cluster of three grains that includes the two split parent grains and twin grain would be expected in the map. However, due to the low spatial resolution of the technique,

the diffracted beam from the split grains may overlap and appear nearly on the same collection of pixels of the detector.

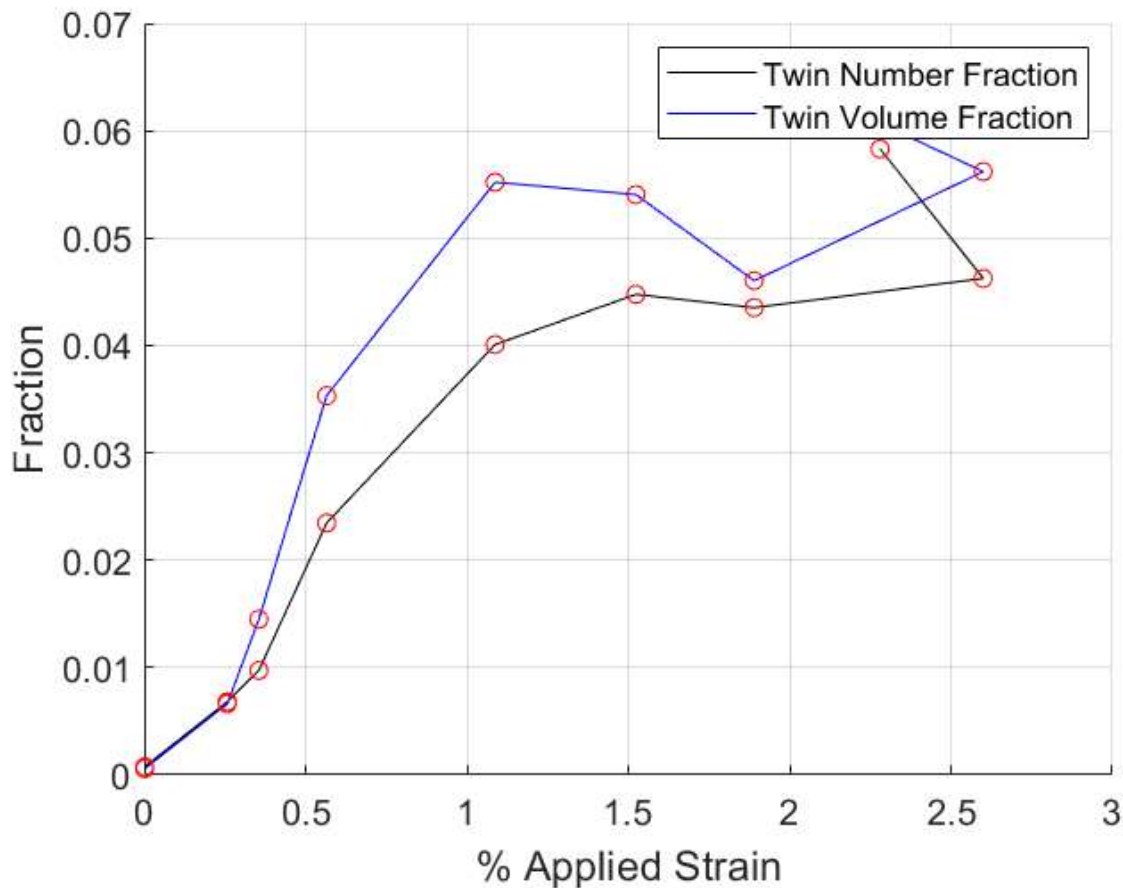


**Figure 4.12: Progression of twin number and volume fraction with respect to the applied strain**

All grain IDs acquired for all parent-twin pair in every step is assembled in a matrix. Using this matrix, the total number of twins can be quantified in figure 4.12 as twin number and volume fraction and the number of twins in each step is tracked through this method. The final twin volume fraction, after deformation, is close to the value provided in the literature, [4], however the variations occurring during deformation is inconsistent with the trends in the literature. The twin volume fraction in this experiment is calculated as the summation of the relative volume of twins divided by the summation of the total volume of all grains in the scanned volume. Another interesting observation is the rise in the twin volume and number fraction upon unloading the specimen in the last step. Upon increasing the applied strain in the plasticity region, the nucleated twins continue to grow [29]. This results to larger and brighter peaks for bigger twins,

which can be captured by the peak-searching algorithm. In addition, upon unloading, the elastic lattice rotation within grains will be restored resulting in better match between simulated peak and measured peak from the experiment and increasing the grain indexing rate (more peaks will fall under the determined tolerance for peak search). Similar to the first three steps in the plastic region, bright and round peaks are easily captured by the peak-searching algorithm.

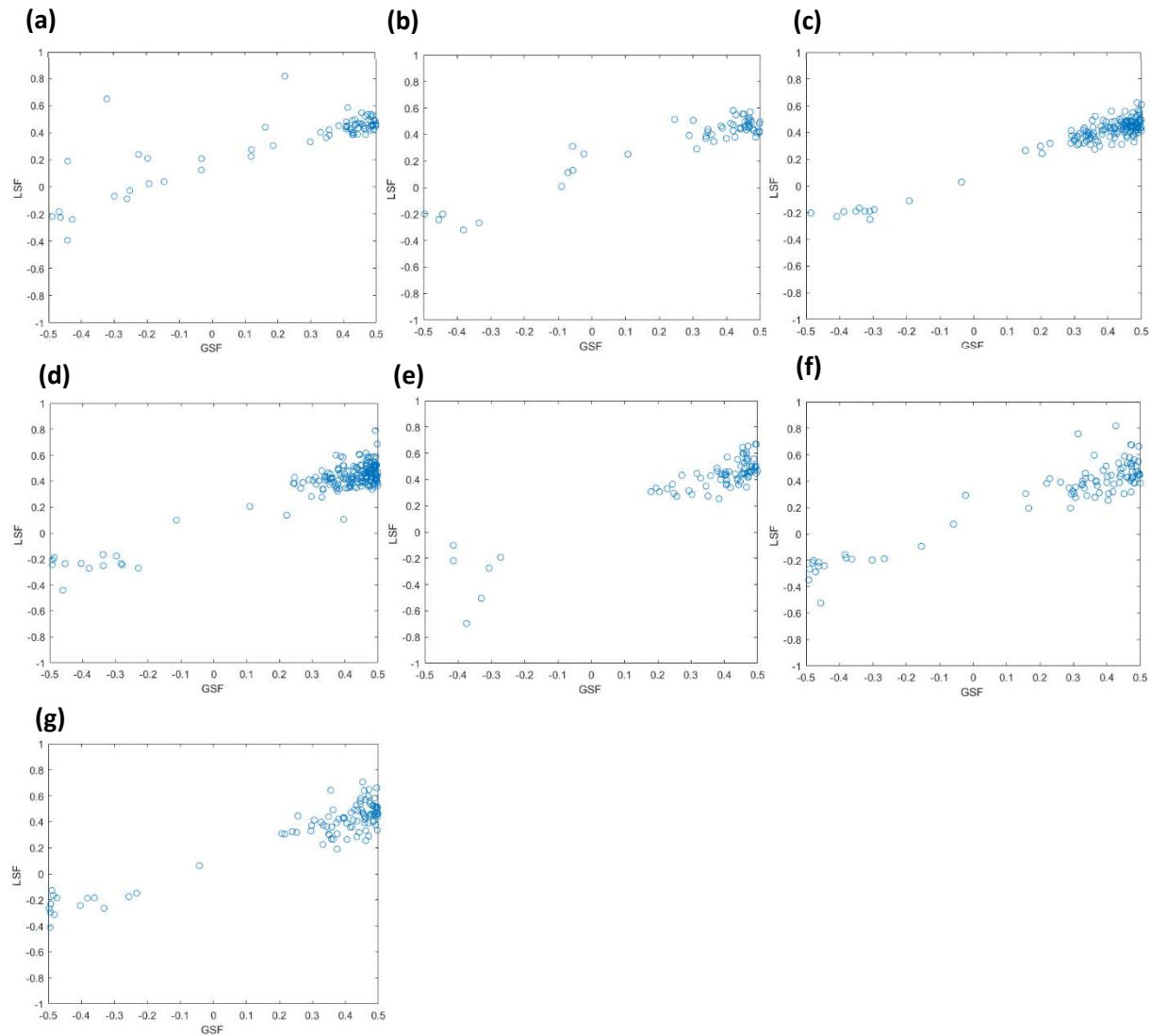


**Figure 4.13: Twin Local Schmid Factor as a function of twin Global Schmid Factor for twins nucleated in steps 2 to 8**

Understanding twin nucleation is the first step for developing predicting numerical models. The main factor that causes twin nucleation in any parent grain is the misorientation of the c-axis of

the parent grain with the loading direction or simply the Schmid factor of the any six twin variants. Generally, Schmid factor resembles the likelihood of activating a slip or twin system depending on the direction of the applied load. The higher the Schmid factor, the higher the chance that the slip or twinning system is activated. Therefore, in the case of tensile twinning, the variant with the highest Schmid factor is expected to twin as opposed to the other twins. In an ideal case where the c-axis is oriented along the loading direction for a uniaxial loading situation, the Schmid factor reaches a maximum value of 0.5 and crystal is the best position to twin. The results in figure 4.13 show the relation between the local Schmid factor (LSF) and global Schmid factor (GSF) of each nucleated twin from the 2<sup>nd</sup> step all the way to unload. The LSF is calculated using the tensorial average stresses of the parent grain in the global coordinate in the step prior to twin nucleation step. For example, if the twin nucleated in step 5, the measured tensorial stress of the parent in step 4 is used for calculating LSF. The GSF is calculated using the unit vector of the applied load. In all steps, the trend shows that most of the twins generate at a high Schmid factor regardless if its LSF or GSF and a linear relation between LSF and GSF. In all the trends, there are few twins with low LSF and GSF that disproves the general understanding that the parent grain needs to be a hard grain to twin. These grains could have probably twinned due to the stresses in the neighboring grains or stress/misorientation gradient at the grain boundary. Another possible explanation would be twin extension from the neighboring grain to the parent grain. Finite element modeling and deep analysis of 3D results are required to confirm which mechanism is active.

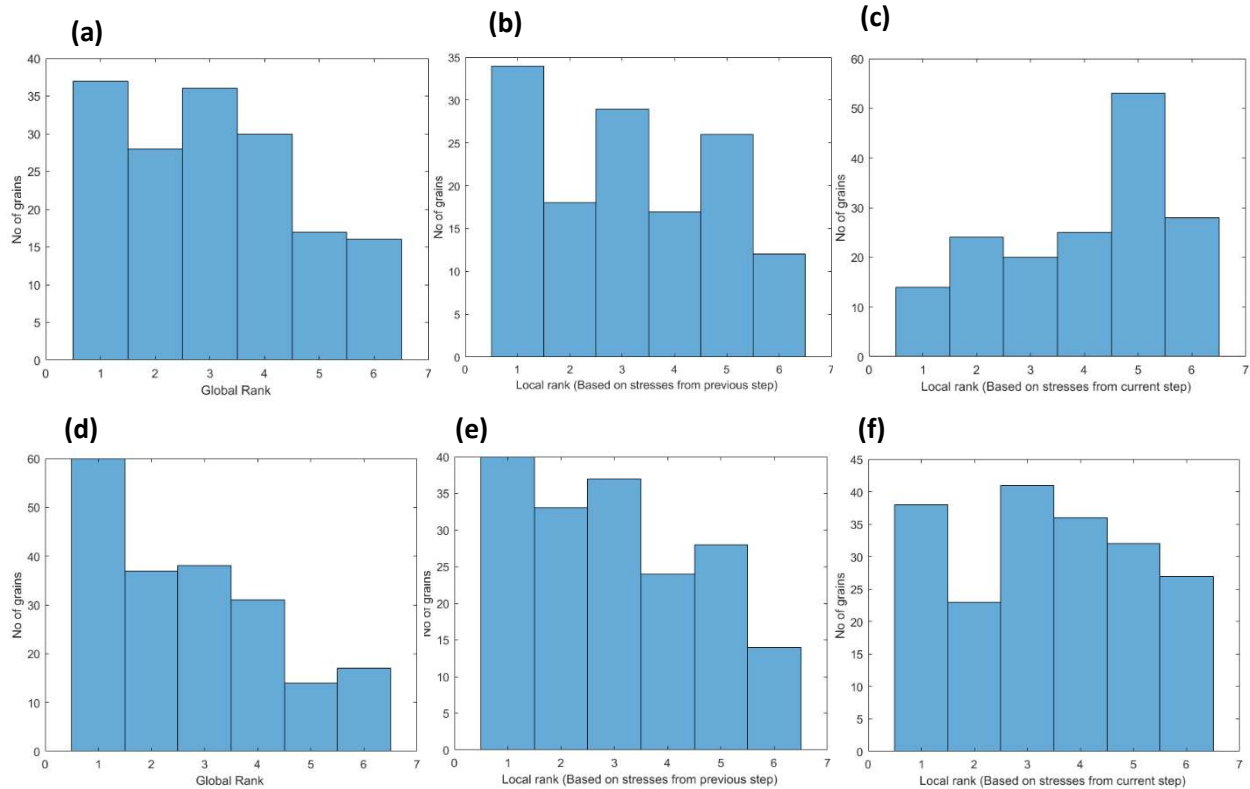


**Figure 4.14: The rank of twinned variant (a,d), in 4 and 5 respectively, based on Global Twin Schmid factor (b,e), in 4 and 5 respectively, Local Twin Schmid factor using the measured stress in the parent before twinning (c,f), in 4 and 5 respectively, Local Twin Schmid factor using the measured stress in the parent after twinning.**

Figure 4.14 demonstrates the rank of twinned variant and sorts them from the highest variant to the lowest, where highest has the highest Schmid factor. The top 3 figures belong to twins that nucleated in the 4<sup>th</sup> step and the bottom 3 figures belong to twins that nucleated in the 5<sup>th</sup> step. Ideally, all grains are expected to twin at the variant with the highest Schmid factor and all the grains would appear at the 1<sup>st</sup> rank. According to figures 4.14 (a), (b), (d), and (e), most of the twins in step 4 and 5 twinned with their strongest variant. However, there are many other grains that are twinned with low Schmid factor. In figure 4.14 (f), the LSF is calculated from the parent grains in the same step as the nucleation step and the trend is completely different from the expected trend since the stresses in the parent grain changes after twin nucleation. This shows that once twinning happen, the status of the stress within the parent changes and the most active variant may not stay as the predominant variant.



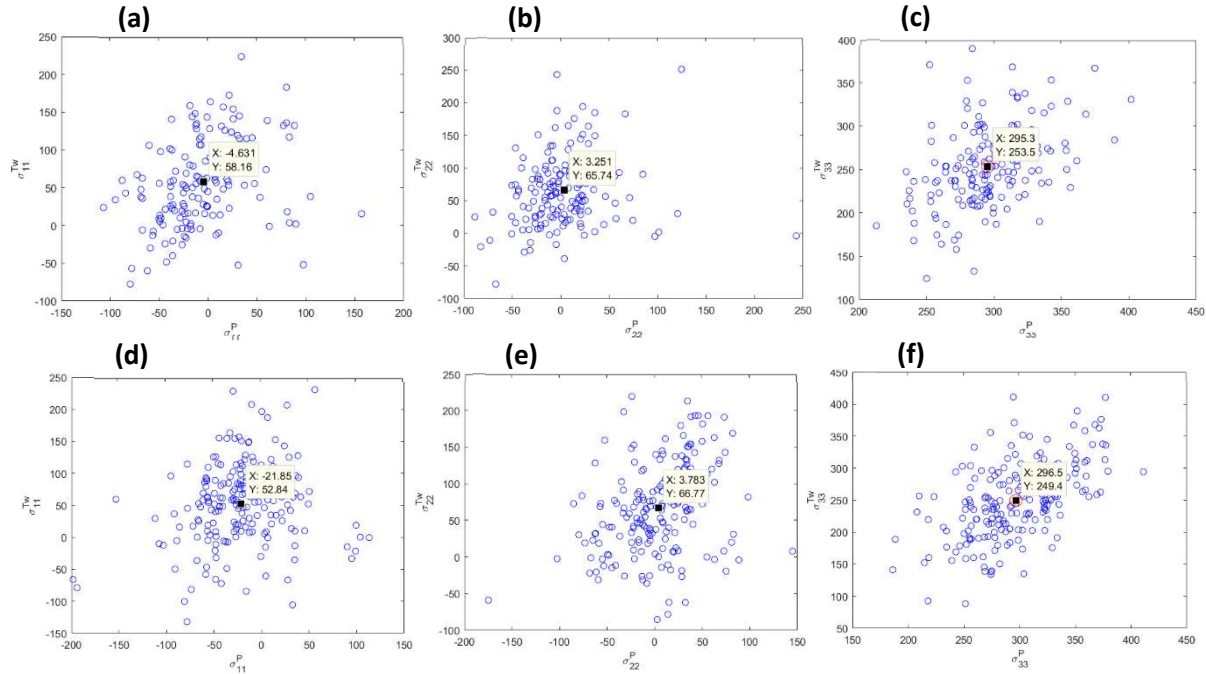


**Figure 4.15: (a)  $S_{11}$ , (b)  $S_{22}$ , (c)  $S_{33}$  of the parent and twin pairs in step 4 and (d)  $S_{11}$ , (e)  $S_{22}$ , (f)  $S_{33}$  of parent and twins in step 5**

Figure 4.15 shows the measured stresses in all parent and twin grains after twins have nucleated in step 4 and 5. The stress plotted in figure 4.15 are in the global coordinate system of the specimen. The numbers displayed in the figures using the tracker and the red circle are the average for all pairs. In step 4, the average stress, in the LD ( $S_{33}$ ), in the twin (253.5 MPa) is lower than the parent grain (295.3 MPa) and this same trend is observed between the twin (249.4 MPa) and parent grain (296.5 MPa) in step 5. On the other hand, the stresses in the other two axes are lower in the parent compared to the twin for both steps [40], [67]. Results discussed in the past confirm the trends acquired from figure 4.15 and the probable explanation of this behavior would be the crystallographic orientation of the parent and twin grains. The parent grain has a hard orientation in contrast to the twin. The lack of slip activity in a hard orientation causes an increase in the lattice strain as opposed to the soft oriented twins.

## 4.5 Conclusions

An algorithm was developed to capture the twins that nucleated during in-situ deformation of a zirconium sample. Local and global stresses were used to calculate Schmid factors and it was shown that many nucleated twins have high local and global Schmid factor. It was also observed that a few parent grains having low twin-Schmid factors. This indicates that resolved shear

stress is not the sole factor of deformation twinning and other mechanisms that lead up to deformation twinning is happening. Variant ranks were used to determine whether twinning occurs on the variants with the highest Schmid factor. With using the grain-measured stresses after twinning the twin ranks are shown to become disordered which indicates that the active variant does not stay as active, once a twin is formed. This is because the stress state in the parent grain after twinning is significantly changed in comparison to grain-stress prior to twinning. Stresses in twins along the loading direction are relaxed compared to the stresses in the parent grains. This is due to the hard and soft orientations of the parent and twin grains respectively. This also explains the high stresses in twins along the other two axes. Twin volume and number fraction were recorded for every step and plotted with respect to strain. It was shown that the calculated twin volume fractions overestimate the expected twin volume for small macroscopic strains.

## Chapter 5

### 5. Analysis of 3D-XRD results on Mg AZ31

This aim of this chapter is to discuss the results of 3D-XRD experiment on the MgAZ31 specimen after post-processing the raw diffraction patterns. This section discusses the measured grain maps as well as the evolution of texture as function of applied load. Macroscopic and microscopic stress evolution, nucleation of twins, de-twinning, variant selection, as well as the state of the stress within twin and parent pairs are discussed.

#### 5.1 Details of 3D-XRD results

This 3D-XRD experiment was carried out through nine loading steps and it is the 1<sup>st</sup> ever in-situ cyclic loading experiment done so far. Over 8,000 grains are captured for which the six components of the stress tensor were measured individually. The grains-average stresses and error bars are recorded in table 5.1 with other information such as COM error bars and the macroscopic applied stress. Similar to the zirconium experiment, the macroscopic strain was measured by tracking the movement of silver wires mounted on the specimen, as well as by the strain gauge that was attached to the specimen. All other measurements including macroscopic stress and micromechanical stresses are recorded in the same procedure as the zirconium experiment.

Table 5.1: 3D-XRD Table of Results for Mg AZ31

Step ID	Step Description	Applied Strain(%)	Macroscopic Stress (MPa)			No. of grains	Average Number of Peaks per grain	COM Position Error (microns)	S11 (MPa)	S22 (MPa)	S33 (MPa)	S23 (MPa)	S13 (MPa)	S12 (MPa)	Beam Size
			Before Alignment	After Alignment	After Measurement										
1	Mg4_ON_	-0.0009	3	3	3	8180	141	5.4974	-0.5116	1.2413	1.4939	0.1965	1.2387	-0.1823	0.1 mm height
									10.3905	7.0671	5.5627	2.1303	2.3708	3.4057	
2	Mg4_35N_	-0.0759	-40	-36	-35	8455	144	5.5039	-3.1339	1.7617	-41.8667	-2.6172	2.1804	-0.8052	
									10.4073	7.0758	5.5635	2.1385	2.3785	3.4037	
3	Mg4_52N_	-0.2832	-59	-57	-54	7653	127	6.2838	-1.6408	3.4283	-55.8007	-1.7598	1.4466	-0.9033	
									11.9188	8.0578	6.4311	2.4689	2.7820	3.9162	
4	Mg4_ONT_	-0.1135	2	2	2	8134	131	6.1819	-1.7472	-0.4622	1.6829	0.3282	1.3307	-0.5936	0.05 mm height
									11.8084	7.9587	6.3422	2.4307	2.7276	3.8555	
5	Mg4_25NT_	0.0985	28	25	25	5980	135	5.7803	-3.4070	-1.8299	20.7202	0.4398	3.7769	-0.7014	
									10.8879	7.3753	5.8699	2.2476	2.5199	3.5731	

The in-situ 3D-XRD experiment was conducted on a MgAZ31 specimen and measurements were done at 5 different steps. The stress-strain curves of the in-situ and ex-situ experiments are provided in figure 5.1 (d). The first measurement is taken before applying any significant macroscopic load (pre-load step), the second measurement is taken after the specimen was compressed to the onset of plasticity and the third measurement was taken after the specimen was loaded to the plastic zone. The fourth measurement was taken after unloading the specimen and the final measurement was taken after loading the specimen to 25MPa of tensile stress. Using these five measurements, information about individual grains can be acquired through the entire cyclic loading experiment. The maximum strain is about -0.3% at the 3<sup>rd</sup> step.

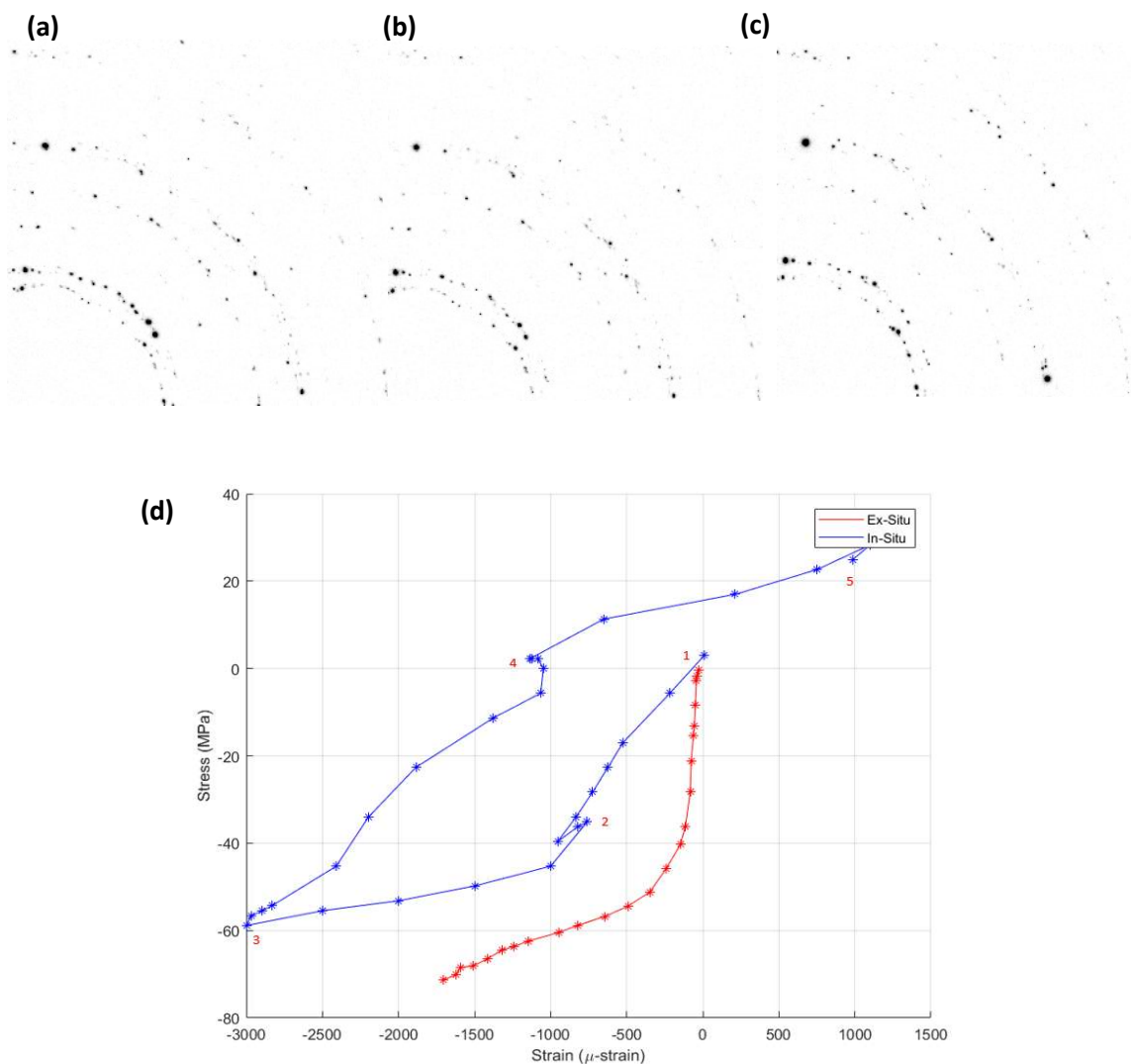


**Figure 5.1: Diffraction patterns in (a) Step-3, (b) Step-4, (c) Step-5, and (d) Stress-strain curves of in-situ and ex-situ experiments**

During the diffraction measurement, an X-ray beam height of 0.1 mm (10 layers) was used for the first two steps, but this beam height was reduced in the following three steps to 0.05 mm (20 layers). The number of indexed grains is initially 8180 as provided in table 5.1 and then it rises due to the increase in the number of grains in the scanning volume as the specimen is being compressed thereby allowing more of the specimen to fall into the scanning range. This is also reinforced by twinning. This number drops after the specimen reaches plasticity due to peak broadening thereby exceeding tolerances in peak searching stage. After unload, the diffraction peaks become round due to releasing part of the elastic rotations thereby reducing the width of the peak and they fall back within peaksearch. The number of indexed grains is then drastically reduced because the specimen fractured during the measurement stage. Among the 20 layers covering the scanned volume, only 14 layers are measured in the last step corresponding to 70% of the entire volume. When comparing this volume to 70% of the volume in the remaining steps, the number of grains increases from the previous steps due to peak narrowing as dislocations rearrange and may annihilate upon stress reversal [68]. The measured peaks for steps 3 to 5 are provided in figures 5.1 (a) to (c). The stress drop during the measurement period is lower compared to zirconium since applied stresses are much lower than those applied for zirconium and since magnesium does not creep as much.

## 5.2 Grain maps and texture analysis

The matching process between any two steps is also conducted for the five loading steps in the magnesium experiment. Three different matching strategies are conducted, the first is between two consecutive steps, the second is between three consecutive steps and the final one combines all grains from all steps into one matrix. The maximum possible number of matches that can be acquired through all steps is equal to the step with the lowest number of indexed grains (step 5: 5980 grains). Using the first method, 4252 grains are captured and this is more than 70% of the indexed grains. In the second strategy, 3992 grains are captured since its more conservative than the first strategy. The final strategy records 9955 grains in a matrix combining all the grains from all steps.

**Table 5.2: CRSS of slip systems on Mg AZ31 [45]**

Plane	CRSS (GPa)
Prism	0.06
Basal	0.12
Pyramidal	0.1
Tensile Twinning	0.04

From figure 5.2 (a), a good agreement is observed between the weighted average of grain stresses and the applied macroscopic stresses. This confirms the selection of the initial 3D-XRD parameters as well as the single crystal parameters. Grains with their misorientation between the c-axis and LD less than  $10^\circ$  are defined as hard grains and more than  $80^\circ$  are defined as soft grains. The soft grains will deform plastically on the system with low CRSS values provided in table 5.2. From figure 5.2 (b), the hard grains clearly have a higher compressive stress during compressive loading in contrast to soft grains. However, upon reversing the load, the soft grains reach higher stresses since the starting point after unload in hard grains is lower compared to soft grains. The average microscopic stress of soft grains in all steps is close to the macroscopic stresses since almost all the grains in the specimen are soft grains. The hard grains demonstrated in figure 5.2 (b) are the only hard grains among all 4252 grains that are captured from the matching algorithm. The two grain maps provided in figures 5.2 (c) and (d) are the results of the matching process. Grain map in figure 5.2 (c) shows the matched grains between steps 1 and 5 with their COMs plotted in the 1<sup>st</sup> step and figure 5.2 (d) shows the entire grain map in step 5. All grains in figure 5.2 (c) are also seen in figure 5.2 (d) and some extra grains in figure 5.2 (d) representing the unmatched grains where most of them are twins (blue grains).

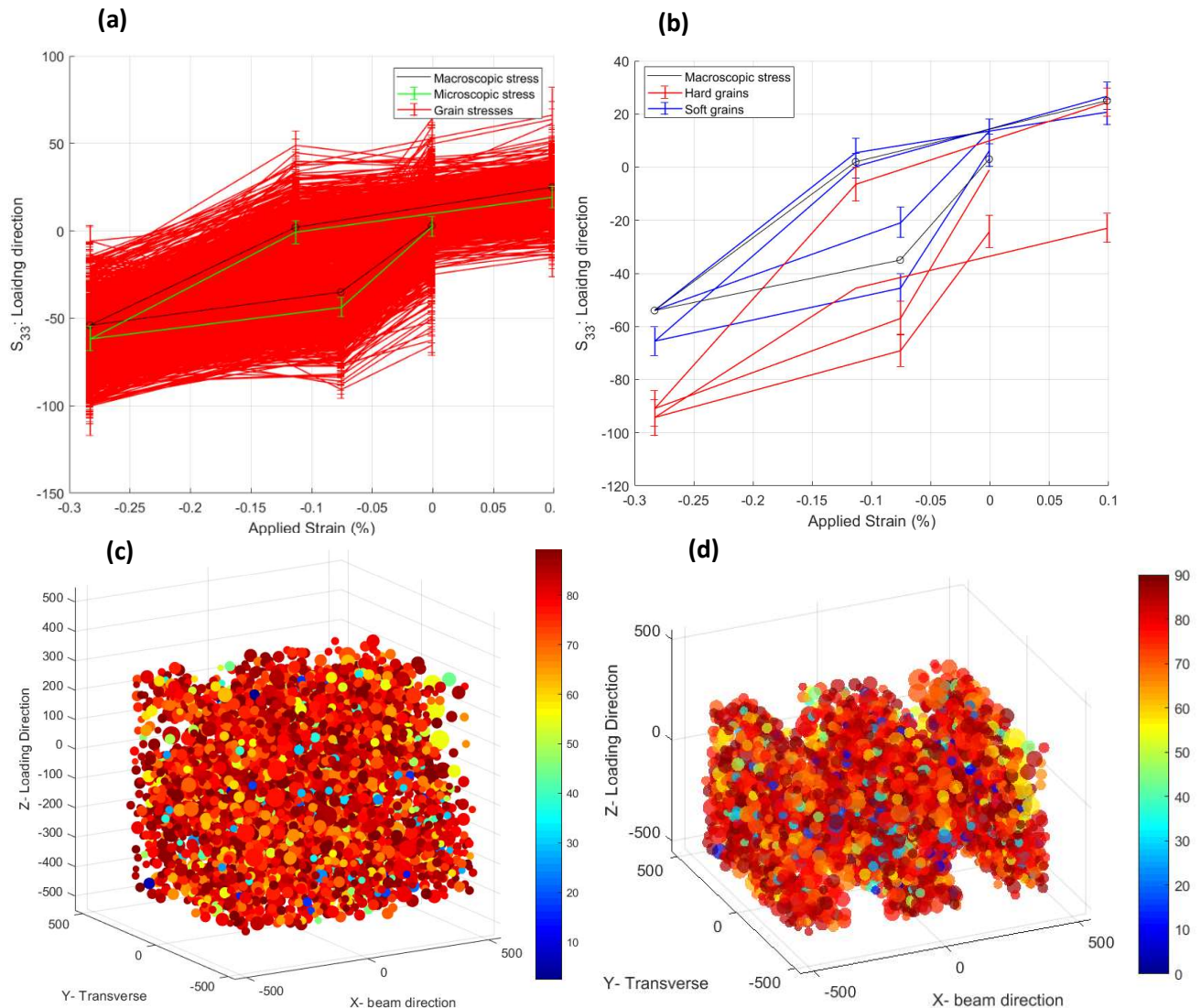


**Figure 5.2: (a) Macroscopic stress-strain plot and stress-strain plots of all grains that are matched in all steps, (b) Macroscopic stress-strain plot and stress-strain plot of hard and soft grains. The c-axis misorientation with LD of Step-1 & 5 matched grains are plotted in (c) step 1 and (d) sliced grain map in step 5**

Figures 5.3, 5.4, and 5.5 demonstrate the changes in the stress distributions and peak height upon stress reversal. Similar to zirconium, the range of stress distributions increases from step 1 to step 3 because of the rise in dislocation density in the plasticity region. In addition, the shift in the peak of the distribution of stresses in LD,  $S_{33}$ , also occurs due to increase in the macroscopic load in the same direction. Bauschinger effect is observed in the figure 5.2 (a) in the microscopic and macroscopic behavior of the specimen. Upon unloading and reversing the load in the tensile direction, the sample yields at about 2 MPa corresponding to step 4. This is



demonstrated in average grain stress-strain curve in figure 5.2 (a) where the slope of the curve in the elastic zone between steps 1 and 2 is parallel to the slope between steps 3 and 4 and not beyond that. The same stress-strain curve is also observed for Mg AZ31 cyclic loading in the literature [69]. The same behavior is observed in a different study conducted on Mg ZK60 and the behavior is termed as ‘Strong Bauschinger effect’ [70].

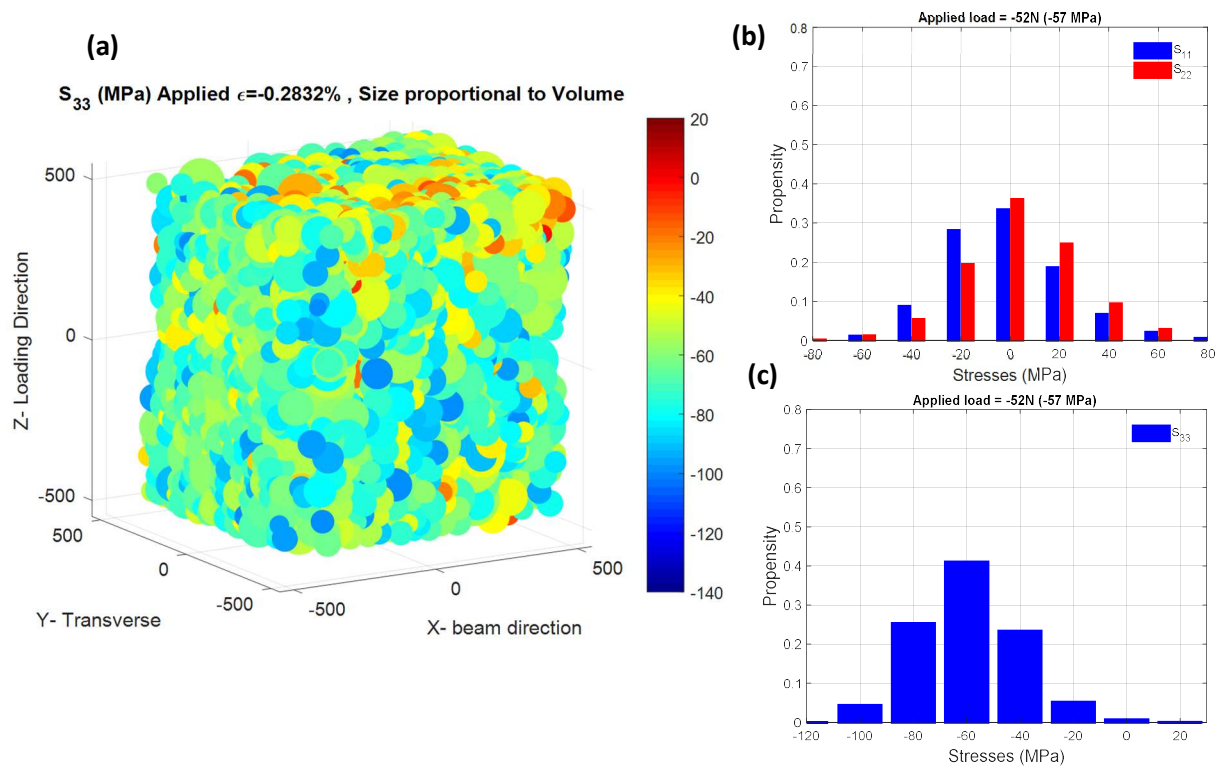


**Figure 5.3: (a) Grain map and normal stresses (b)  $S_{11}$ ,  $S_{22}$ , and (c)  $S_{33}$  distributions in step 3**

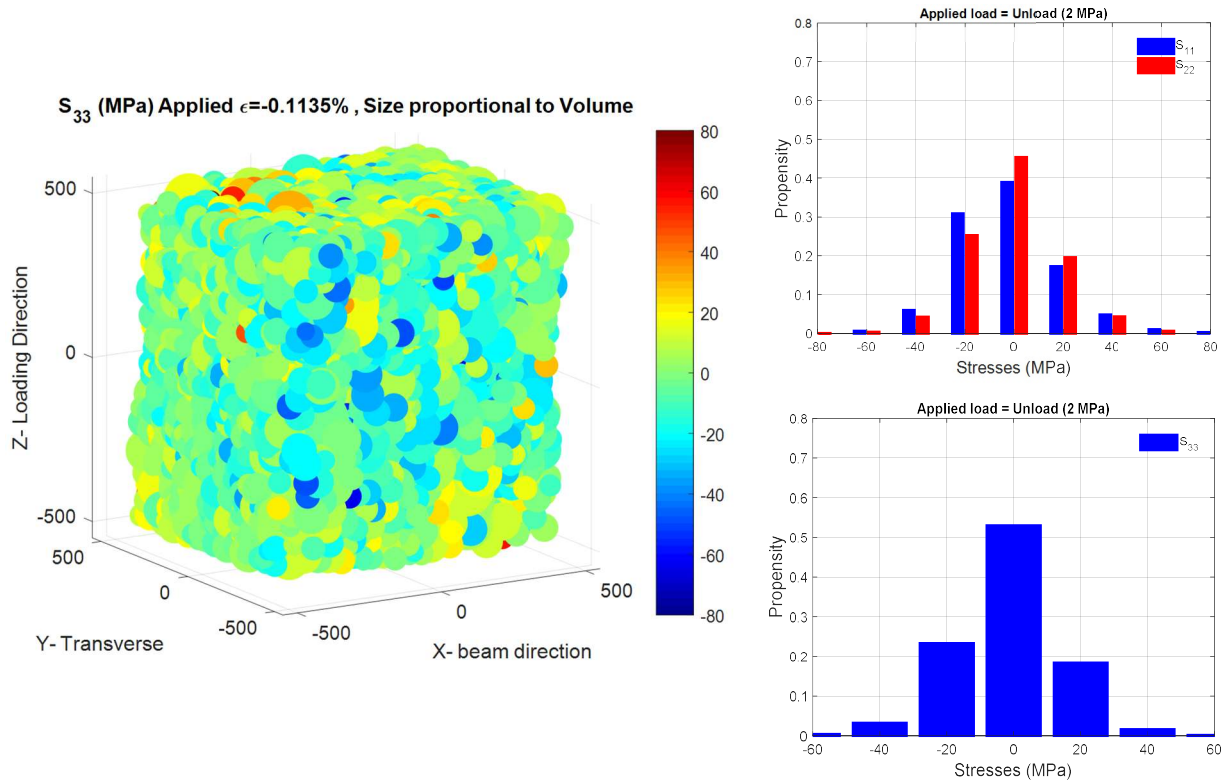


Figure 5.4: (a) Grain map and normal stresses (b)  $S_{11}$ ,  $S_{22}$ , and (c)  $S_{33}$  distributions in step 4

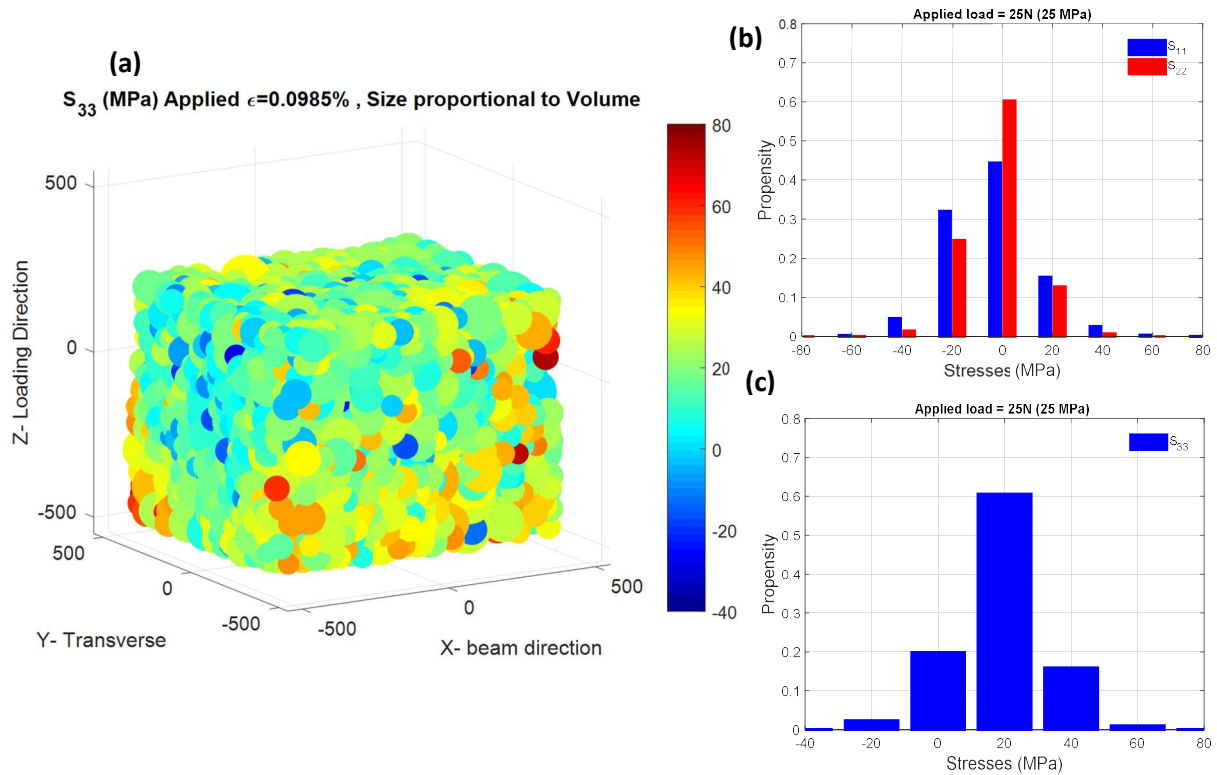
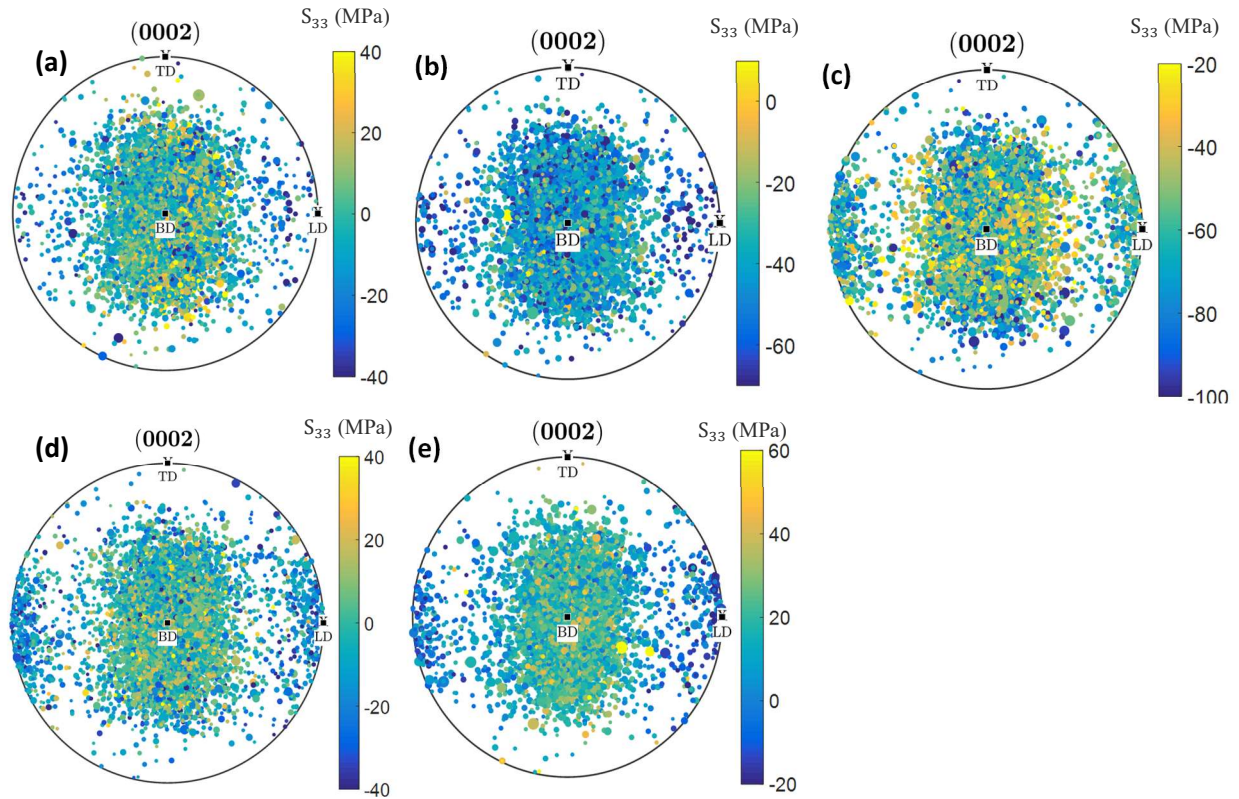


Figure 5.5: (a) Grain map and normal stresses (b)  $S_{11}$ ,  $S_{22}$ , and (c)  $S_{33}$  distributions in step 5

The transition in stress distribution between steps 3 and 4 in figures 5.3 and 5.4 reveals that the stress range drops upon unloading. The likely explanation to this behavior is the reduction in the stress distribution in individual grains due to elimination of elastic lattice strains and rotations. The stress distribution in the unload step is still higher than those of preload since the permanent movement of dislocations has caused orientation and elastic strain distribution between and within grains. During loading in the opposite direction, steps 4 to 5, the distribution of stress is reduced with an increase in the height of the peak as shown in figures 5.4 and 5.5. The possible explanation is that dislocations created in step 3 are now re-arranged and may annihilate when stress is reversed. This further confirms the trend observed in the variation of the number of indexed grains (section 5.1).



**Figure 5.6: Pole figures of steps 1 to 5: each dot represents a grain, and the size of the dot is proportional to the measured grain volume. Dots are color coded with respect to the measured stress.**

Figure 5.6 shows the texture of grains in each step (Full description of the figure is provided in section 4.3). In all figures, the stresses in the grains oriented along BD is lower than those oriented along LD. Since most of the grains are oriented along the BD, the average stress in the entire map is approximately the same as the average stress in soft oriented grains. Initially, there are few spots along BD however from step 3, a cluster of spots show up on the pole figure along LD signifying the nucleation of twins. The nucleated twins are oriented along the LD rather than TD due to preferential selection of the predominant twin variant (see below).

### 5.3 Twinning in 3D

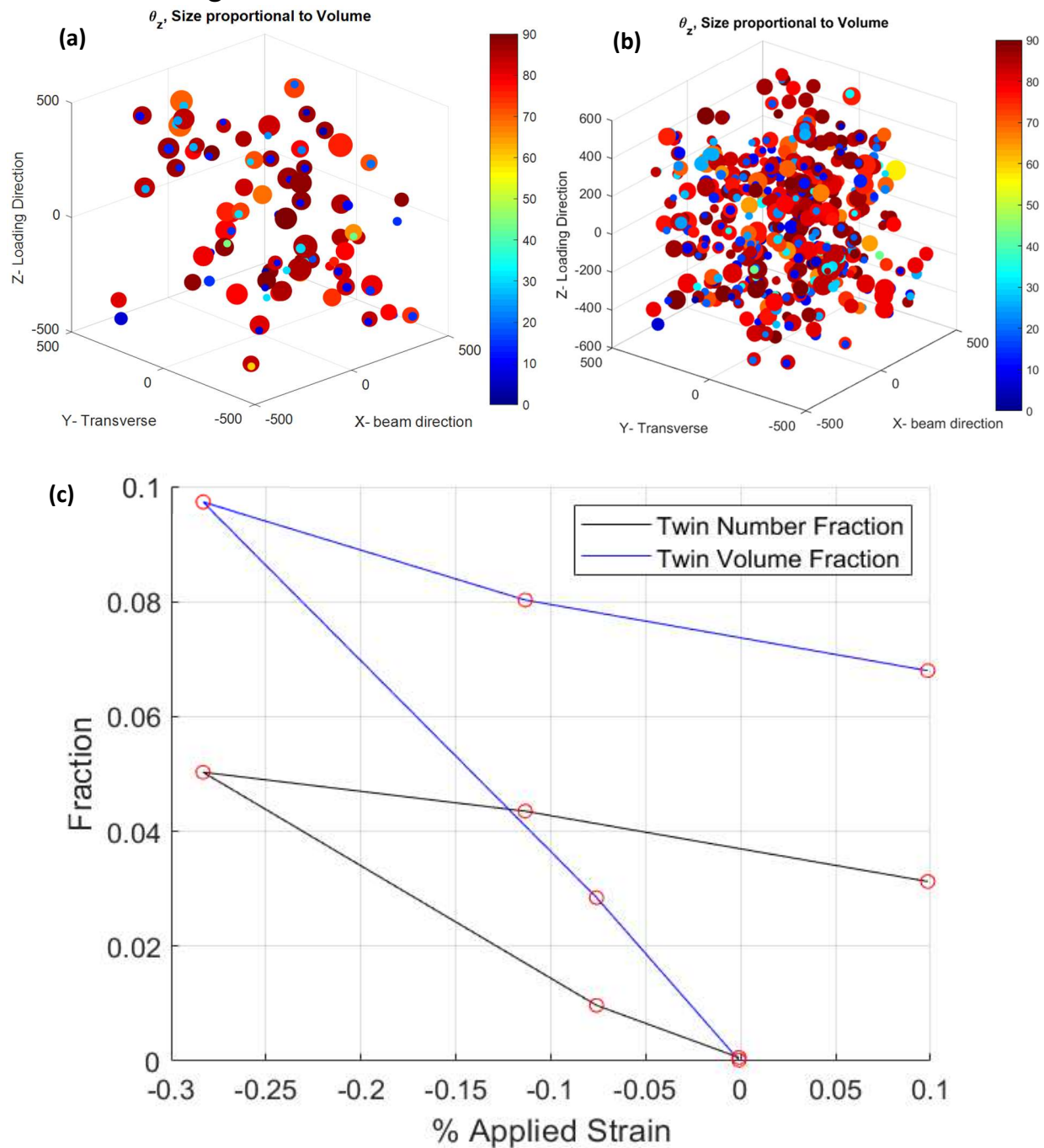


**Figure 5.7: Grain maps of parent grains and twins in (a) Step-2, (b) Step-3, and (c) Twin volume fraction**

The grain maps in figures 5.7 (a) and (b) show the nucleated twins in the 2<sup>nd</sup> and 3<sup>rd</sup> loading steps. The color bar represents the misorientation between the c-axis of the grains and the LD. The red spheres are the parent grains since they are oriented along BD and the blue spheres are the new grains representing twins similar to the results observed in the pole figures. From the

maps, it is clear that the red spheres are larger than the blue spheres since twins shown in the maps are the ones that just nucleated and therefore their volume is still small compared to the parent grain.

All parent grains and nucleated twins in each step from 2<sup>nd</sup> to 5<sup>th</sup> step are used for creating a matrix that adds up the pairs in the all steps and tracks the ID of the grains using the matching matrices. Using the final matrix with all the parent grains and twins in each step, the evolution of twin number and volume fraction is plotted in figure 5.7 (c). As expected, the twin number and volume fraction is initially close to zero. With increasing strain, twin volume fraction increases until maximum strain in step 3. During unload and load reversal, the twin volume fraction in specimen reduces due to de-twinning. The twin volume fraction acquired in the experiment from step 3 is larger than the values provided in literature [45]. The same disagreement is observed in the early stages of plasticity in zirconium but the final twin volume fraction after unload matches with the value in literature [4]. The possible reason for this trend is the fact that twins have an extremely high aspect ratio and small volume right after nucleation and this leads to uncertainties in the measured volumes from diffraction peak intensities. However, as the applied strain increases, the twins grow and the aspect ratio reduces. The reduction in the twin volume fraction after step 3 is because of detwinning during unload and load reversal. Crystal plasticity numerical simulations are required to understand the onset and mechanism of de-twinning.

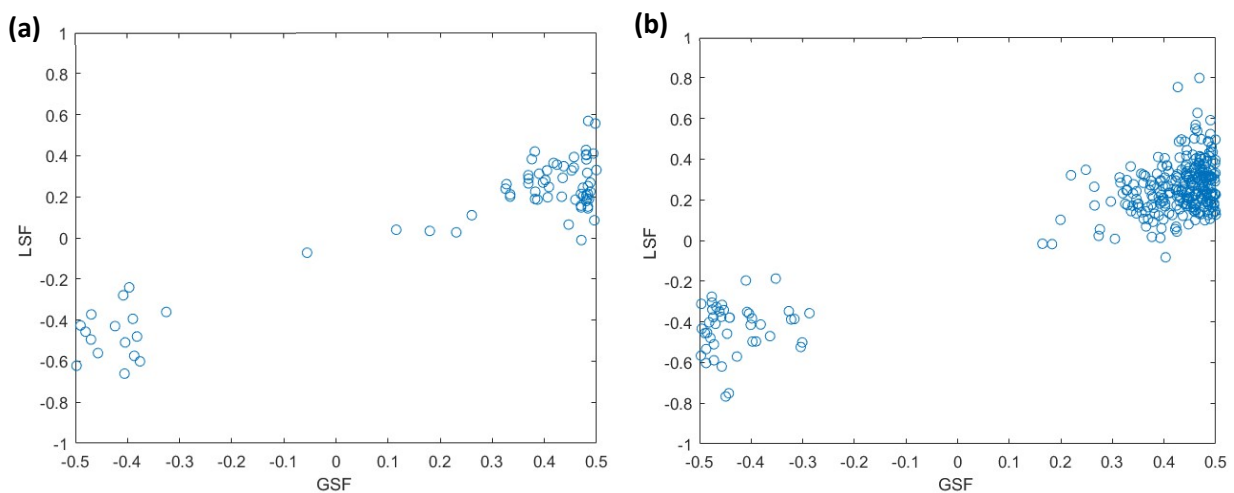


**Figure 5.8: Twin Local Schmid Factor (LSF) vs Twin Global Schmid Factor (GDF) in (a) Step-2 and (b) Step-3**

The relation between twin Local Schmid Factor (LSF) and Global Schmid Factor (GSF) in twins nucleated in steps 2 and 3, in figure 5.8, show similar trends to zirconium. While many parent grains have their twins at high GSF and LSF, some grains have low LSF and GSF in both steps. The LSF is calculated based on the stresses in the parent grains in the step prior to formation of twins. In contrast to zirconium, the direction of the applied load is negative (compressive stress) which is accounted for in the calculation of GSF. Grains with high Schmid factor in the twinning systems always tend to twin because their orientations favor twinning over slip. Even though twins occur at high Schmid factor, some twins can also with low Schmid factor due to grain neighborhood effects or size effects. This should be further investigated with numerical simulation.

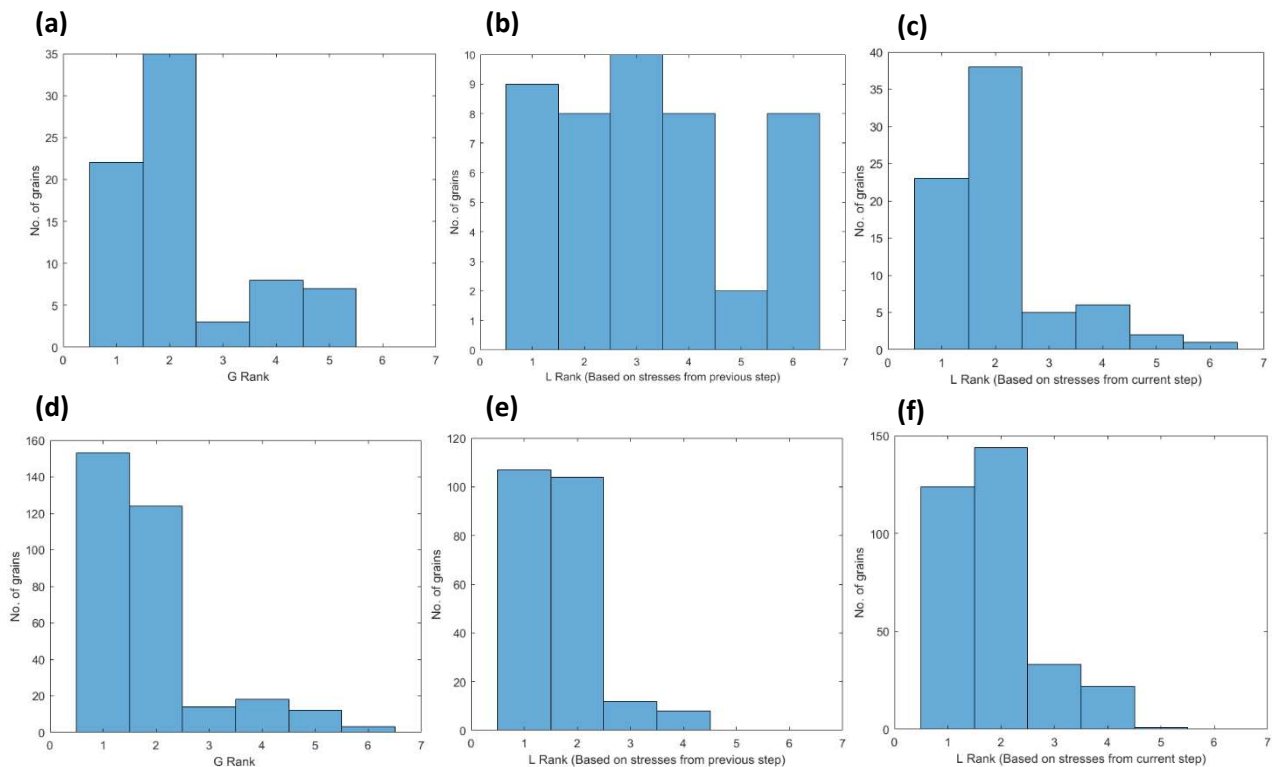


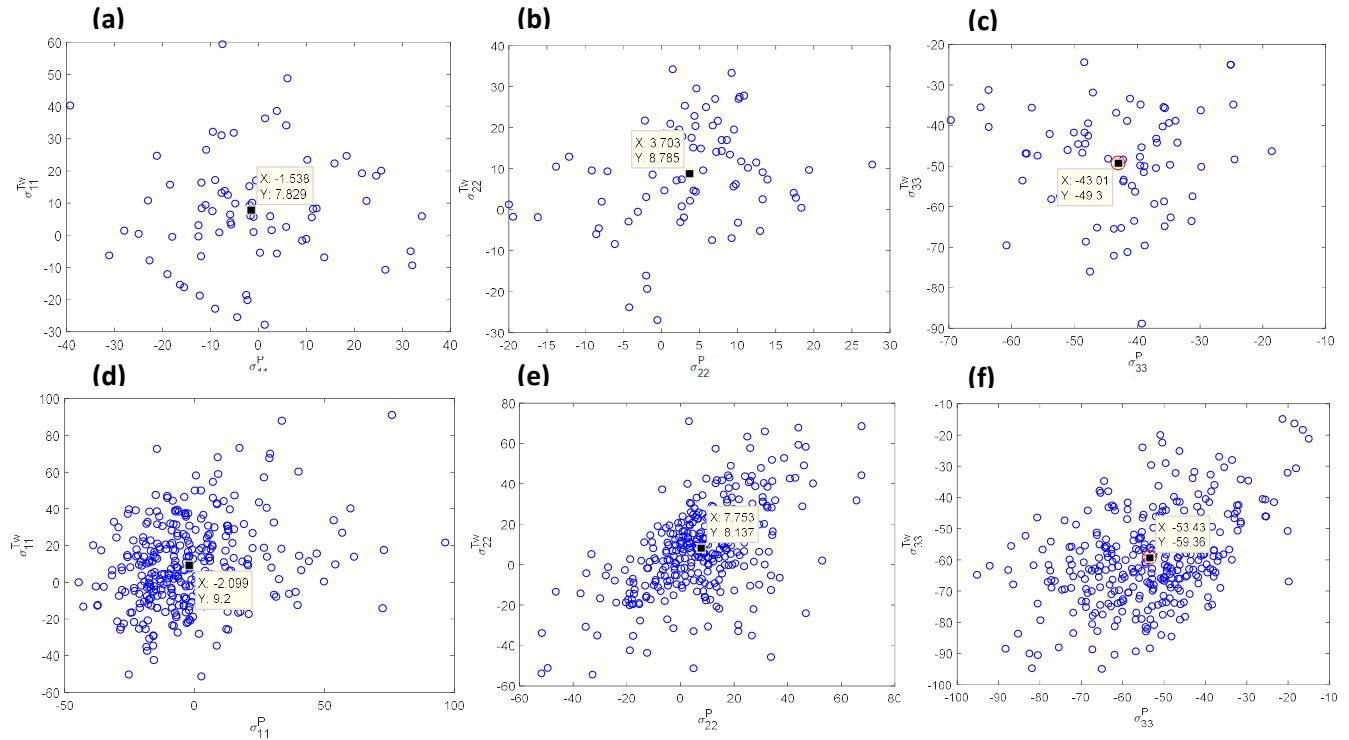
**Figure 5.9: The rank of twin variants: Global and local ranks based on stresses prior to twinning and after twinning in step-2, (a)-(c), and step-3, (d)-(f), respectively**

Similar to figures 4.13 for zirconium data, the variants that twinned in magnesium are given a rank depending on the value of their Schmid factors. Figures 5.9 (a)-(c) represent the ranks of the twins generated at the onset of plasticity and the figures (d)-(f) belong to twins nucleated in the plastic zone. The three figures are ranked based on the stresses in the step prior to twinning

and after twinning. Results show that most of the parent grains twin at the variants with the highest Schmid factor in the case of GSF. The significance of this experiment is that it shows for the first time that all twins are nucleated almost based on the strongest two variants using GSF, at the onset of plasticity; however, there is no predominant variant when LSF is used. This highlights the use of full-field models such as crystal plasticity finite element for simulating grain-level stresses and twinning. Since the grain-stresses change after twinning a significant change is observed in the rank of the twin variants. This signifies the use of in-situ and advanced experiment for measuring stresses in-situ as measuring stresses after twinning may be misleading.

Interestingly, with increasing plasticity, while the twinned variant stays as the predominant one (highest GSF), there is no change in LSF comparing to GSF. This is different compared to zirconium and it could be related to the elastic and plastic anisotropy of magnesium which are much lower than that of zirconium. Further, unlike zirconium, the overall state of the stress throughout the grain remains the same and stress within the twin is much closer to the parent. This can also be related to the degree of anisotropy in magnesium, however, numerical simulation is required to further confirm.





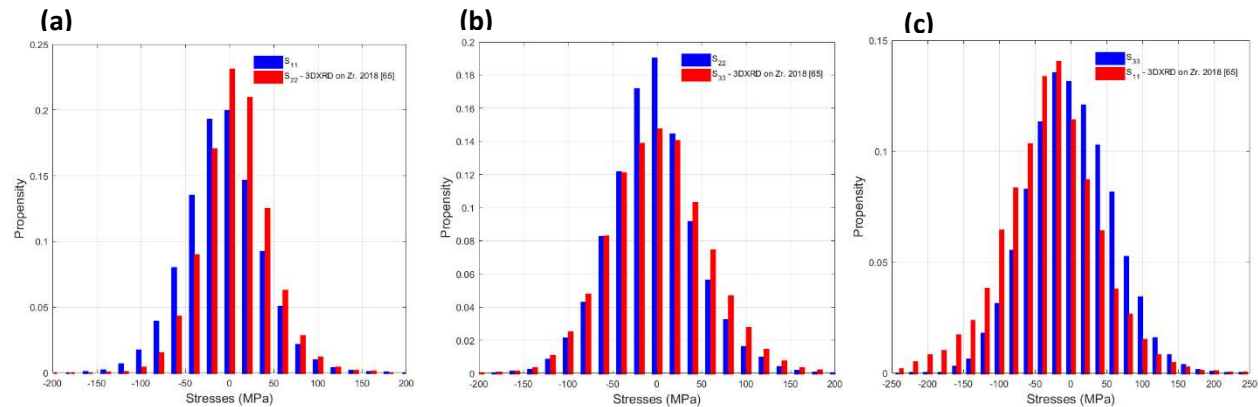
**Figure 5.10: normal stresses in the twins as a function of the stresses in their parents:  $S_{11}$ ,  $S_{22}$ , and  $S_{33}$ , in step-2, (a)-(c), and step-3, (d)-(f), respectively**

Figure 5.10 shows the stresses in parents and twins after nucleation at the onset of plasticity (step-2), and in the plastic zone (step-3). Like zirconium, the x-axis represents the stresses in the parent and y-axis resembles the stresses in twins. Every single point belongs to a parent grain and its corresponding twin and the numbers shown in the plots are the averages of the stresses calculated for all twin-parent pairs. The trends in the stresses are opposite to those observed in zirconium. Unlike zirconium, the twins are now the hard grains and the parent grains are the soft grains and this explains the higher stresses ( $S_{33}$ ) in twins as opposed to the parent grain.

## 5.4 Repeatability

Certain techniques can be used to validate the final grain maps and confirm the repeatability of the results. Since grains of each loading step is measured independently from other steps, grains that show up in one step should also appear in the consecutive step. This was confirmed in our measurements for both Zr and Mg samples. Moreover, two experiments are carried out on two different specimens and the results between the two experiments are compared. In both experiments it was observed that twins nucleated as the loading increases which is generally in agreement with independent 2D EBSD measurements. Another technique is comparing current

results with results in past experiments. Figure 5.11 shows the residual stresses at preload in the current experiment and another experiment from literature. A good agreement is observed between the stress distributions of both experiments. Finally, the measured texture from 3D-XRD for Zr was compared with those from EBSD confirming the repeatability and accuracy of orientation measurements.



**Figure 5.11: Residual stress distributions for current and past experiment. (a) – (c) is  $S_{11}$ ,  $S_{22}$  and  $S_{33}$  distributions respectively for current experiment.**

## 5.5 Conclusions

With the use of the developed algorithm, twinning and detwinning were captured during cyclic loading of a magnesium sample. Like zirconium, many twins were observed to nucleate in grains with high Schmid factor with respect to both global and local stresses. A small population of parent grains was also observed to have low twin-Schmid factors. Most of the twin nucleated in the grains with both local and global high Schmid factors. Unlike zirconium, the twin ranks acquired from parent stresses after twinning stay the same which indicates that the active variant does stay active after twinning. This is due to the low elastic anisotropy in the magnesium HCP crystals. Stresses in twins along the loading direction are high compared to the stresses in the parent grains. This is due to the soft and hard orientations of the parent and twin grains respectively and this also explains the low stresses in twins along the other two axes. Twin volume and number fraction were recorded for every step and plotted with respect to strain. In both cases, fractions were increasing linearly until maximum compressive strain and upon unload and stress reversal, the fraction reduced due to detwinning in both steps. Similar to the

zirconium case, twin volume fractions are larger than expected due to the overestimation of their actual volume after nucleation.

## Chapter 6

### 6. Conclusion and Future Work

#### 6.1 Conclusion

The scope of this work was to characterize twinning in 3D. Three-dimensional Synchrotron X-ray Diffraction (3D-XRD) was used for an in-situ tensile experiment on pure zirconium and an in-situ cyclic experiment on a magnesium alloy, Mg AZ31, specimen. The grain center-of-masses, Euler angles, average elastic strains and stresses, and volume fraction were measured. Over 11,000 grains were captured for zirconium and 8,000 grains in the case of magnesium from a total of 4 TB size of diffraction images. Surface measurements were conducted using EBSD, prior to the 3D-XRD experiment on zirconium and the measured pole figures are compared to those from 3D-XRD. The following conclusions can be made:

- Codes were developed to match measured grains from each loading steps. This was done in two steps: (a) matching and adding grains from different layers of each loading step and (b) matching grains between two loading steps.
- Codes were developed to identify twins and find their matching parent grain and follow them through deformation steps.
- EBSD results acquired from zirconium were compared with the results from the 3D-XRD measurements. Very good agreements are observed for both texture and grain sizes distribution confirming the validity of the codes developed for matching layers and steps.
- Both zirconium and magnesium specimen textures were favored to have tensile twins and most of these are nucleated at the onset and early stages of plasticity.
- For the first time, twinning and de-twinning was captured in 3D and Bauschinger effect is captured for each grain through their stress-strain curves.
- It was shown that twins of zirconium are relaxed comparing to their corresponding parent in the loading direction. This was due to the fact that twins mainly nucleated with their c-axis perpendicular to the loading direction.

- It was shown that unlike zirconium, twins in magnesium are, on average, more stressed comparing to their parent. This was because the twins of magnesium have their c-axis along the loading direction.
- Unlike zirconium, the stresses measured in twins of magnesium were higher than their parents. This is because twins of magnesium are hard grains and their corresponding parent grains are soft grains which explains the higher stresses ( $S_{33}$ ) in twins as opposed to the parent grain.
- Since the grain-average stresses are measured, both twin global and local Schmid factors (GSF, and LSF) were studied in details. It was shown that the predominant twin variant has the highest contribution to twin formation, however there are many twins that nucleated with low SF.
- For the zirconium sample, it was shown that at the beginning of the onset of plasticity, almost all of the twin variants are active equally; however, with more load applied, the predominant variant become the most active twin variant. These trends are observed using both GSF and LSF, but the contribution of each variant was different when GSF was used as oppose to LSF. This is significant for model development.
- It was shown that for the zirconium sample, the use of parent stress after twinning would result in completely reverse trend in calculating the twin rank. This shows that once a twin nucleated, state of the parent stress changes so that the same twin variant is not immediately the favorable variant.
- It was shown that for the magnesium sample, all twins are nucleated almost based on the strongest two variants using GSF, at the onset of plasticity; however, there is no predominant variant when LSF is used. This highlights the use of full-field models for simulating grain-level stresses and twinning. Since the grain-stresses change after twinning a significant change is observed in the rank of the twin variants. This signifies

the use of in-situ and advanced experiment for measuring stresses in-situ as measuring stresses after twinning may be misleading.

- It was shown that for the magnesium sample, with increasing plasticity, while the twinned variant stays as the predominant one (highest GSF), there is no change in LSF comparing to GSF. Further, unlike zirconium, the overall state of the stress throughout the grain remains the same and stress within the twin is much closer to the parent. This can be related to the degree of anisotropy in magnesium, however, numerical simulation is required to confirm.

## 6.2 Contributions

This section provides a short summary of the contributions made towards understanding deformation twinning. These contributions are as follows,

- A method was developed to merge grain maps of individual layers in 3D-XRD and compare it side by side with EBSD maps measured from the same area, same sample.
- A method was developed to find individual grains in all steps and track their evolution with macroscopic applied strain.
- A method was developed to capture nucleated twins from individual grain maps and pair them with their parent grains.
- Through the use of the above method, twin number and volume fractions were studied where twinning and detwinning for the magnesium sample was captured in three dimensions, for the first time.

## 6.3 Future Work

The next step aims at conducting finite element work to compare the results with those acquired through 3D-XRD. This will be done by creating 3D microstructures via the Voronoi tessellation using the measured COMs and volumes of each grain. This microstructure will be then used as an input to a crystal plasticity finite element (CPFE) model.

Further analysis will also be conducted on the 3D-XRD results to search for other variables that could impact twinning. These analyses include the following:

- Grain Size: The impact of grain size on twinning.
- Sequence of twinning: if chain of twins formed in mg or zr. Are the low LSF and GSF twins nucleated because of their neighbors? What drives nucleation of such twins.
- How de-twinning in Mg sample starts.
- Study the diffraction peak shapes from twins and parents and compare them to those from CPFE simulation.

## References

- [1] A. S. Zaimovskii, “Zirconium alloys in nuclear power,” *Sov. At. Energy*, vol. 45, no. 6, pp. 1165–1168, 1978.
- [2] E. G. Price, “Highlights of the Metallurgical Behaviour of Candu Pressure Tubes.,” *At. Energy Canada Limited, AECL*, 1984.
- [3] M. Griffiths, G. Bickel, D. Rodgers, S. S. Lawrence, C. Coleman, A. Buyers, and H. Nordin, “Performance of Pressure Tubes in Candu Reactors,” *CNL Nucl. Rev.*, vol. 5, no. 1, pp. 1–15, 2016.
- [4] H. Abdolvand, “Multi-scale Modeling and Experimental Study of Deformation Twinning in Hexagonal Close-Packed Materials,” *J. Mech. Phys. Solids*, 2012.
- [5] P. Davies, P. Chow, D. Rodgers, M. McManus, C. Coleman, B. Cheadle, S. Sagat, A. Causey, and G. van Drunen, “Evaluation of Zircaloy-2 Pressure Tubes from NPD,” *Zircon. Nucl. Ind. Eighth Int. Symp.*, pp. 35-35–15, 2008.
- [6] Natural Resources Canada, “The Canadian Nuclear Industry and its Economic Contributions,” *Gov. Canada*, pp. 1–2, 2016.
- [7] T. S. Some, D. The, and T. Ii, “Slip, Twinning, and Fracture in Hexagonal Close-Packed Metals,” 1981.
- [8] M. R. Barnett, “Twinning and the ductility of magnesium alloys Part I : ‘ Tension ’ twins,” vol. 464, pp. 1–7, 2007.
- [9] G. Ambrogio, C. Bruni, S. Bruschi, L. Filice, A. Ghiotti, and M. Simoncini, “Characterisation of AZ31B magnesium alloy formability in warm forming conditions,” pp. 205–206, 2008.
- [10] M. Majkut, “A study of deformation twinning in magnesium alloy AZ31B,” 2013.
- [11] E. Tenckhoff, *Deformation mechanisms, texture, and anisotropy in zirconium and zircaloy*, vol. 20, no. 21. 1988.
- [12] P. G. Partridge, “The crystallography and deformation modes of hexagonal close-packed



- metals,” *Metall. Rev.*, vol. 12, pp. 169–194, 1967.
- [13] E. Schmid and B. Walter, *Kristallplastizität: Mit Besonderer Berücksichtigung der Metalle*. 1935.
- [14] R. Peierls, “The size of a dislocation,” *Proc. Phys. Soc.*, vol. 52, no. 1, pp. 34–37, 1940.
- [15] F. R. N. Nabarro, “Dislocations in a simple cubic lattice,” *Proc. Phys. Soc.*, vol. 59, no. 2, pp. 256–272, 1947.
- [16] C. N. T. I. J. Beyerlein, “A probabilistic twin nucleation model for HCP polycrystalline metals,” *Proc. R. Soc. A Math. Phys. Eng. Sci.*, no. February, pp. 2517–2544, 2010.
- [17] A. G. Bilby, B. A. Crookerf, “The theory of the crystallography of deformation twinning,” *Proc. R. Soc. A Math. Phys. Eng. Sci.*, vol. 288, no. 1413, pp. 240–255, 1965.
- [18] M. Science, J. W. Christian, and S. Mahajant, “Deformation Twinning,” *Prog. Mater. Sci.*, vol. 39, pp. 1–157, 1995.
- [19] W. S. E. Orowan, J. S. Koehler, F. Seitz, W. T. Read, “Dislocations in Metals,” *Inst. Met. Div. Am. Inst. Min. Metal. Eng. Inc*, no. 1954.
- [20] H. Abdolvand and A. J. Wilkinson, “Assessment of residual stress fields at deformation twin tips and the surrounding environments Acta Materialia Assessment of residual stress fi elds at deformation twin tips and the surrounding environments,” *Acta Mater.*, vol. 105, no. February, pp. 219–231, 2016.
- [21] S. Pfeiffer and M. F. Wagner, “Elastic deformation of twinned microstructures,” *Proc. R. Soc. A Math. Phys. Eng. Sci.*, vol. 473, no. 2204, 2017.
- [22] R. W. C. R. L. Bell, “The dynamics of twinning and the interrelation of slip and twinning in zinc crystals,” *Proc. R. Soc. A Math. Phys. Eng. Sci.*, vol. 239, no. 1219, 1957.
- [23] T. Takeuchi, “Dynamic Propagation of Deformation Twins in Iron Single Crystals,” *J. Phys. Soc. Japan*, vol. 21, no. 2616, 1966.
- [24] S. Godet, L. Jiang, A. A. Luo, and J. J. Jonas, “Use of Schmid factors to select extension twin variants in extruded magnesium alloy tubes,” vol. 55, pp. 1055–1058, 2006.

- [25] J. F. Bingert, T. A. Mason, G. C. Kaschner, P. J. Maudlin, and G. T. Gray, "Deformation Twinning in Polycrystalline Zr : Insights from Electron Backscattered Diffraction Characterization," vol. 33, no. March, pp. 955–963, 2002.
- [26] Y. Guo, H. Abdolvand, T. B. Britton, and A. J. Wilkinson, "Growth of { 1122 } twins in titanium : A combined experimental and modelling investigation of the local state of deformation," *Acta Mater.*, vol. 126, pp. 221–235, 2017.
- [27] J. J. Jonas, S. Mu, and T. Al-samman, "The role of strain accommodation during the variant selection of primary twins in magnesium," vol. 59, pp. 2046–2056, 2011.
- [28] M. A. Kumar, I. J. Beyerlein, R. A. Lebensohn, and C. N. Tomé, "Modeling the effect of neighboring grains on twin growth in HCP polycrystals Modeling the effect of neighboring grains on twin growth in HCP polycrystals," 2017.
- [29] I. J. Beyerlein, L. Capolungo, P. E. Marshall, R. J. McCabe, C. N. Tomé, L. Capolungo, P. E. Marshall, R. J. McCabe, and C. N. Tomé, "Statistical analyses of deformation twinning in magnesium," vol. 6435, no. May, 2010.
- [30] M. A. Kumar, I. J. Beyerlein, R. J. McCabe, and C. N. Tome, "Grain neighbour effects on twin transmission in hexagonal close-packed materials ' 1," no. May, pp. 1–9, 2016.
- [31] A. et al. Khosravani, "Nucleation and propagation of {10–12} twins in AZ31 magnesium alloy," *Acta Mater.*, vol. 100, pp. 202–214, 2015.
- [32] A. Ghaderi and M. R. Barnett, "Sensitivity of deformation twinning to grain size in titanium and magnesium," *Acta Mater.*, vol. 59, no. 20, pp. 7824–7839, 2011.
- [33] M. S. Tsai and C. P. Chang, "Grain size effect on deformation twinning in Mg – Al – Zn alloy Grain size effect on deformation twinning in Mg – Al – Zn alloy," vol. 0836, 2013.
- [34] Y. T. Z. X. Z. Liao and X. L. W. J. Narayan, "Grain size effect on deformation twinning and detwinning," pp. 4467–4475, 2013.
- [35] L. Capolungo, P. E. Marshall, R. J. McCabe, I. J. Beyerlein, and C. N. Tome, "Nucleation and growth of twins in Zr : A statistical study," vol. 57, pp. 6047–6056, 2009.
- [36] P. A. Turner and C. N. Toivi, "A Study of Residual Stresses in Zircaloy-2 With Rod

- Texture,” *Acta Mater.*, vol. 42, no. 12, pp. 4043–4055, 2000.
- [37] C. A. Calhoun, E. Garlea, R. P. Mulay, T. A. Sisneros, and S. R. Agnew, “Investigation of the effect of thermal residual stresses on deformation of  $\alpha$ -uranium through neutron diffraction measurements and crystal plasticity modeling,” *Acta Mater.*, vol. 85, pp. 168–179, 2015.
- [38] C. C. Aydiner, J. V Bernier, B. Clausen, U. Lienert, C. N. Tomé, and D. W. Brown, “Evolution of stress in individual grains and twins in a magnesium alloy aggregate,” pp. 1–6, 2009.
- [39] H. Abdolvand and M. R. Daymond, “Journal of the Mechanics and Physics of Solids Multi-scale modeling and experimental study of twin inception and propagation in hexagonal close-packed materials using a crystal plasticity finite element approach ; part II : Local behavior,” *J. Mech. Phys. Solids*, vol. 61, no. 3, pp. 803–818, 2013.
- [40] H. Abdolvand, M. Majkut, and J. Oddershede, “Study of 3-D stress development in parent and twin pairs of a hexagonal close-packed polycrystal : Part II – crystal plasticity finite element modeling,” *Acta Mater.*, vol. 93, pp. 235–245, 2015.
- [41] T. R. Bieler, L. Wang, A. J. Beaudoin, P. Kenesei, and U. Lienert, “In Situ Characterization of twin nucleation in pure Ti using 3D-XRD In Situ Characterization of Twin Nucleation in Pure Ti Using 3D-XRD,” no. January 2015, 2014.
- [42] Y. B. Chun and C. H. J. Davies, “Twinning-induced negative strain rate sensitivity in wrought Mg alloy AZ31,” *Mater. Sci. Eng. A*, vol. 528, no. 18, pp. 5713–5722, 2011.
- [43] R. K. Mishra, S. Godet, L. Jiang, J. J. Jonas, A. K. Sachdev, and A. A. Luo, “Twinning and texture development in two Mg alloys subjected to loading along three different strain paths,” *Acta Mater.*, vol. 55, no. 11, pp. 3899–3910, 2007.
- [44] B. Clausen, C. N. Tomé, D. W. Brown, and S. R. Agnew, “Reorientation and stress relaxation due to twinning: Modeling and experimental characterization for Mg,” *Acta Mater.*, vol. 56, no. 11, pp. 2456–2468, 2008.
- [45] H. Abdolvand, M. Majkut, J. Oddershede, S. Schmidt, U. Lienert, B. J. Diak, P. J. Withers, and M. R. Daymond, “On the deformation twinning of Mg AZ31B: A three-

- dimensional synchrotron X-ray diffraction experiment and crystal plasticity finite element model,” *Int. J. Plast.*, vol. 70, pp. 77–97, 2015.
- [46] S. Saimoto, O. Cazacu, and G. C. Kaschner, “Characterization of work-hardening evolution in hexagonal metals using mean slip distance normalized with inter-obstacle spacing,” *Mater. Sci. Eng. A*, vol. 543, pp. 129–138, 2012.
- [47] H. Abdolvand, M. R. Daymond, and C. Mareau, “Incorporation of twinning into a crystal plasticity finite element model: Evolution of lattice strains and texture in Zircaloy-2,” *Int. J. Plast.*, vol. 27, no. 11, pp. 1721–1738, 2011.
- [48] H. Abdolvand and M. R. Daymond, “Internal strain and texture development during twinning: Comparing neutron diffraction measurements with crystal plasticity finite-element approaches,” *Acta Mater.*, vol. 60, no. 5, pp. 2240–2248, 2012.
- [49] W. H. Bragg and W. L. Bragg, “The Reflection of X-rays by Crystals,” *Proc. R. Soc. A Math. Phys. Eng. Sci.*, vol. 88, no. 605, pp. 428–438, Jul. 1913.
- [50] W. Yinghua, “Lorentz–polarization factor for correction of diffraction-line profiles,” *J. Appl. Crystallogr.*, vol. 20, no. 3, pp. 258–259, 1987.
- [51] M. J. Buerger, “The correction of x-ray diffraction intensities for lorentz and polarization factors,” *Proc. Natl. Acad. Sci. U. S. A.*, vol. 26, pp. 637–642, 1940.
- [52] M. M. Woolfson, *An Introduction to X-ray Crystallography. Cambridge*. Cambridge: Cambridge University Press, 1997.
- [53] O. Engler and V. Randle, *Introduction to texture analysis; macrotexture, microtexture and orientation mapping*. 2000.
- [54] I. Schlipf, M. Bauer, and H. Bertagnolli, “X-ray absorption spectroscopy,” *Chem. Solut. Depos. Funct. Oxide Thin Film.*, vol. 9783211993, pp. 181–212, 2013.
- [55] R. P. Goehner, R. G. Tissot, and J. R. Michael, “Small area analysis using micro-diffraction.”
- [56] H.-J. Bunge, “Texture analysis in materials science — 2Ed,” *Materials & Design*, vol. 4, no. 3. p. 795, 2003.

- [57] W. Massa, *Crystal Structure Determination*. Springer, 1994.
- [58] H. F. Poulsen, *Three-Dimensional X-ray Diffraction, Mapping Polycrystals and their Dynamics*, vol. 5. Springer, 2004.
- [59] G. E. Ice and B. C. Larson, “Three-Dimensional X-Ray Structural Polychromatic,” no. March 2004, 2014.
- [60] W. Yang, B. C. Larson, J. Z. Tischler, G. E. Ice, J. D. Budai, and W. Liu, “Differential-aperture X-ray structural microscopy : a submicron-resolution three-dimensional probe of local microstructure and strain,” vol. 35, no. 2004, pp. 431–439, 2008.
- [61] P. Reischig, A. King, L. Nervo, N. Viganò, Y. Guilhem, W. J. Palenstijn, K. J. Batenburg, M. Preuss, W. Ludwig, P. Reischig, A. King, L. Nervo, N. Viganò, and Y. Guilhem, “Advances in X-ray diffraction contrast tomography : flexibility in the setup geometry and application to multiphase materials To cite this version : HAL Id : hal-01553410 Advances in X-ray diffraction contrast tomography : flexibility in the setup geometr,” 2017.
- [62] Jon Wright, “Making a centre of mass grain map using the fable python module,” 2014.
- [63] J. Oddershede, “FitAllB version 1.1.1,” 2012.
- [64] H. Abdolvand, J. P. Wright, and A. J. Wilkinson, “On the state of deformation in a polycrystalline material in three- dimension : Elastic strains , lattice rotations , and deformation mechanisms,” *Int. J. Plast.*, vol. 106, no. March, pp. 145–163, 2018.
- [65] H. Abdolvand, J. Wright, and A. J. Wilkinson, “Strong grain neighbour effects in polycrystals,” *Nat. Commun.*, no. 2018, pp. 1–11.
- [66] J. Gong, T. B. Britton, M. A. Cuddihy, F. P. E. Dunne, and A. J. Wilkinson, “<a> Prismatic , <a> basal , and <c + a> slip strengths of commercially pure Zr by micro-cantilever tests,” *Acta Mater.*, vol. 96, pp. 249–257, 2015.
- [67] T. R. Bieler, L. Wang, A. J. Beaudoin, P. Kenesei, and U. Lienert, “In situ characterization of twin nucleation in pure Ti using 3D-XRD,” in *Metallurgical and Materials Transactions A: Physical Metallurgy and Materials Science*, 2014.
- [68] M. Shamma, N. Caspi, B. Anasori, B. Clausen, D. W. Brown, S. C. Vogel, V. Presser, S.

- Amini, O. Yeheskel, and M. W. Barsoum, "In situ neutron diffraction evidence for fully reversible dislocation motion in highly textured polycrystalline Ti 2 AlC samples," *Acta Mater.*, vol. 98, pp. 51–63, 2015.
- [69] N. Nguyen, O. S. Seo, C. A. Lee, M. Lee, J. Kim, and H. Y. Kim, "Mechanical Behavior of AZ31B Mg Alloy Sheets under Monotonic and Cyclic Loadings at Room and Moderately Elevated Temperatures," *Materials (Basel)*, pp. 1271–1295, 2014.
- [70] Q. Yu, J. Zhang, Y. Jiang, and Q. Li, "An experimental study on cyclic deformation and fatigue of extruded ZK60 magnesium alloy," *Int. J. Fatigue*, vol. 36, no. 1, pp. 47–58, 2012.

## Curriculum Vitae

**Name:** Karim Louca

**Post-secondary Education and Degrees:** American University of Sharjah  
Sharjah, United Arab Emirates  
2013-2017, B.Sc. Mechanical Engineering

**Honours and Awards:** NSERC Canada Graduate Scholarship - Masters  
2018-2019  
Dean's list  
2014-2016  
Chancellor's list  
2014-2016

**Related Work Experience**  
Graduate and Teaching Assistant  
The University of Western Ontario  
2018-2019  
Technical Engineer  
Building Technologies, Siemens, LLC  
2017  
Graduate and Teaching Assistant  
American University of Sharjah  
2015-2016